

Driver Command Interpreter
for
Electric Vehicles:
Development and Experiments

by

Abtin Athari

A thesis
presented to the University of Waterloo
in fulfillment of the
thesis requirement for the degree of
Master of Applied Science
in
Mechanical Engineering

Waterloo, Ontario, Canada, 2013

© Abtin Athari 2013

AUTHOR'S DECLARATION

I hereby declare that I am the sole author of this thesis. This is a true copy of the thesis, including any required final revisions, as accepted by my examiners.

I understand that my thesis may be made electronically available to the public.

Abstract

Electric-driven vehicles (EVs) are a relatively new topic in the area of alternative-fuel vehicles. EVs that have the capability for an independent wheel-drive system provide researchers and automakers with numerous benefits. These benefits include sharp torque generation and independent torque control at each wheel, which improves the dynamic stability of EVs on the road, and also increases energy efficiency.

Vehicle safety is a major challenge in the field of vehicle dynamics. There is an increasing demand for active safety systems in order to avoid accidents. The focus of this thesis is the development of a Driver Command Interpreter (DCI), which is used in conjunction with an active stability controller.

A DCI generates the desired longitudinal and lateral forces and the vehicle's yaw moment based on the driver's commands. These forces, as well as the yaw moment, are compared with the actual sensor data commonly mounted at the center of gravity (CG) location to produce error signals for the controller, which is in charge of correcting and stabilizing the vehicle by changing the torque in each wheel.

To simplify the computation of the vehicle's desired forces, a bicycle model is considered, including a full non-linear tire model. An algorithm was developed for the DCI, which is implemented in the Matlab code for simulation purposes. The algorithm is then implemented in the vehicle's real-time onboard computer to experimentally demonstrate the proposed DCI application to an active stability control. The execution of various standard stability tests prove the acceptable performance and accuracy of the proposed DCI.

Acknowledgements

First, I would like to express my gratitude to my thesis supervisor, Dr. Amir Khajepour, for his guidance and patience throughout the completion of my degree. This thesis would not have been possible without his constant support and trust.

I would also like to thank my colleagues at the University of Waterloo, for all of their support throughout my research. I cannot list all of your names here, but I will always carry fond memories of your company in the research lab.

Finally, I would like to express a sincere thanks to my lovely friends and family for all of their moral support. Last but not least, I would like to thank my beloved parents and sister for the endless love, encouragement, and support that they have provided me throughout my life.

Dedication

This thesis is dedicated to my parents.

My success would not be possible without their sacrifice.

Table of Contents

AUTHOR'S DECLARATION.....	ii
Abstract	iii
Acknowledgements.....	iv
Dedication	v
Table of Contents	vi
List of Figures	viii
List of Tables	xi
Nomenclature	xii
Chapter 1 Introduction	1
1.1 Background Statement	1
1.2 Objectives and Research Scope	2
Chapter 2 Literature Review & Background	4
2.1 Electric Vehicles	4
2.2 Stability Control Systems.....	5
2.3 Driver Command Interpreter Background	7
2.4 Different Mathematical Vehicle Models.....	10
Chapter 3 Modeling and Computer Simulations.....	13
3.1 Vehicle Model.....	13
3.1.1 Bicycle Model.....	15
3.1.2 Tire Model	17
3.1.3 Resistive Forces	19
3.2 Computer Simulation	22
3.2.1 CarSim Software.....	23
3.2.2 Modeling Opel Corsa in CarSim.....	23
3.2.3 Test Scenarios and Results.....	25
Chapter 4 Hardware-in-the-loop Analysis	33
4.1 Hardware Description	33
4.1.1 Propulsion System	34
4.1.2 Brake System	37
4.1.3 Control System.....	41
4.1.4 Electric Energy Storage System.....	45

4.1.5 Inertial Measurement Unit.....	47
4.2 Vehicle Parameters Measurements.....	49
4.2.1 Steering Wheel Gear Ratio	50
4.2.2 Weight Measurement Procedure	51
4.2.3 Center of Gravity (CG) Location	53
4.3 Hardware-in-the-loop setup.....	53
4.4 Implementation Issues and Solutions	56
4.4.1 Sample-Time Issue	56
4.4.2 Noise Issue	56
4.4.3 Acceleration Generation from IMU Outputs.....	58
Chapter 5 Full Vehicle Testing.....	59
5.1 Standard Tests Description.....	59
5.1.1 Test Track.....	59
5.1.2 Environmental Conditions.....	60
5.1.3 Test Scenarios.....	60
5.1.4 Test Driver.....	62
5.2 Results and Analysis.....	63
5.2.1 Double Lane Change (DLC) Test Results	63
5.2.2 Slalom Test Results	67
Chapter 6 Conclusion and Recommendations.....	72
6.1 Conclusion and Summary.....	72
6.2 Future Work	73
Bibliography	74
Appendix A Tire Model Parameters.....	78
Appendix B RT2000 Specifications	79
Appendix C Vehicle Components	80
Appendix D Aerodynamic Drag Coefficient Tables	81
Appendix E CarSim/Simulink Simulation Interface	84
Appendix F DCI Model Matlab Code	85
Appendix G Sensitivity Analysis Results.....	97

List of Figures

Figure 1-1: Vehicle stability controller framework	2
Figure 2-1: Comparison of drivetrains in ICE vehicle and EV.....	5
Figure 2-2: Vehicle performance with/without ESC system	6
Figure 2-3: How stability controller creates rotational torque	7
Figure 2-4: Control architecture.....	8
Figure 2-5: Coordinated traction control structure.....	9
Figure 2-6: 2-DOF Bicycle Model.....	10
Figure 2-7: Additional dynamic roll model for a bicycle model	11
Figure 2-8: 10-DOF Vehicle Dynamic Model	12
Figure 3-1: ISO coordinate system in vehicle dynamics	14
Figure 3-2: Four-Wheel Vehicle Model Coordinates	14
Figure 3-3: Single track bicycle model.....	15
Figure 3-4: Velocity and moments acting on the bicycle model	16
Figure 3-5: Linear and Nonlinear Tire Model Curves	19
Figure 3-6: Air flow over the vehicle.....	20
Figure 3-7: Aerodynamic slip angle relative to vehicle longitudinal axis	21
Figure 3-8: Computer simulation framework	23
Figure 3-9: CarSim main vehicle configuration page.....	24
Figure 3-10: CarSim vehicle model specifications	24
Figure 3-11: CarSim DLC predefined trajectory	25
Figure 3-12: DLC Computer Simulation Input Steering Angle.....	26
Figure 3-13: DLC computer simulation vehicle forward velocity	26
Figure 3-14: DLC computer simulation forward force at CG point	27
Figure 3-15: DLC computer simulation lateral force at CG point.....	27
Figure 3-16: DLC computer simulation yaw moment at CG point.....	28
Figure 3-17: Stability test computer simulation input torques.....	29
Figure 3-18: Stability test computer simulation input steering angle	29
Figure 3-19: Stability test computer simulation vehicle forward velocity	30
Figure 3-20: Stability test computer simulation forward force at CG point	31
Figure 3-21: Stability test Computer simulation lateral force at CG point	31
Figure 3-22: Stability test computer simulation yaw moment at CG point	32

Figure 4-1:4WD electric-driven Opel Corsa with four in-wheel motors	33
Figure 4-2: Electric In-Wheel Hub.....	35
Figure 4-3: In-wheel electric motor fitted in to the rim.....	35
Figure 4-4: PIM Operation Range.....	36
Figure 4-5: Parallel friction and regenerative braking system	38
Figure 4-6: Friction brake hydraulic pump and control box.....	38
Figure 4-7: Hydraulic brake line	39
Figure 4-8: Brake pressure pump and sensor test setup	39
Figure 4-9: Hydraulic pump pressure at different voltages	40
Figure 4-10: Friction Brake Mapping.....	40
Figure 4-11: Diagnostic Interface Panel.....	42
Figure 4-12: Graphical User Interface.....	43
Figure 4-13: GUI first layer.....	43
Figure 4-14: GUI motor information screen.....	44
Figure 4-15: GUI dynamic screen	44
Figure 4-16: High voltage battery packs	45
Figure 4-17: 12V battery located under the hood.....	46
Figure 4-18: Manzanita Micro PFC Charger.....	47
Figure 4-19: OXTS 6-axis GPS IMU	47
Figure 4-20: Coordinate system of the IMU	48
Figure 4-21: Location of OXTS IMU	49
Figure 4-22: Setup for steering gear ratio measurement	50
Figure 4-23: Front wheel assembly with wheel hub motor	51
Figure 4-24: Vehicle sitting on the load scales.....	52
Figure 4-25: Hardware-in-the-loop simulation framework	54
Figure 4-26: Vehicle off the ground in the lab for HIL test	55
Figure 4-27: HIL Computer connected to the vehicle in the lab	55
Figure 4-28: DCI internal prediction.....	56
Figure 4-29: Chebyshev type II filter bode diagram	57
Figure 5-1: Test Track.....	59
Figure 5-2: Test track with cones setup for double-lane-change scenario	61
Figure 5-3: Top view of the test track with pylons in place for a double-lane-change maneuver.....	61

Figure 5-4: Semi-Slalom Test.....	62
Figure 5-5: DLC test input torques	64
Figure 5-6: DLC test input steering angle.....	64
Figure 5-7: DLC test vehicle forward velocity	65
Figure 5-8: DLC test forward force at CG point.....	66
Figure 5-9: DLC test lateral force at CG point	66
Figure 5-10: DLC test yaw moment at CG point.....	67
Figure 5-11: DLC test vehicle trajectory	67
Figure 5-12: Slalom test input torques.....	68
Figure 5-13: Slalom test input steering angle	68
Figure 5-14: Slalom test vehicle forward velocity.....	69
Figure 5-15: Slalom test forward force at CG point	70
Figure 5-16: Slalom test lateral force at CG point.....	70
Figure 5-17: Slalom test yaw moment at CG point.....	71
Figure 5-18: Slalom test vehicle trajectory	71
Figure A-1: Performance Specification for the RT2000 Systems	79
Figure A-2: Detailed picture of all vehicle components and sensors.....	80
Figure A-3: Longitudinal drag coefficient vs. vehicle slip angle.....	81
Figure A-4: Lateral drag coefficient vs. vehicle slip angle.....	82
Figure A-5: Vertical drag coefficient vs. vehicle slip angle	83
Figure A-6: CarSim/Simulink Simulation Interface	84

List of Tables

Table 1: Some typical rolling coefficients.....	22
Table 2: Vehicle load/mass measured data.....	52
Table A-1: List of the parameters for nonlinear tire model.....	78

Nomenclature

α	Tire slip angle
β	Vehicle slip angle
Δz_{ij}	Vertical displacements of the suspension systems
δ	Front steering angle
θ	Pitch angle
ϕ	Roll angle
ψ	Heading angle
ω	Wheel angular velocity
C_α	Cornering stiffness
C_ϕ	Roll damping coefficient
C_f, C_r	Damping coefficient of the suspension system (front, rear)
F	Tire force (with a corresponding subscript)
g	Gravity constant
H_{CG}	Height of center of gravity
H_{CR}	Height of the roll center
I_w	Wheel moment of inertia around its spin axis
I_ϕ	Roll moment of inertia
I_{xz}	Product moment of inertia (xz component)
I_y	Pitch moment of inertia
I_z	Yaw moment of inertia
K_ϕ	Roll stiffness coefficient
K_{af}	Stiffness of front anti roll bar
K_f, K_r	Spring stiffness of the suspension system (front, rear)
L	Wheelbase
L_f, L_r	Horizontal distance between the center of gravity of the vehicle and the front and rear axles, respectively
L_s	Distance from CG to the wheel (with a corresponding subscript)
m	Vehicle Mass
m_s	Mass of the sprung mass
R	Effective radius of wheel
r	Yaw rate
\dot{r}	Yaw acceleration
T	Wheel torque
t_f, t_r	Front and rear track widths, respectively

v_x, v_y	Longitudinal and lateral velocity, respectively
a_x, a_y	Longitudinal and lateral acceleration, respectively
V	Velocity of tire (with a corresponding subscript)
V_{CG}	Vehicle body velocity
μ	Road coefficient of friction
β_{air}	Aerodynamic slip angle
D_{air}	Air mass density
A_f	Frontal area of the vehicle
C_{rr}	Rolling resistance coefficient
N	Tire static normal load
ij subscript	Indicator subscript for corners of the vehicle (fl : front-left, fr : front-right, rl : rear-left, rr : rear-right)
f, r subscript	Front and rear indication subscripts, respectively
x, y, z subscript	Coordinates in the corresponding coordinate system

Chapter 1

Introduction

1.1 Background Statement

Since automobiles are the primary means of transportation for humans, they play a vital role in each of our lives. The first cars appeared in 1806 and were powered by internal combustion engines (ICEs). There are already millions of cars and light trucks on roads around the world, and the number continues to increase each year. Conventional ICEs are known to cause air pollution; as such, the auto industry has been forced to find alternative solutions to power vehicles.

Electric and hybrid vehicles are slowly being introduced to the market by cars manufacturers, and are expected to take a bigger share of the vehicle market within the next decade. Specifically, EVs have several advantages over ICE vehicles, including quick and precise torque generation, which helps to control vehicle chassis stability.

The safety of EVs on roads is a major topic in the area of vehicle dynamics. EVs are divided into different types, with each type possessing diverse motor combinations. All models with independent wheel drive systems have the ability to control the torque of each wheel independently; changing the torque at each wheel separately produces the required body yaw moment.

When a human is driving a car, the sensory system within the vehicle helps him/her to comprehend the vehicle's surroundings, where it is located, and where it supposed to go. This sensory system also assists the driver in controlling the car and applying the appropriate inputs to the vehicle. Thus, it is important to ensure that this information is reliable. While using different sensors can be a solution, the cost of these sensors are relatively high.

Automakers prefer to decrease the number of sensors installed on vehicles because it helps reduce the overall price of the vehicle. As such, it is advantageous to have a robust algorithm to calculate desired control signals based on basic inputs provided from the driver. Such an algorithm can also lessen the computational time while increasing reliability.

The focus of this thesis is on the development of an algorithm that interprets driver inputs. It includes mathematical modeling, Hardware-in-the-Loop (HIL) analysis, and on-road full vehicle experimentation.

1.2 Objectives and Research Scope

The objective of this research work is to implement and verify a Driver Command Interpreter (DCI), which is a connection between the driver and the stability controller system for EVs. Figure 1-1 represents the overall schematic diagram of the vehicle control system, including the DCI module:

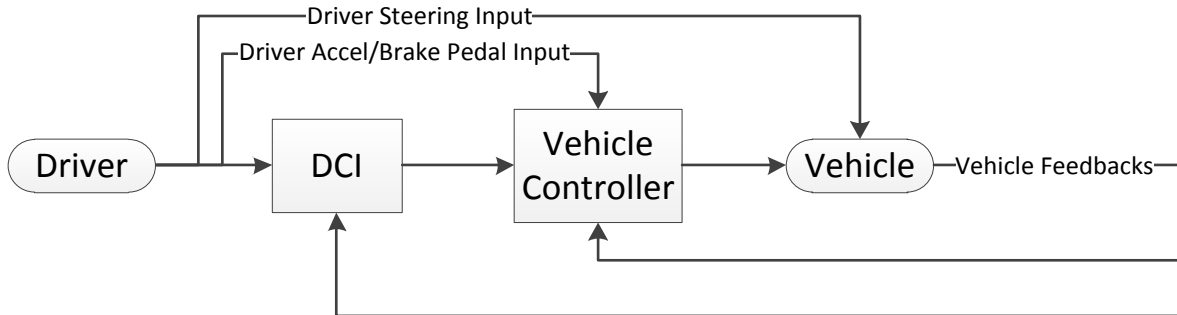


Figure 1-1: Vehicle stability controller framework

The outputs controlled by the driver are the acceleration pedal, brake pedal, and wheel steering angle. This torque and wheel steering angle are inputs to the DCI, in addition to the velocity feedback from the vehicle body. The steering angle is sent directly to the front wheels, and torque is sent to the stability controller for further action. This further action can either be the addition or subtraction of torque to the electric motors.

EVs are controlled differently based on the structure of the controller designed for them, depending on the required application. For example, one controller compares the yaw motion of the vehicle, while another compares its longitudinal forces. The controller in need of DCI monitors the vehicle forces and moment at the center of gravity (CG) location. All controllers are in need of having two sets of comparable signals to define the error, which needs to be minimized. Actual signals are usually feedbacks from the vehicle accelerometers or Inertial Measurement Units (IMU), and desired signals are produced by DCI. The final positive or negative torque at each wheel is determined based on this error.

The desired forces of the vehicle CG point are calculated by DCI, which contains a robust algorithm to calculate the desired forces, as well as the vehicle moment at CG point. The approach taken in this study was to first find and employ the appropriate vehicle model in the DCI structure.

The performance of the proposed vehicle stability control system and DCI algorithm was verified with simulations and experiments using a compact-class passenger vehicle equipped with four electric in-wheel motors.

This thesis work includes 6 chapters. The next chapter contains a literature survey about electric vehicles that are currently available, as well as different control systems and previous work similar to the DCI. The mathematical modeling of the proposed DCI, including all formulations and simulations are presented in chapter 3. Chapter 4 includes Hardware-in-the-loop analysis, as well as all vehicle hands-on experimentations. Full vehicle testing and the corresponding results are explained in chapter 5, while the last chapter presents the conclusion and suggested future work.

Chapter 2

Literature Review & Background

This chapter reviews the literature that has been published regarding electric vehicles and common safety systems. The first section provides a brief background about electric vehicles and the existing models of such vehicles. The subsequent section describes different types of lateral control systems that are currently used or are under development by automotive manufacturers and researchers. Lastly, the final section elaborates on previous work that is similar to the proposed DCI.

2.1 Electric Vehicles

The idea of conventional fuel-powered automobiles was introduced in 1823 when Samuel Brown submitted his patent for the first internal combustion engine. Many different fuels have been used since then, but vehicles with gasoline and diesel-fueled combustion engines are still common in the present day.

In these type of vehicles, the engine's power is mechanically transmitted to the driving wheels through the transmission, differential, and gears. The function of the transmission is to produce the different input/output power ratios based on the vehicle's state. The gear box also makes it possible to have various rotating speeds between the left and right driving wheels; this is necessary for when the ground condition is not the same under the two wheels, or while turning [1, 2].

Rising gas prices and increasing environmental concerns (e.g., air pollution and global warming, among others) have inspired the automotive industry to shift towards the development of green transportation systems. EVs are feasible alternative solutions to these concerns because they significantly contribute towards lowering the cost of energy, while also increasing environmental protection. Moreover, EVs have the capability to produce quick and precise torque generation, a distinct advantage compared to other vehicle types. These cars are also less noisy than conventional vehicles, and demonstrate high energy efficiency because they waste less energy in the form of heat. Lastly, the cost of electric motors is also relatively low [3].

The drive system of EVs is comprised of a power source, inverter module, and electric motor. The mechanical energy is transferred from the motor to the wheels through the driving shaft, while

the wires transfer electric power from the batteries to the inverter and motor. Figure 2-1 shows two system diagrams explaining the components of drive systems for ICE vehicles and EVs [4, 5].

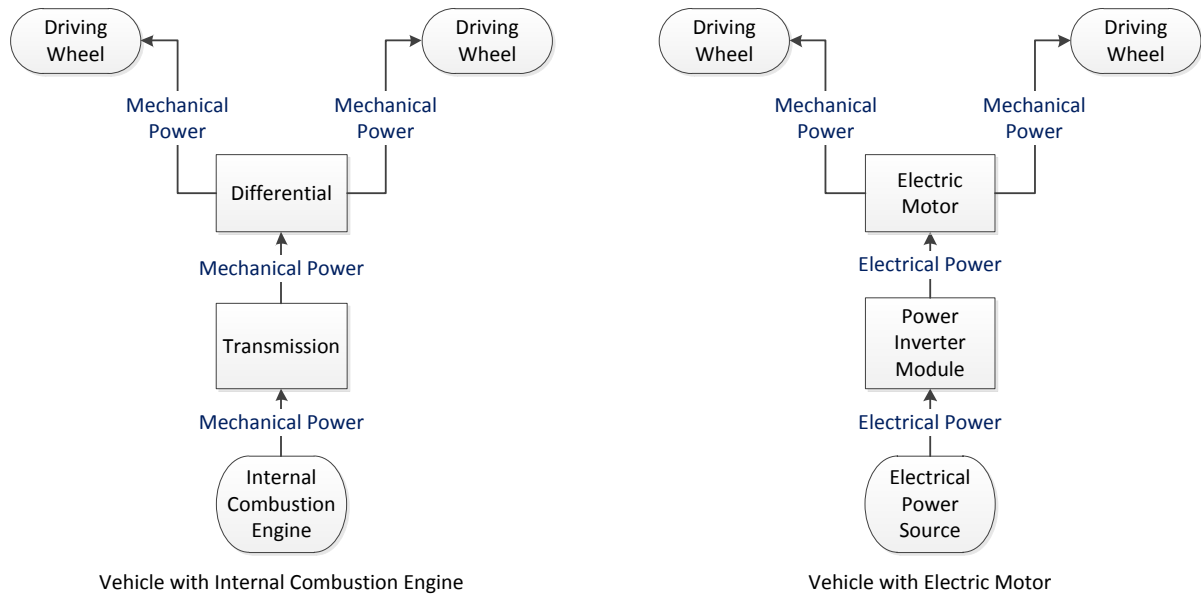


Figure 2-1: Comparison of drivetrains in ICE vehicle and EV

Four-wheel EVs are divided into three categories based on their motor configurations for shaping the propel system: four in-wheel motors, two independent motors for the front and rear axles, and a single motor running all four wheels. EVs with independent drive motors have advantages over other EVs, since it is possible to independently control the driving forces of wheels by changing the electric current and voltage of each separate motor.

The fast response characteristic of electric motors enables the driver to accurately control wheel speeds, thereby achieving enhanced handling performance. These motors help in stabilizing vehicle motion by generating counter-directional torques between the left and right wheels using predefined control strategies. Applying such controllers to ICE vehicles requires the addition of complex hardware to the vehicle structure, whereas in EVs, only software modification is needed [4].

2.2 Stability Control Systems

When discussing cars, most people are usually concerned about horsepower, torque, and zero-to-hundred acceleration. However, the power produced by the engine is useless if the driver is not able to control the vehicle [6]. There are many different control systems in research literature, some of

which are currently employed by automakers on mass-produced vehicles. The most common safety systems include the Antilock Brake System (ABS), the Traction Control System (TCS), and the Electronic Stability Control (ESC). Below is a quick overview of these systems, as well as the stability control of the proposed EV.

ABS helps drivers stop vehicles faster while maintaining steering control, and is mandatory on all light-weight vehicles. Recent statistics have shown that since the employment of ABS technology during the last decade, driving fatalities have significantly declined [7].

TCS is built to prevent wheel slippage when it moves on a surface with a low friction coefficient. This is done by using the independent brake system of the vehicle, available through ABS technology [8].

ESC is a system used to control the yaw motion of the vehicle in order to keep it stable and secured on the road. During extreme maneuvers, ESC can control the lateral dynamic motion of the vehicle by producing sufficient yaw torque. Achieving this goal requires a strategic controller for the rotational torque based on the system state feedback and the actuation system. In Figure 2-2, the middle car represents the vehicle with ESC, while the other two cars do not have this system. Front-wheel and rear-wheel slips lead to the understeer and oversteer conditions, respectively.

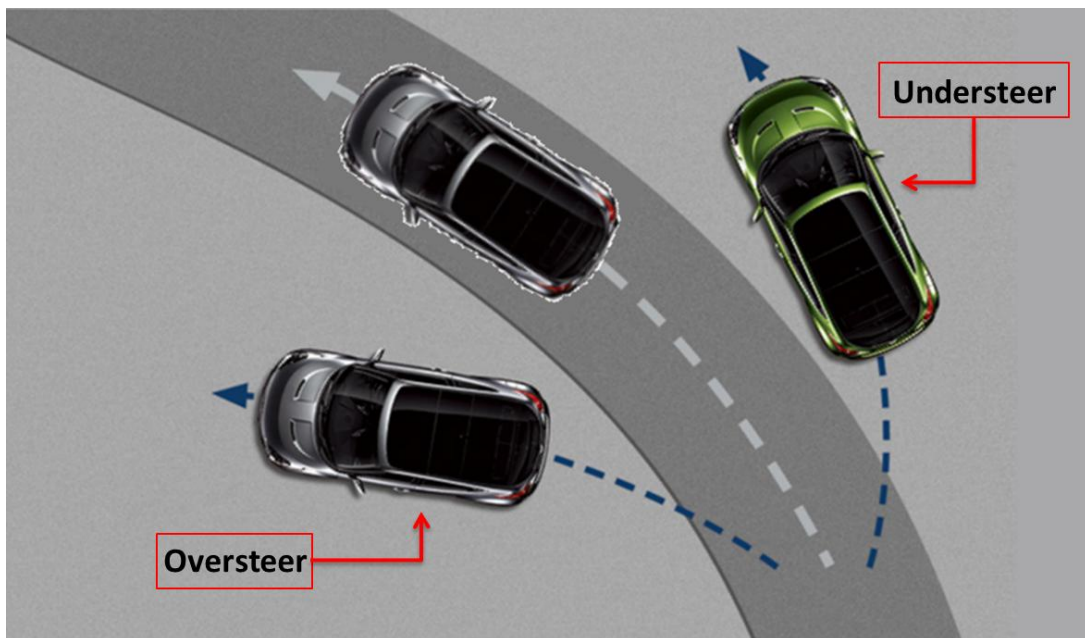


Figure 2-2: Vehicle performance with/without ESC system [9]

ESC in ICE vehicles create the required rotational moment by using independent wheel brakes and producing different braking forces between the left and right sides of the vehicle, while also cutting engine power. This method is known as Differential Braking and uses the Antilock Braking System along with robust control logic [10]. Contrary to conventional vehicles, in EVs, the driving force of the motors can be used to generate the required rotational torque.

2.3 Driver Command Interpreter Background

This section describes prior work on EV stability, and how these works are different from the work described in this thesis. It also discusses the reasons behind why DCIs are needed in an EV.

Piyabongkarn et al. describe the difference between brake-based and torque-based stability controllers as follows: “in contrast to brake-based yaw stability control systems, torque biasing has the potential to provide yaw stability control without slowing down the longitudinal response of the vehicle” [11]. In other words, while the desired speed of the vehicle is maintained, the yaw rate error and body slip angle error for a given steering input has to be minimized. This is one of the advantages of EVs that support independent drive systems. Figure 2-3 shows the performance of the stability controller under a condition that creates a counter-clockwise rotational torque at the vehicle’s CG by increasing the magnitude of the torque on the two right wheels.

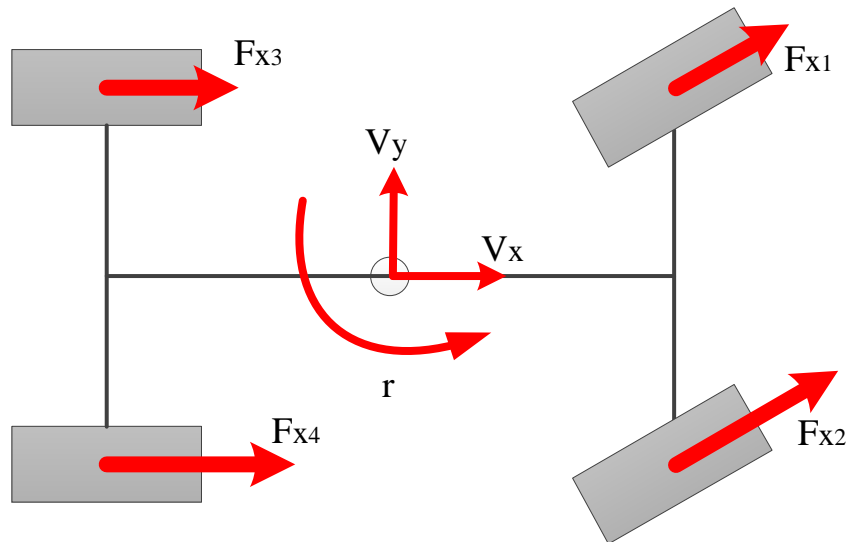


Figure 2-3: How stability controller creates rotational torque

Piyabongkarn et al. also demonstrated the control architecture for the yaw stability control system to be hierarchical, as shown in Figure 2-4. In this system, the role of the upper controller is to maintain yaw stability control and to command any desired value of yaw moment. The actual measured data is obtained from different sensors, and a designed control law computes the desired value of the yaw moment. The role of the lower controller is to ensure that the desired yaw torque is commanded by a change in the wheel’s rotational dynamics [12].

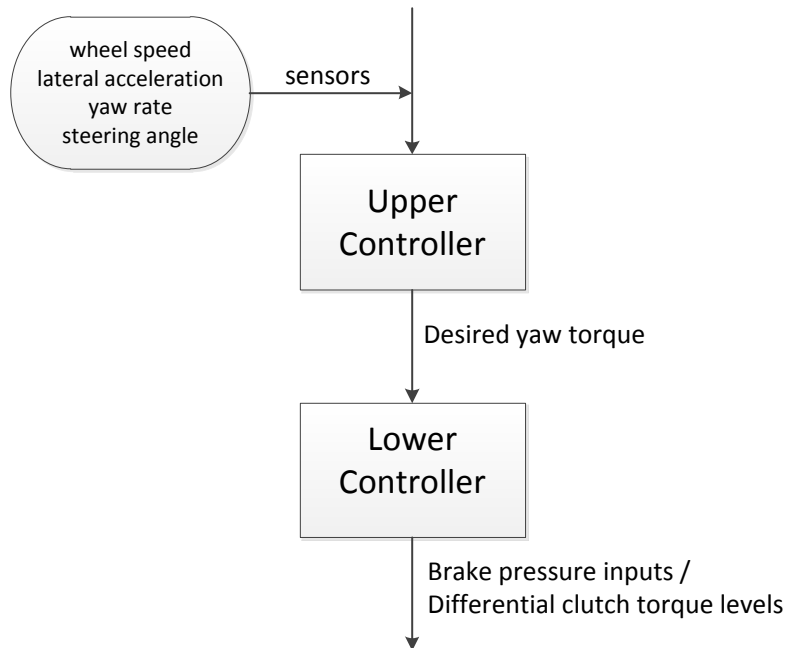


Figure 2-4: Control architecture [13]

In the approach proposed in this thesis, the role of the DCI is the same as that of the upper controller. While only the desired yaw torque is produced in Piyabongkarn’s approach, the DCI proposed in this thesis produces all three of the main forces at the vehicle’s CG location. The role of the stability controller is analogous to the lower controller, which carries the wheels’ torque adjustment job.

Another similar work deployed the hierarchical control architecture for the stability of EVs. This approach only focused on the desired longitudinal traction force and yaw moment, which is sent to the middle layer. As stated by Chu et al. [14], “in the middle layer, the control allocator maps the virtual controls into the actual control, representing desired motor torque for individual motors”,

and “in the lower layer, motor torque is applied as the input to motor normalization block”. The framework of this hierarchical controller is shown in Figure 2-5.

The proposed DCI can be distinguished from Chu et al.’s work because the desired lateral force was also included and compared in the controller logic.

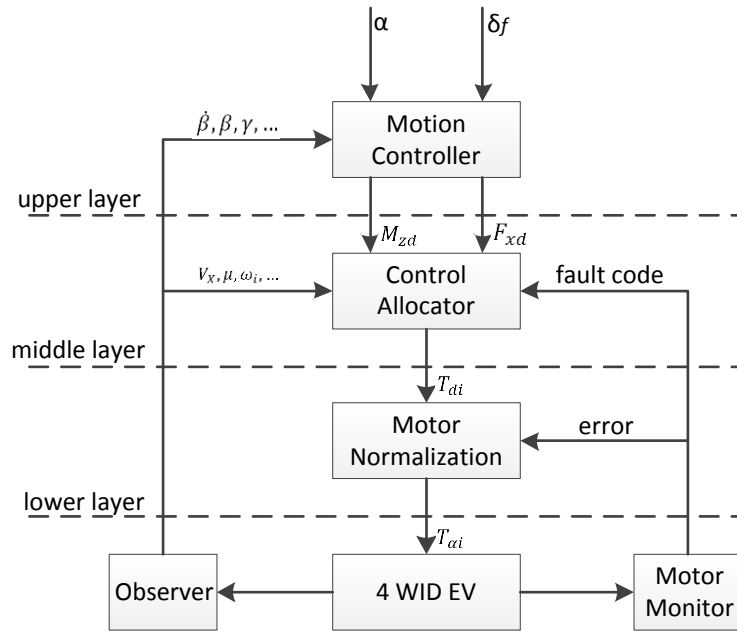


Figure 2-5: Coordinated traction control structure [14]

Chung et al. discuss how the stability controller’s performance can be improved based on different kinds of drivers, and propose either a nominal value approach, or a control-threshold adaptation as two possible solutions. This resulted in a vehicle state estimator based on driver inputs [15]. This idea can be considered as a future work in extending a stability controller for EVs.

The proposed stability controller for the independent-drive EV is similar to the ESC system of ICE vehicles. They are similar because they both maintain vehicle control by determining the driver’s intended commands, as well as by measuring vehicle response and performing the required correction if the response does not match the driver’s intentions. While the driver’s commands are steering-wheel angle and torque request, the vehicle feedback responses are the forward and lateral forces plus the rotational moment at the CG point, which will be obtained by the IMU.

In the research described in this thesis, the available test vehicle has four independent in-wheel motors without any differential and transmission systems involved. To understand the proposed

DCI algorithm, a review of the different vehicular mathematical models proposed in research literature is necessary.

2.4 Different Mathematical Vehicle Models

Accurately modeling the vehicle's dynamics is the first step in developing systems such as stability controllers. There are a variety of vehicle dynamic models, ranging from the one-degree-of-freedom (1-DOF) model, to highly complicated models implemented in software that enables researchers to find suitable models for the purpose of their studies.

The analytical 2-DOF model (the Bicycle model) only has two degrees of freedom, and is repeatedly used in research literature [16, 17, 18, 19, 20]. This model is popular because of its simplicity, as well as its capacity to be used in a closed-form solution for the dynamics of a vehicle in linear tire regions and low lateral accelerations.

Figure 2-6 shows this model:

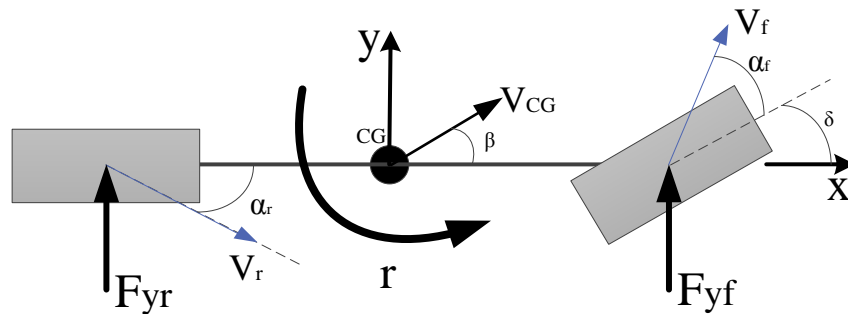


Figure 2-6: 2-DOF Bicycle Model

The combination of the 2-DOF model with the 1-DOF roll model generates a 3-DOF model, which is commonly used to evaluate the effect of roll motion on the handling and stability of the vehicle. Takano et al. have used such a model in their studies [21] to improve roll stability, as shown in Figure 2-7. Point *CR* is the roll center of this model.

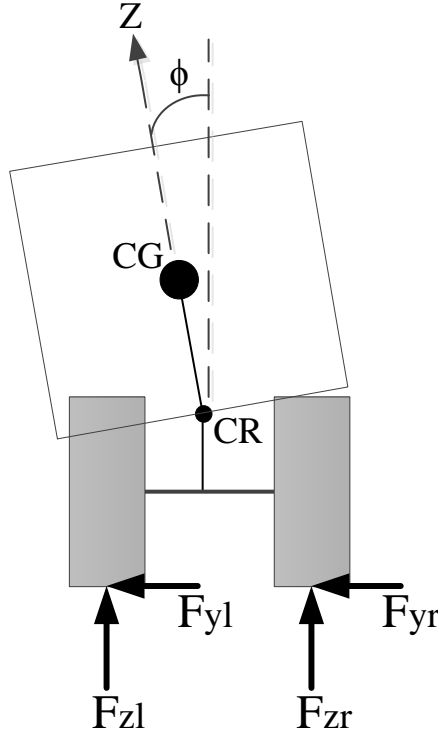


Figure 2-7: Additional dynamic roll model for a bicycle model

To investigate the effect of wheel dynamics on the vehicle's motion, a higher-DOF vehicle model is obtained by adding wheel dynamic equations to the previous model. Such a model has been widely used in research literature. To consider the nonlinear behavior of the tires, a nonlinear tire model can be used and tuned to match the tires of the given vehicle. Two popular tire models for this purpose are the Pacejka model, and the combined slip tire models. A detailed description of these tire models can be found in [22].

Reference [23] is an example of using a 7-DOF vehicle model to develop a lateral vehicle motion controller. In this paper, tire torques are control inputs for longitudinal motion, and also provide the required external yaw moment to stabilize lateral and yaw dynamics. The dynamic vehicle model in this study includes the longitudinal, lateral, and yaw dynamics of the planar motion, as well as the rotational dynamics of the four wheels.

Adding the roll, pitch, and vertical motions to the preceding 7-DOF dynamic model creates a 10-DOF model, known as the Semi-Full vehicle model, as shown in Figure 2-8 [24].

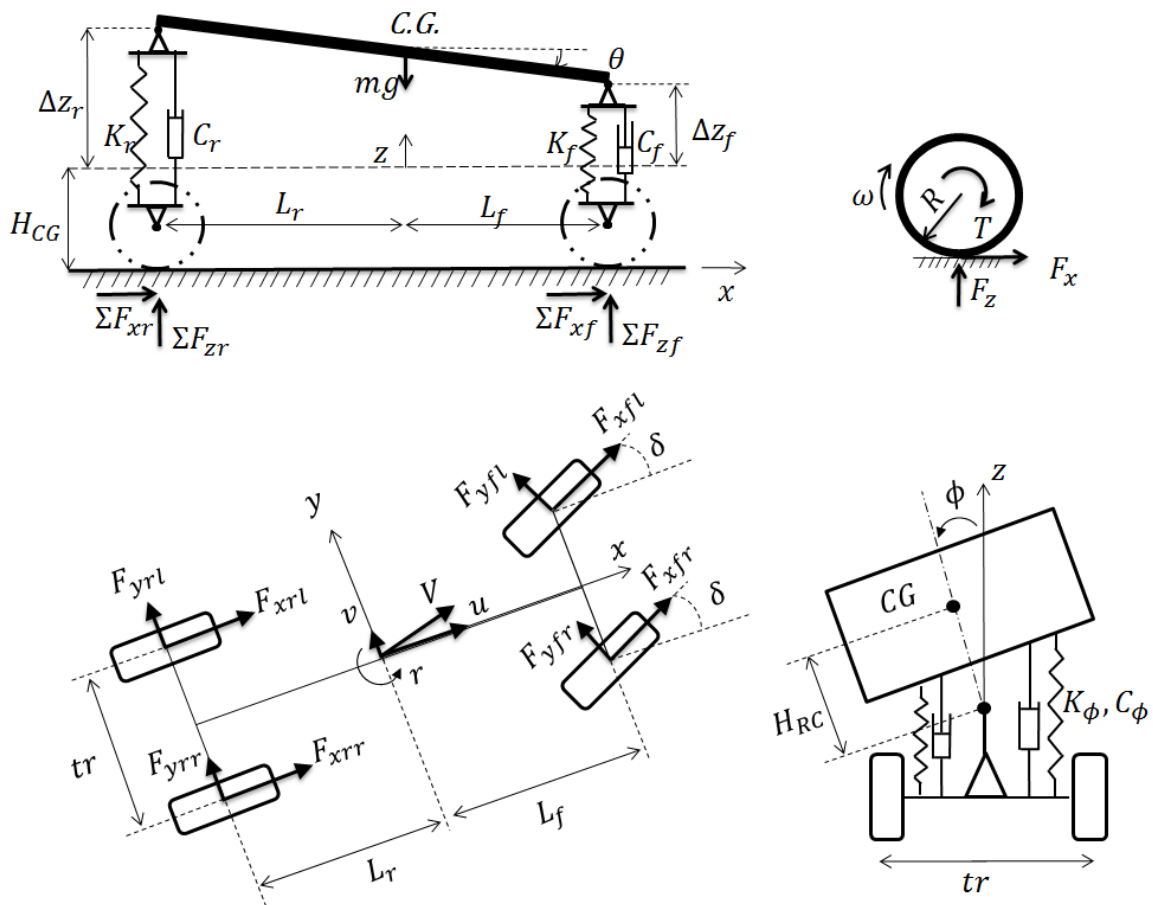


Figure 2-8: 10-DOF Vehicle Dynamic Model [24]

There are highly complicated vehicle dynamic models for various purposes, such as for the simulation and implementation of control algorithms. As an example, reference [25] illustrates a 127-DOF vehicle model developed in the ADAMS software for analyzing the behavior of a fuzzy logic vehicle dynamic control (VDC) system. This high-DOF model contains front and rear suspensions, the steering subsystem, the body subsystem, the powertrain subsystem, the braking subsystem, and the tire model.

In real-time development, there is always an important tradeoff between accuracy and computational complexity that needs to be considered. Therefore, the final model should be as simple as possible, while the results are accurate within reasonable error.

Chapter 3

Modeling and Computer Simulations

A suitable vehicle model is needed to conduct research and experiment about vehicle chassis control. This model is normally created based on the laws of mathematics and physics, using dynamic equations and the fixed parameters of the vehicle. The bicycle model is a good example to demonstrate vehicle body motion. An appropriate tire model should also be included, since all propulsion forces are transferred to the ground through the tires. This chapter briefly describes these dynamic models used for DCI modeling, as well as the simulation results based on this model.

3.1 Vehicle Model

For this study, the main goal was to maintain the accuracy of the force prediction while keeping the computation time short. This was made possible by choosing a model that has the least number of equations and avoids any unnecessary differentiation or integration. Therefore, a single-track vehicle model, known as the bicycle model in the field of vehicle dynamics, was used to accurately represent vehicle dynamics. The popularity of this model is because of its simplicity, and because it can be used in a closed form solution for the dynamics of a vehicle. It is repeatedly used in research literature [16, 17, 18, 19, 20].

The proposed bicycle model generates both linear forces and rotational moments with the help of the proper tire model. The following subsections describe the theory behind the bicycle model, as well as the tire model employed in this study. The coordinates defined for the vehicle are illustrated in Figure 3-1.

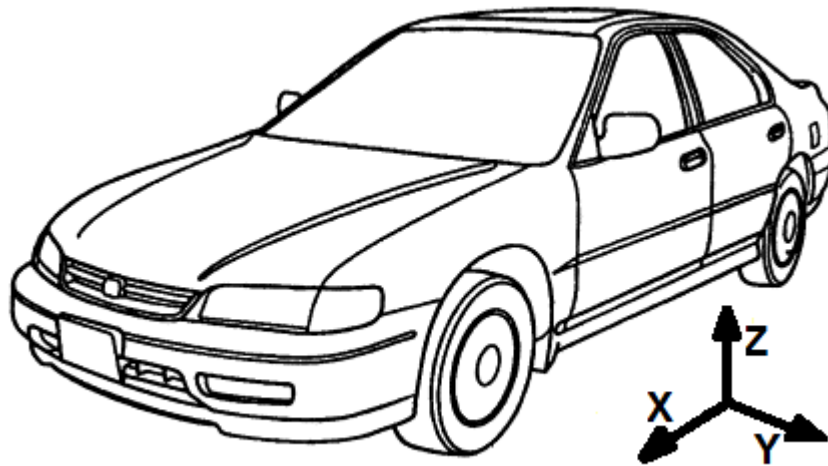


Figure 3-1: ISO coordinate system in vehicle dynamics [26]

This coordinate system is known as an ISO coordinate system in the field of vehicle dynamics. Figure 3-2 shows the ISO coordinate system relative to the tire forces of the four-wheel vehicle model. Parameters F_{xi} and F_{yi} are the longitudinal and lateral tire forces respectively, where $i = 1, \dots, 4$, denotes the number assigned to each wheel.

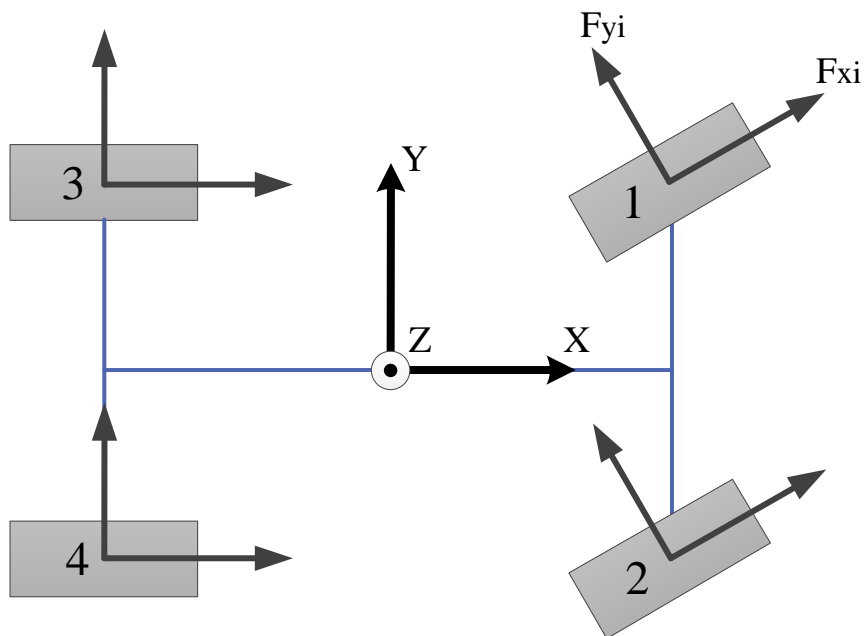


Figure 3-2: Four-Wheel Vehicle Model Coordinates

3.1.1 Bicycle Model

In this well-known single-track model, each pair of the wheels is simplified as one wheel, as shown in Figure 3-3. This model includes all longitudinal accelerations, lateral accelerations, and yaw moments. The weight transfer between the left and right wheels is not modeled [27].

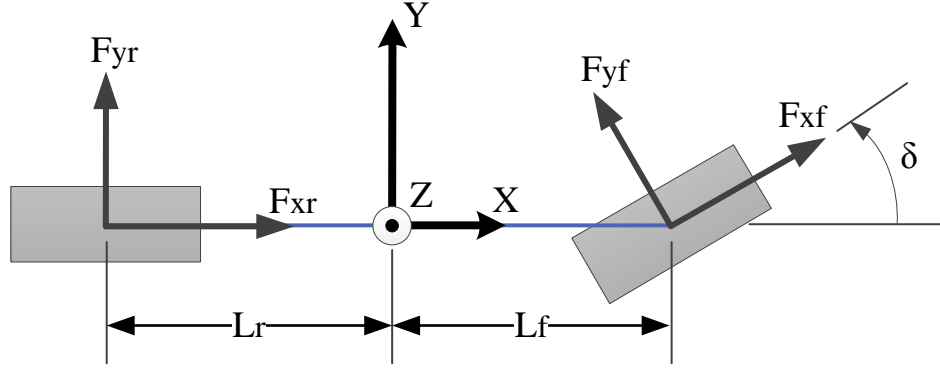


Figure 3-3: Single track bicycle model

This single track model is suitable for modeling simple vehicle actions, and its simple mathematical equations can keep computation times short compared to other dynamic models that are available. Equations (3-1) – (3-3) are the derived equations of motion for this bicycle model, and define the summation of the forces acting on the front and rear wheels, as well as the vehicle's rotation.

$$ma_x = F_{xf} \cos(\delta) - F_{yf} \sin(\delta) + F_{xr} \quad (3-1)$$

$$ma_y = F_{xf} \sin(\delta) + F_{yf} \cos(\delta) + F_{yr} \quad (3-2)$$

$$I_z \dot{r} = F_{xf} \sin(\delta) L_f + F_{yf} \cos(\delta) L_f - F_{yr} L_r \quad (3-3)$$

All of the parameters for these equations are defined in the nomenclature. Equations (3-4) and (3-5) define a_x and a_y in the global-coordinate frame considering the yaw.

$$a_x = a_x - V_y r \quad (3-4)$$

$$a_y = a_y + V_x r \quad (3-5)$$

Now, by combining the last five equations, we get the general equations of motion in the global-coordinate frame.

$$a_x = \frac{1}{m}(F_{xf}\cos(\delta) - F_{yf}\sin(\delta) + F_{xr}) + V_y r \quad (3-6)$$

$$a_y = \frac{1}{m}(F_{xf}\sin(\delta) + F_{yf}\cos(\delta) + F_{yr}) - V_x r \quad (3-7)$$

$$\dot{r} = \frac{1}{I_z}(F_{xf}\sin(\delta)L_f + F_{yf}\cos(\delta)L_f - F_{yr}L_r) \quad (3-8)$$

The slip angle of a wheel is the angle between the direction of a wheel heading and the direction of travel. Actual wheel velocity at the contact is determined by summing the velocity at the CG point with the velocities affected by the yaw rate. Figure 3-4 and equations (3-9) and (3-10) define the slip angles for both the front and rear wheels using trigonometry.

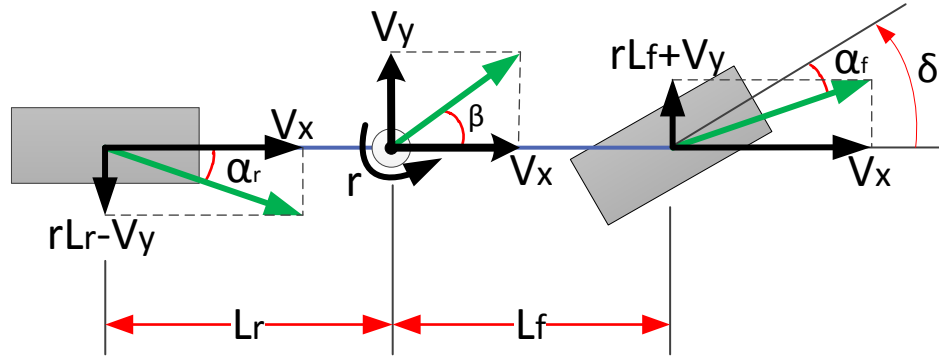


Figure 3-4: Velocity and moments acting on the bicycle model

$$\tan(\delta - \alpha_f) = \frac{rL_f + V_y}{V_x} \quad (3-9)$$

$$\tan(\alpha_r) = \frac{rL_r - V_y}{V_x} \quad (3-10)$$

From the above equations, the slips angles can be derived as:

$$\alpha_f = \delta - \tan^{-1}\left(\frac{V_y + rL_f}{V_x}\right) \quad (3-11)$$

$$\alpha_r = -\tan^{-1}\left(\frac{V_y - rL_r}{V_x}\right) \quad (3-12)$$

The vehicle side-slip angle (β) can be calculated by:

$$\beta = \tan^{-1}\left(\frac{V_y}{V_x}\right) \quad (3-13)$$

The next two equations define the slip angles of the front (α_f) and rear (α_r) tires in terms of the vehicle side-slip angle, assuming that the other two angles are small:

$$\alpha_f = \delta - \beta - \frac{rL_f}{V_x} \quad (3-14)$$

$$\alpha_r = -\beta + \frac{rL_r}{V_x} \quad (3-15)$$

The following section explains the tire model, which is essential for solving the general equations of motion, since the longitudinal and lateral forces should be derived from the vehicle wheels.

3.1.2 Tire Model

Frey defines the role of vehicle tires as follows: “The function of tires on vehicles is to support the weight of the vehicle, provide longitudinal and lateral tractive forces to accelerate and decelerate the vehicle, and help cushion the vehicle from the effects of road surface irregularities in order to improve driver and passenger ride comfort” [28].

One of the most challenging performance factors for designers is the longitudinal and vertical ride comfort of the vehicle. It has long been recognized that there is a need for pneumatic tire models to provide the transfer function between the vehicle and road in order to predict vehicle ride and comfort [28]. As described below, there are different linear and nonlinear tire models available in research literature.

The linear tire model only depends on the slip angle, and is the simplest model. The linear analysis of a tire model commonly considers constant side-force coefficients of tires at small ranges of force output. The linear tire model does not consider longitudinal tire forces due to the complex interactions between lateral and longitudinal tire forces. Thus, the linear tire model does not model the tire saturation, and is suitable for analyzing stable vehicle behavior under the assumption of reduced steering and acceleration.

Tire forces are determined from tire properties and slip models. The linear lateral tire forces, F_{yf} and F_{yr} , used in vehicle model equations are calculated from:

$$F_{yf} = C_{\alpha f} \mu \alpha_f \quad (3-16)$$

$$F_{yr} = C_{\alpha r} \mu \alpha_r \quad (3-17)$$

The “cornering stiffness” for the front tire ($C_{\alpha f}$) and rear tire ($C_{\alpha r}$) denote the slope of the curve of lateral force versus slip angle, evaluated at zero slip angles, as shown in Figure 3-5.

The intermolecular bonds between the rubber and the aggregate in the road surface introduce the road coefficient of friction (μ) or surface adhesion. The road surface and its condition have a direct effect on the friction coefficient, which has a value of 1 for dry roads, 0.3 for wet roads, and 0.1 for icy roads.

The non-linear tire model involves highly non-linear curve fitting of the tire data. However, the lateral force of the tire shows a linear increase as the slip angle increases up to a certain value.

Hans Bastiaan Pacejka is an expert in vehicle system dynamics, with particular expertise in tire dynamics; his works are now standard references in these fields. Pacejka has developed a series of tire design models, which are named “Magic Formula”, because there is no particular physical basis for the structure of the equations. Each tire is characterized by 10 to 20 coefficients. The nonlinear tire model used in this project is also similar to one of Pacejka’s magic formulas, which are defined based on parameters and constant values specified by the General Motors Corporation.

For the front or rear tires, longitudinal force is calculated using equation (3-18).

$$F_{x_i} = F_{X_i} \varphi_{x_i} \quad (3-18)$$

where F_{X_i} and φ_{x_i} are defined by formulas (3-19) and (3-20), respectively.

$$F_{X_i} = a_x F_{z_i} \mu \sin \left(b_x \tanh \left(\frac{c_x \kappa_i}{\mu} \right) \right) \quad (3-19)$$

$$\varphi_{x_i} = 1 - (\lambda_x \operatorname{sech}(\gamma_x \kappa_i) (\tanh(\beta_x \alpha_i))^2) \quad (3-20)$$

The lateral force is calculated using equation (3-21).

$$F_{y_i} = F_{Y_i} \varphi_{y_i} \quad (3-21)$$

As with the longitudinal force equation, the parameters in equation (3-21) are as follows:

$$F_{Y_i} = a_y F_{z_i} \mu \sin \left(b_y \tanh \left(\frac{c_y \alpha_i}{\mu} \right) \right) \quad (3-22)$$

$$\varphi_{y_i} = 1 - (\lambda_y \operatorname{sech}(\gamma_y \alpha_i) (\tanh(\beta_y \kappa_i))^2) \quad (3-23)$$

All of the coefficients used in the tire model are listed in appendix A. F_{z_f} and F_{z_r} are vertical forces that apply to the front and rear wheels, and can be calculated by equations (3-24) and (3-25).

$$F_{z_f} = \frac{L_r}{L_f + L_r} mg \quad (3-24)$$

$$F_{zr} = \frac{L_f}{L_f + L_r} mg \quad (3-25)$$

The curve shown in Figure 3-5 illustrates the nonlinear tire model and its properties:

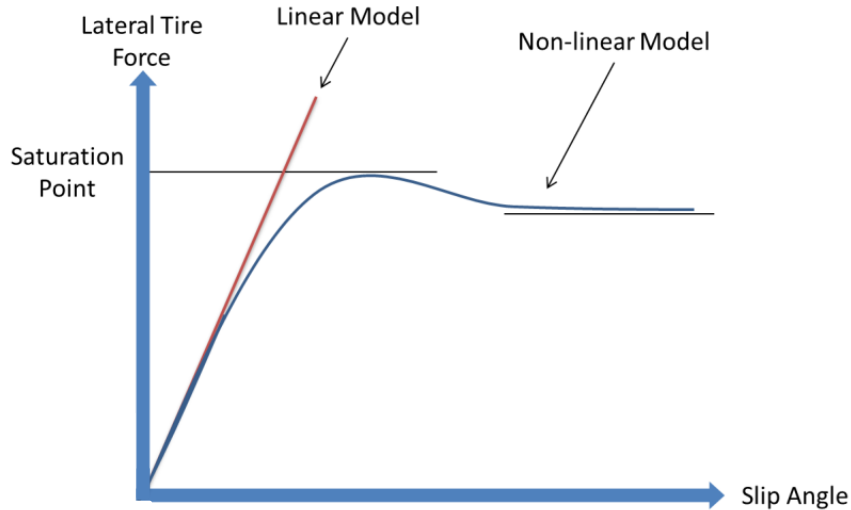


Figure 3-5: Linear and Nonlinear Tire Model Curves

Relaxation length is another topic that was not considered in this study, but is a promising consideration for future work. Relaxation length is the distance that a wheel has travelled during the time it takes to develop the lateral force on the wheel [27]. An alternative definition for relaxation length is described by Maurice et al. as follows: “the distance needed by the tire to reach a certain percentage of the steady-state situation after a step-wise change in the slip angle” [29]. The shorter the relaxation length, the better handling the tire provides for the driver. Adding relaxation length to the tire model improves the accuracy of the forces generated by the model, and enables the proper modeling of the delay between the time that the driver turns the steering wheel, to the time that the car actually turns.

As aforementioned, the purpose of the DCI is to generate the desired forces based on driver inputs. To represent the driver’s desire to have the feeling of driving on a dry road, the road adhesion friction is assumed to be 1.

3.1.3 Resistive Forces

There are different environmental factors that affect a vehicle’s operating performance when moving on the road, such as wind forces, the ground-surface condition, and road grade. Air drag

and rolling resistance are the two main factors considered in this study. This section describes the formulation of these resistive forces, their calculation formulas, and associated assumptions.

3.1.3.1 Air Drag Force

Air drag, also known as aerodynamic drag, is an important resistive force that fights against any object moving forward through the air. Air drag depends directly on the velocity of the moving body. In vehicle design, one of the challenges for engineers is to design the vehicle body so as to minimize the magnitude of this resistive force [28].

Longitudinal, lateral, and vertical drag forces are three separate forces applied to the vehicle body, which creates overall air drag. These three vectors are usually calculated at a specific point called the aerodynamic reference point, defined in the sprung-mass coordinate system. Figure 3-6 shows the air drag applied to the vehicle body and how it flows over the car.

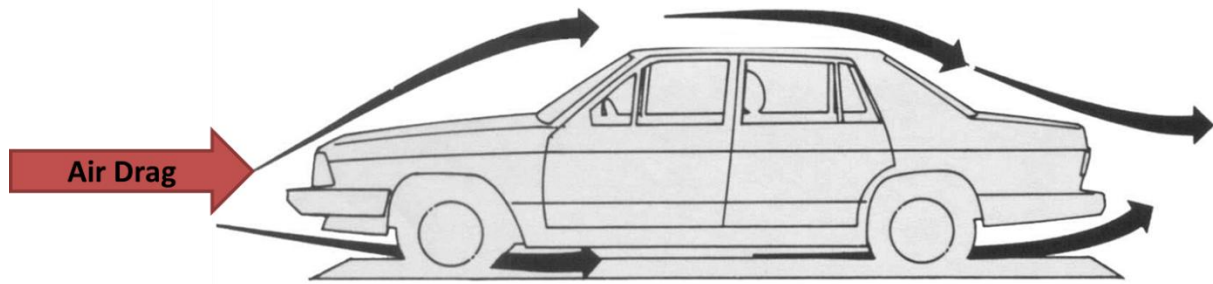


Figure 3-6: Air flow over the vehicle [29]

The drag forces are calculated as functions of the aerodynamic side slip angle β , shown in Figure 3-7. The equations related to these three forces are presented below:

$$F_x = -C_x(\beta_{air})A_fQ \quad (3-26)$$

$$F_y = -C_y(\beta_{air})A_fQ \quad (3-27)$$

$$F_z = -C_z(\beta_{air})A_fQ \quad (3-28)$$

where:

$$Q = \frac{1}{2}D_{air}V_{air}^2 \quad (3-29)$$

The dimensionless coefficients C_x , C_y , C_z are defined as tabular functions of aerodynamic side slip angle (β_{air}). For this study, the values of these coefficients were extracted from Figure A-3 to

Figure A-5, shown in appendix D [30]. A_f , also called the frontal area of the vehicle, is the projected area of the vehicle in the direction of travel, and was reported as 1.6 [m²]. The air mass density (D_{air}) was assumed to be 1.225 [Kg/m³]. Air density is affected by environmental conditions, which means that different aerodynamic drag applies in altered conditions. A temperature of 15°C and a barometric pressure of 101.32 [kPa] are frequently used as standard conditions [13].

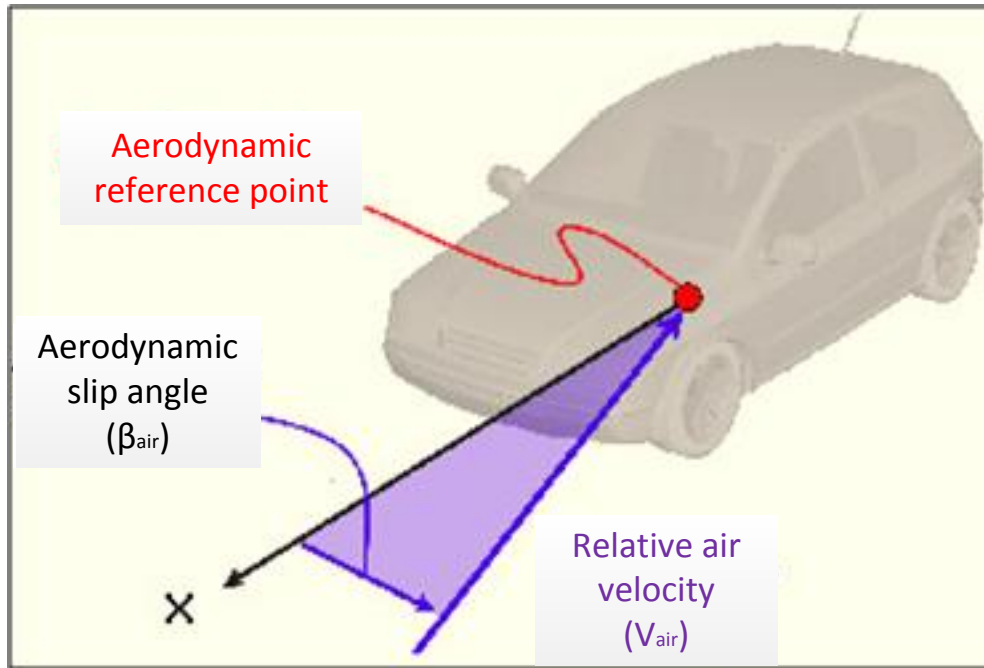


Figure 3-7: Aerodynamic slip angle relative to vehicle longitudinal axis [30]

3.1.3.2 Rolling Resistance

Rolling Resistance, also called rolling friction, is the force against the motion of an object rolling on a surface. When the tire rotates on the road, part of the contact patch is vertically deflected, and then springs back to its original shape. Part of the energy spent due to this internal damping is not completely recovered, and acts as an opposite force in the motion of the vehicle, called rolling resistance [13].

The deformation of the wheels and the roadbed surface are contributing factors to rolling resistance. Wheel diameter, the speed load on the wheels, and surface adhesion are additional contributing factors.

Rolling resistance is typically modeled as being proportional to the wheel normal force. Therefore, it is often expressed as coefficient multiplied by the normal force. The rolling resistance coefficient is the force needed to push the wheeled vehicle forward per unit force of weight. It varies in the range of 0.01 to 0.04 based on the ground condition. Table 1 shows the different rolling resistance coefficients for passenger cars.

Table 1: Some typical rolling coefficients [31]

Rolling Resistance Coefficient (C_{rr})	Description
0.01 – 0.015	Car tire on concrete
0.03	Car tire on tar or asphalt
0.04 – 0.08	Car tire on solid sand
0.2 – 0.4	Car tire on loose sand

Equation (3-30) is used to obtain the rolling resistance force, where the normal force of the tire can be obtained from (3-31):

$$F = C_{rr}N \quad (3-30)$$

$$N = mg \quad (3-31)$$

Since the role of the DCI is to generate desired forces of the vehicle moving on a dry asphalt road, the rolling resistance coefficient is selected to be 0.03.

3.2 Computer Simulation

To validate the desired forces obtained from the driver command interpreter, the forces out of the interpreter module were compared with the output forces at the CG point of the vehicle, when the driving scenario was set to perfect driving conditions.

Figure 3-8 shows the structure of the computer simulation setup. The inputs to the CarSim and DCI were the same, while the proposed stability controller was disabled. The road and tire conditions were assumed to be perfect.

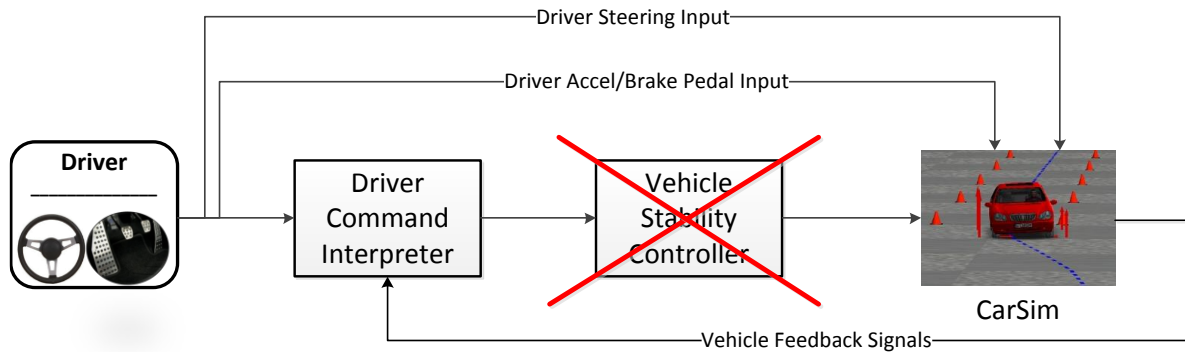


Figure 3-8: Computer simulation framework

3.2.1 CarSim Software

The validation of the driver command interpreter model should be checked against a reliable source that gives signals identical to those of the actual vehicle. There are many different software packages in the market for researchers to use for this purpose, such as CarSim, ADAMS, and DADS; in this study, CarSim was used as a reference vehicle model predictor [32].

CarSim is a commercial software package for studying detailed vehicle dynamics, developed by one of the company founders at University of Michigan Transportation Research Institute (UMTRI). CarSim predicts the performance of vehicles in response to driver controls such as steering, throttle, and brakes, in an environment specified in terms of properties such as road geometry and coefficients of friction. This software is used by many automotive manufacturers such as General Motors, Ford, Toyota, and Honda. Many suppliers, research labs, and universities employ this software in experiments that compare theoretical results with actual results obtained through physical tests [30].

3.2.2 Modeling Opel Corsa in CarSim

An Opel Corsa hatchback was modeled by plugging appropriate engineering measurements into the CarSim software to obtain a complex high-DOF model.

Figure 3-9 shows the main configuration page for the vehicle in CarSim. Different parameters can be edited for the subsystems shown in this page. Figure 3-10 shows the configuration page for the sprung mass subsystem, where all of the parameters and coordinates for the vehicle body and its

CG location are set. These constant values should be identical to the parameters used in the DCI and controller algorithms.

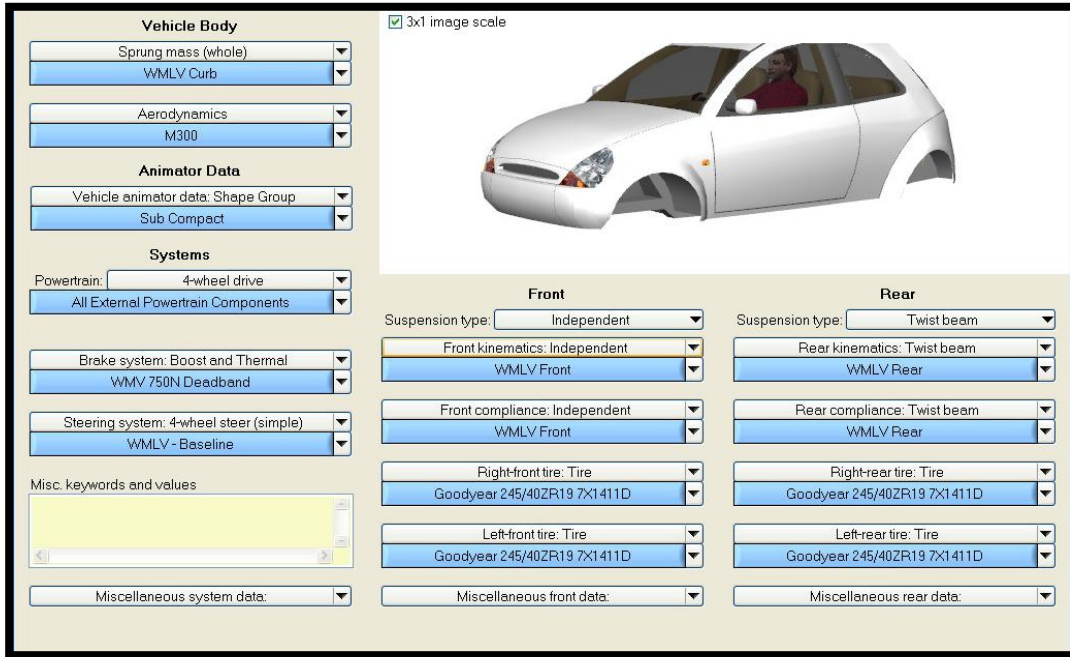


Figure 3-9: CarSim main vehicle configuration page [30]

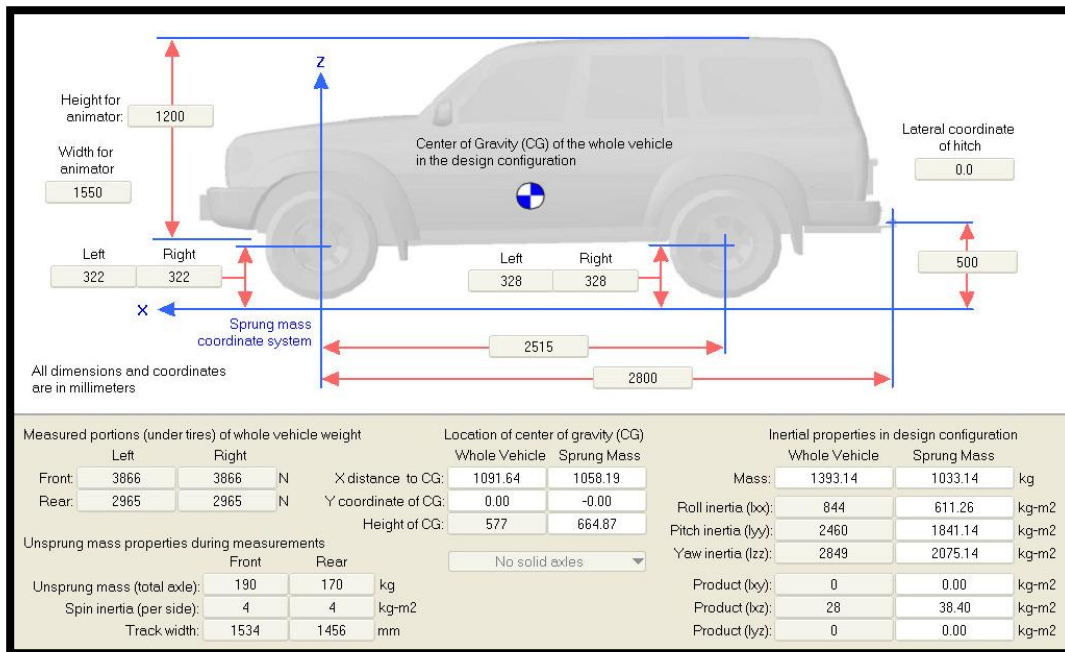


Figure 3-10: CarSim vehicle model specifications [30]

The CarSim/Simulink interface shown in appendix E depicts how the DCI block containing the proposed model and the CarSim s-function vehicle model are connected. The scope on the top right corner shows the location where the DCI generated forces and CarSim vehicle forces at the CG were compared and verified.

3.2.3 Test Scenarios and Results

CarSim has predefined test procedures for different stability tests, such as vehicle spin and roll over. For the purpose of this study, which concerns lateral stability control, two scenarios were chosen for evaluation: the Double-Lane-Change (DLC) scenario, and another custom-defined stability test offered by General Motors. Both of these scenarios are strong enough to excite the vehicle chassis in the lateral direction.

Figure 3-11 shows the predefined trajectory for the DLC scenario. CarSim determines the required steering angle input based on this path, which should be followed by the vehicle model. The driver preview time was set to be 1 sec, and the time lag was neglected.

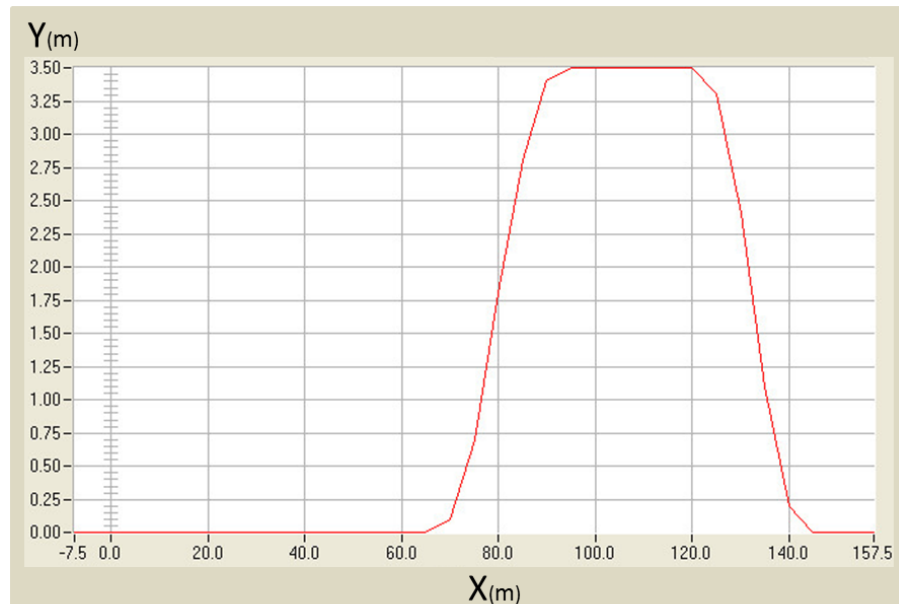


Figure 3-11: CarSim DLC predefined trajectory [30]

The initial speed of the vehicle was set to be 60 [km/h] with a decrement of 7 [km/h] until the end of the scenario. No torque was applied to the vehicle from the driver. The total time of this scenario was 13.2 seconds, and double-lane-change steering was applied at the 3rd second for about 9

seconds. Figure 3-12 and Figure 3-13 depict the driver's steering input and the vehicle's longitudinal velocity.

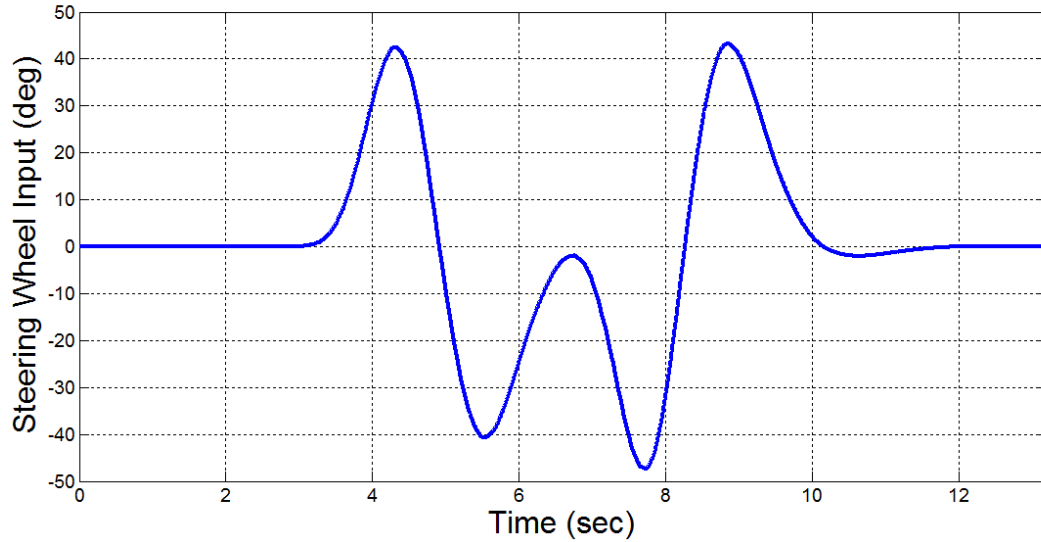


Figure 3-12: DLC Computer Simulation Input Steering Angle

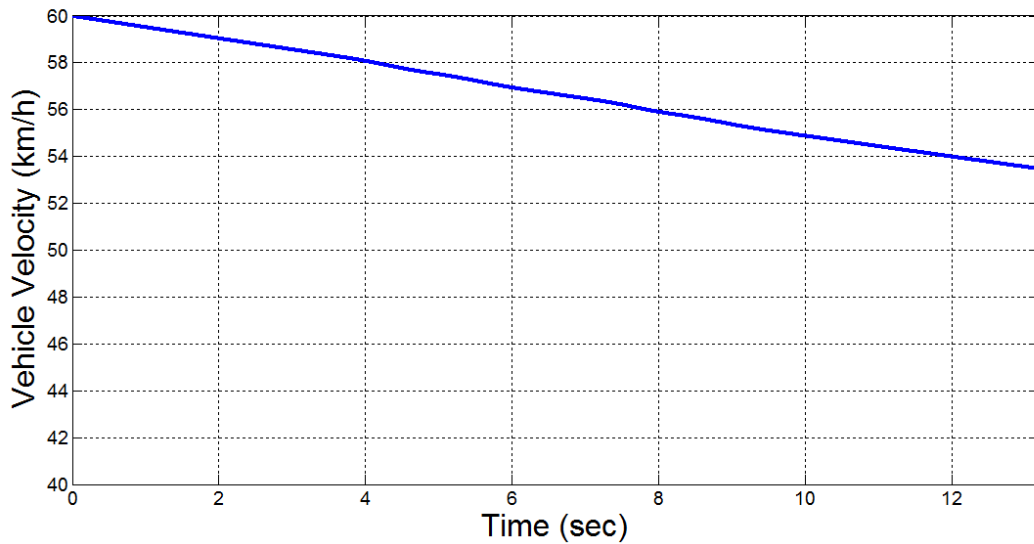


Figure 3-13: DLC computer simulation vehicle forward velocity

Figure 3-14 to Figure 3-16 show the longitudinal force, lateral force, and yaw moment of the vehicle at the CG point, where the blue line shows the result from the CarSim model, and the red dashed line represents the DCI's results.

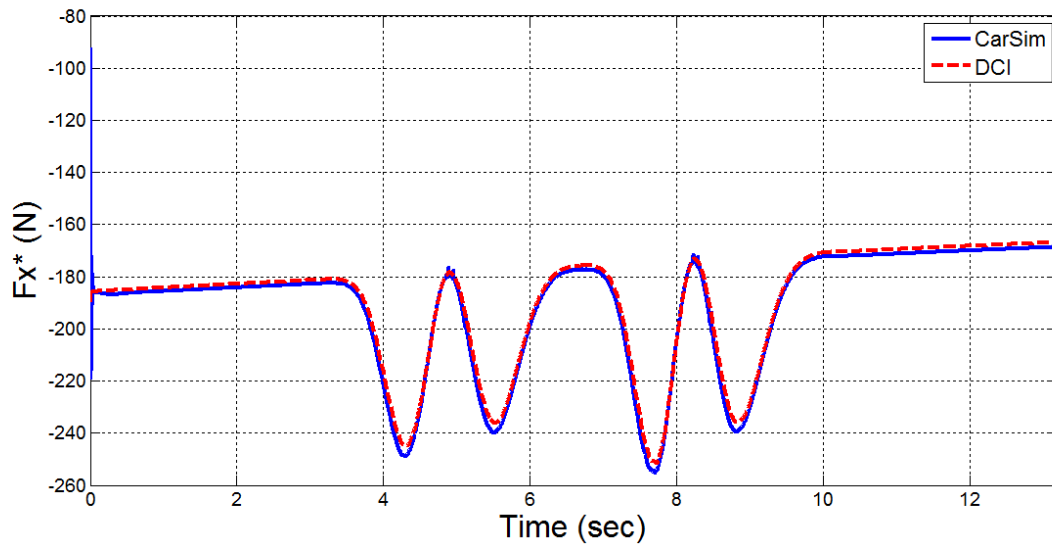


Figure 3-14: DLC computer simulation forward force at CG point

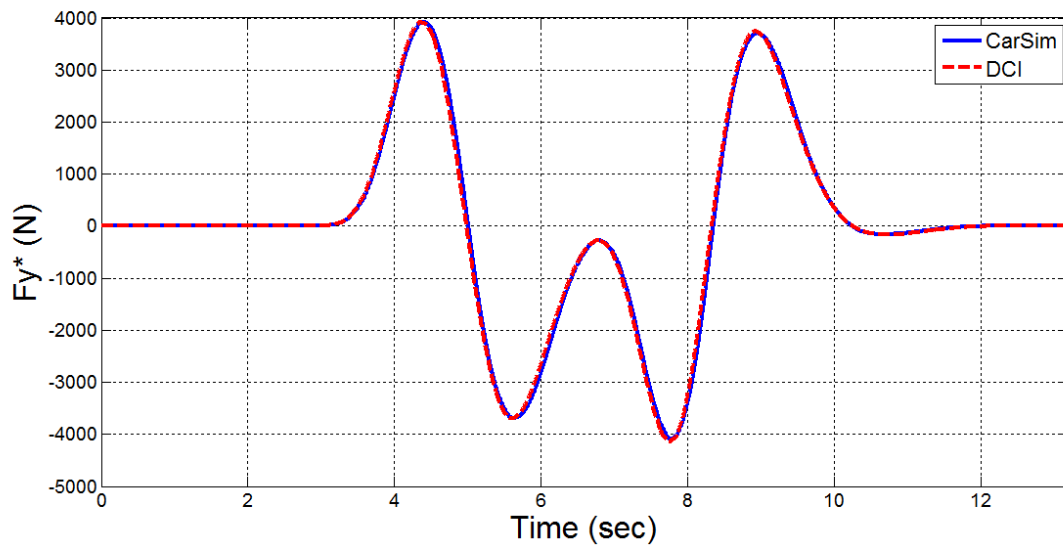


Figure 3-15: DLC computer simulation lateral force at CG point

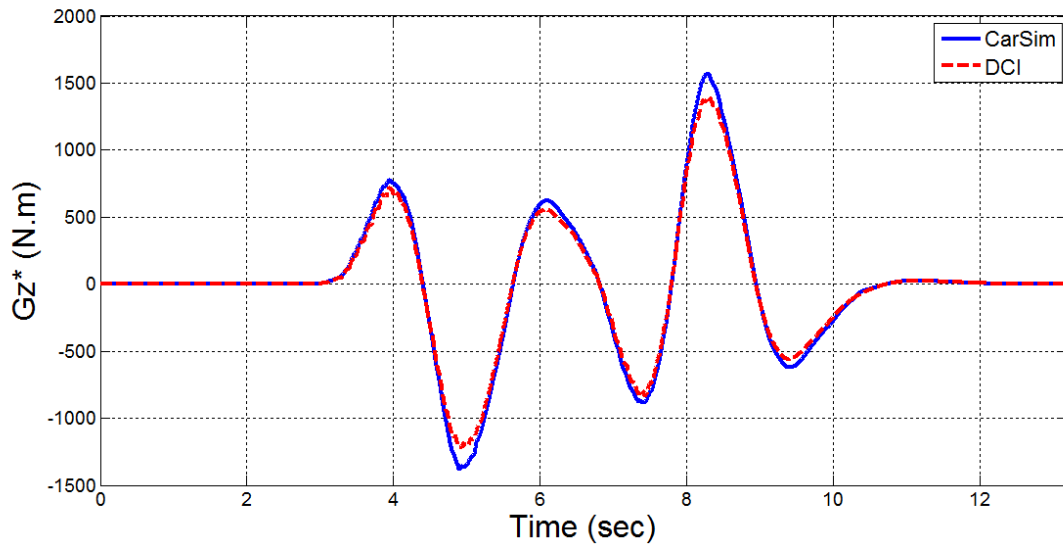


Figure 3-16: DLC computer simulation yaw moment at CG point

The two lines generally agree; the small discrepancies are due to the difference between the complexities of the two models, which are 5-DOF DCI and high-DOF CarSim.

The second maneuver was defined by General Motors. During this 15-second test, a semi-sinewave steering input was applied between 0.5 to 3.1 seconds, followed by sudden braking from 8.03 to 10.03 seconds, and finally followed by an application of deceleration up to the end of the maneuver. Figure 3-17 shows the torques applied to the front wheel and rear wheels. The torque magnitudes given are for a single wheel, which means that the magnitude values were multiplied by two to be used as inputs for the DCI. Figure 3-18 and Figure 3-19 show the driver's steering input and the vehicle's forward speed during this maneuver.

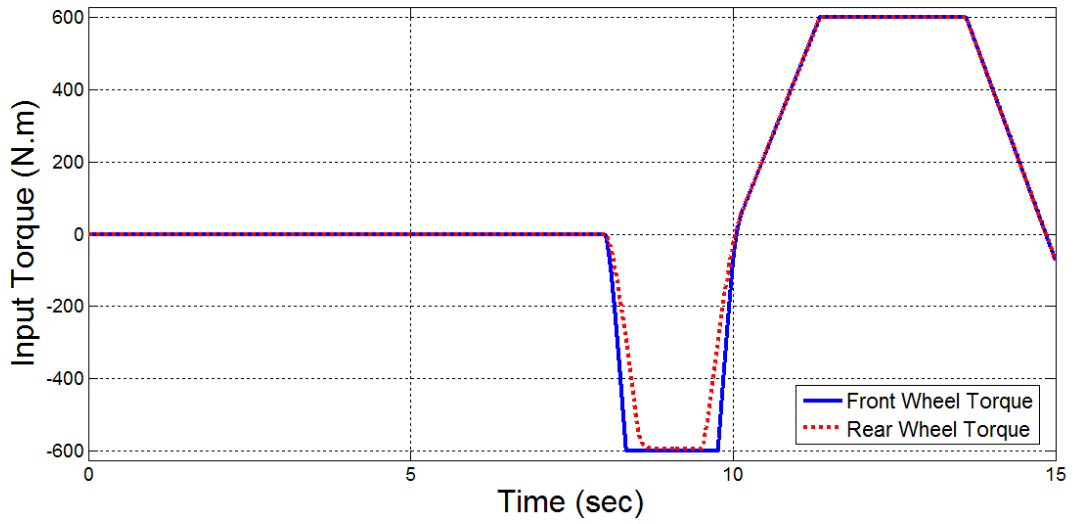


Figure 3-17: Stability test computer simulation input torques

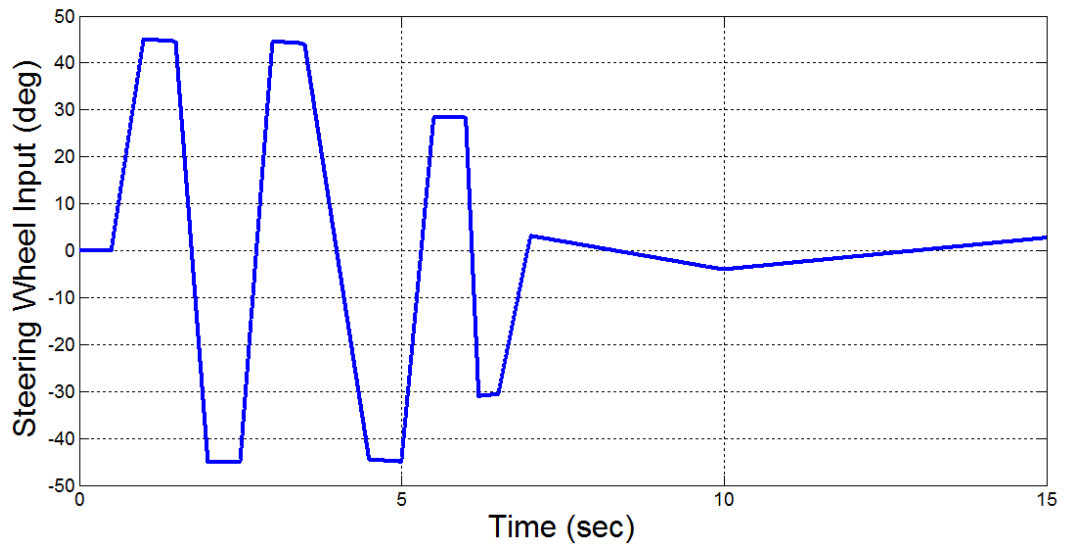


Figure 3-18: Stability test computer simulation input steering angle

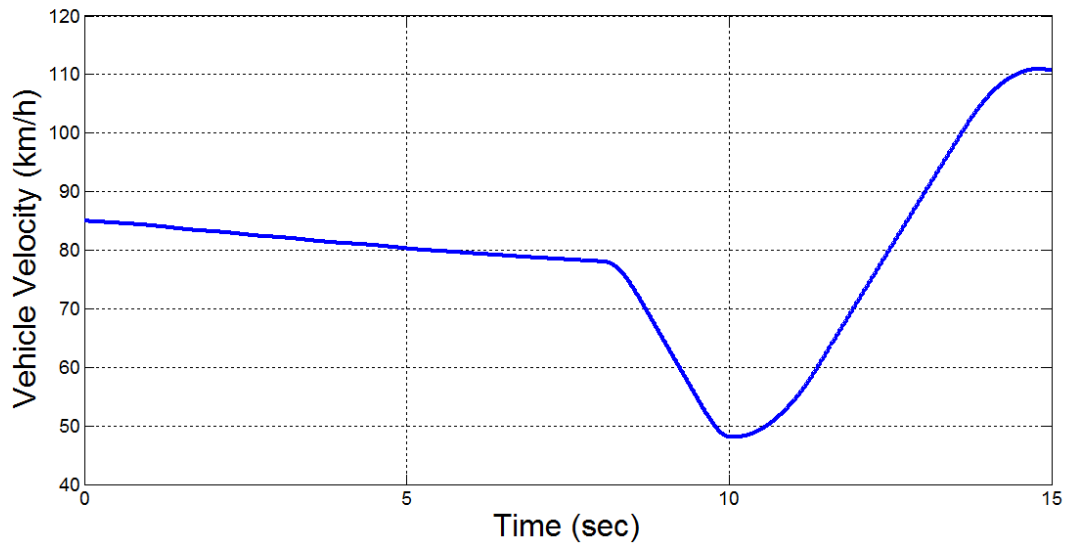


Figure 3-19: Stability test computer simulation vehicle forward velocity

Figure 3-20 to Figure 3-22 show all three forces and the moment calculated at the CG location of the vehicle. The CarSim and DCI results agree for the longitudinal and lateral forces. The same is generally true for the yaw moment curves, except for small differences at the peaks of the curves, which are due to the repeated vibrations caused by the driver's steering. Looking at the period between the 6th and 8th seconds, the differences disappear as the vehicle's body settles into normal conditions.

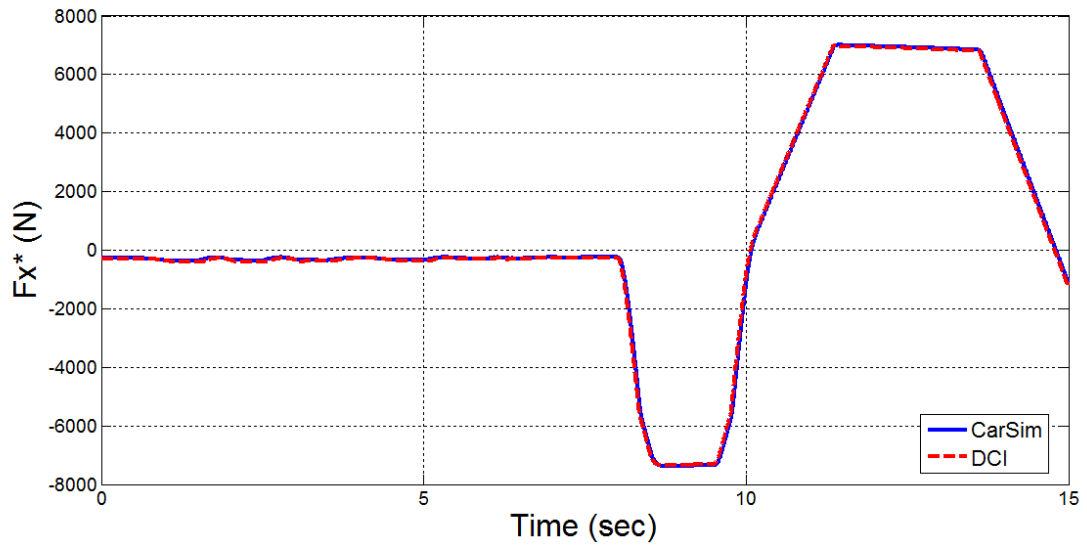


Figure 3-20: Stability test computer simulation forward force at CG point

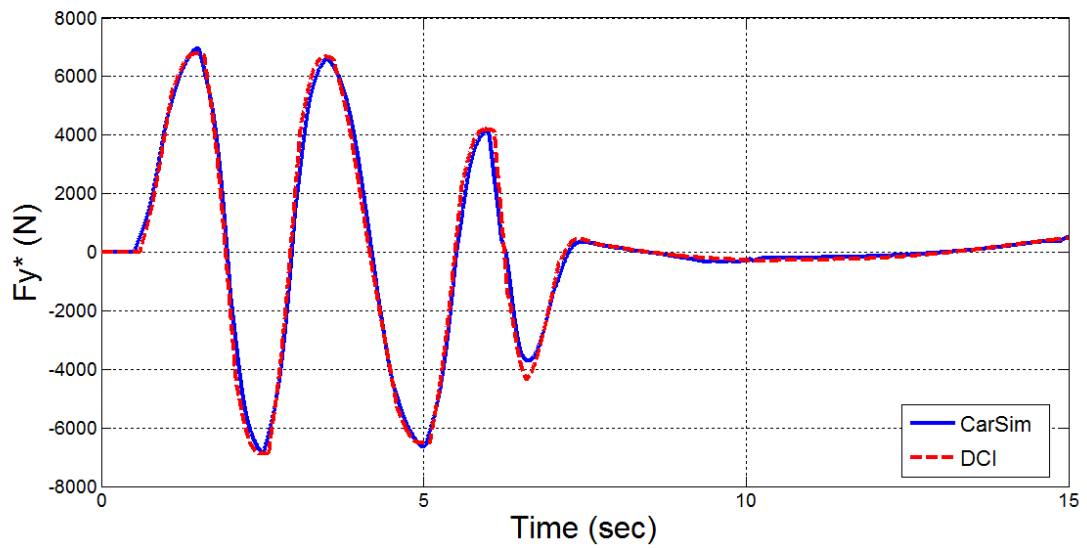


Figure 3-21: Stability test Computer simulation lateral force at CG point

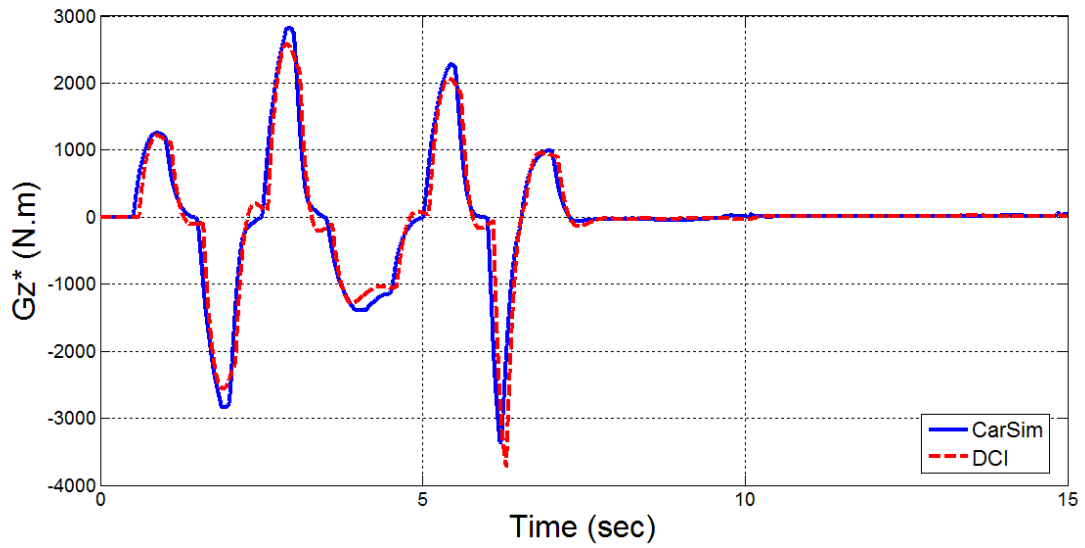


Figure 3-22: Stability test computer simulation yaw moment at CG point

After verifying the model through computer simulation, the Hardware-In-the-Loop (HIL) step was conducted. To prevent from any unexpected damage or accident, HIL must be performed before any real road test.

Chapter 4

Hardware-in-the-loop Analysis

This chapter presents descriptions about the test vehicle and its hardware components, as well as details about issues encountered during the code compilation on the vehicle, and the effective solutions established for them.

4.1 Hardware Description

There were two electric vehicles available to the research team. One of them was the Four-Wheel-Drive C-class Opel Corsa, and the other one was the Rear-Wheel-Drive SUV-class Chevrolet Equinox. Figure 4-1 shows the Opel Corsa hatchback, which was selected to be used for validation of the DCI because a fully independent torque adjustment was needed at all four wheels for the proposed controller. However, the stability controller algorithm was later modified to work on the available SUV vehicle, which also confirmed good results from the DCI.



Figure 4-1:4WD electric-driven Opel Corsa with four in-wheel motors

The standard combustion engine and powertrain, plus the driving shafts and wheel discs of this compact-sized vehicle were removed from the vehicle and replaced with four independent electric-drive in-wheel motors for each wheel. This kind of motor is also called the wheel hub motor or wheel hub drive. There are several concept cars that have been developed using in-wheel motors, such as Protean Electric's Mini QED, the Mitsubishi MIEV, and the Peugeot BB1 [33, 34, 35].

4.1.1 Propulsion System

In the test vehicle, the propulsion system consists of batteries, chargers, four independent electric motors, and motor drivers.

Four axial-flux, permanent magnet, synchronous AC Direct-Drive wheel motors were installed on the wheel hubs. Each motor has a maximum torque generation of 800Nm with 350A, and has 60 kW peak power at 1200 rpm. One of the motors installed on the vehicle is shown in Figure 4-2.

These motors are used to produce the positive and negative traction torque requested by the driver, and the adjustment torques requested by the integrated controller. When compared with DC motors, AC motors have been found to be advantageous in terms of demonstrating higher efficiency, higher power density, lower operating costs, lighter weight, and little to no need for maintenance. Additionally, synchronous AC electric motors benefit from a smaller size, higher power density, lower cost, and higher efficiency when compared to other available AC electric motors.

Figure 4-3 clearly explains the reasons for using large rims and tires for this vehicle. The custom made electric motors are slightly large, and adequate spacing to fit them in the rims was created using the 19 [in] rims.

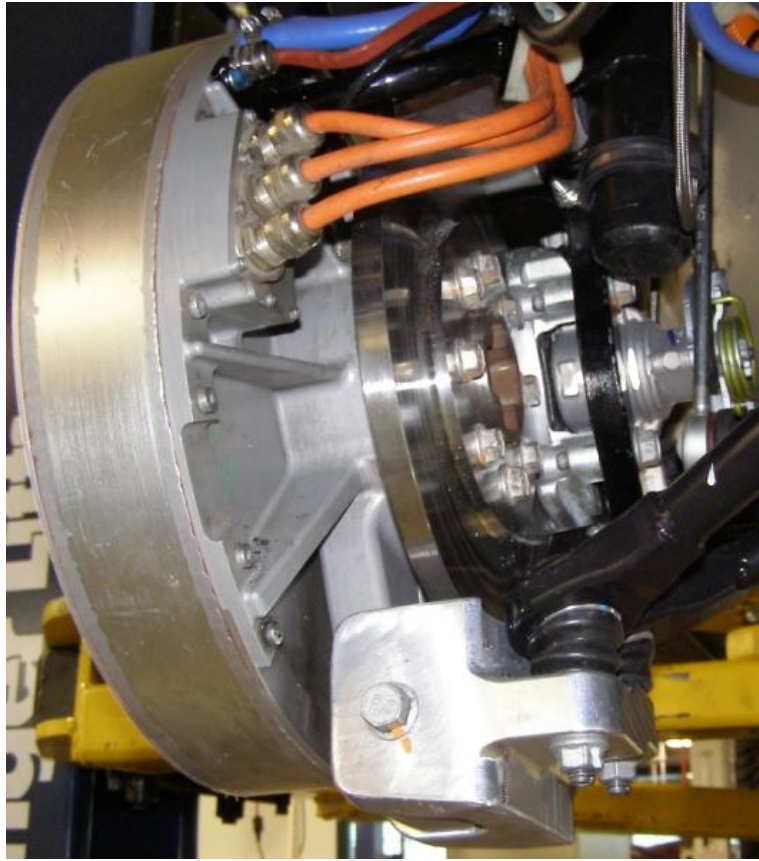


Figure 4-2: Electric In-Wheel Hub



Figure 4-3: In-wheel electric motor fitted in to the rim

There are four Power Inverter Modules (PIMs) in the vehicle, separately connected to the motors. The PIM consists of different subcomponents such as the motor control and motor drive, among others.

The motor control function, which can be defined as DC to AC inversion and AC to DC conversion, is to take the request torque magnitude and direction as inputs and produce a low voltage Pulse-Width Module (PWM) signal as output. This torque control function is designed to operate in motoring, rollback, and regenerative modes.

There are three conditions defined for PIM operation:

- When input voltage is lower than 180 volts or higher than 425 volts, the system should not be operational
- When input voltage is between 200 to 240 volts, the propulsion system should be operational, but at a reduced torque
- When input voltage is between 240 to 408 volts, the propulsion function should be fully operational

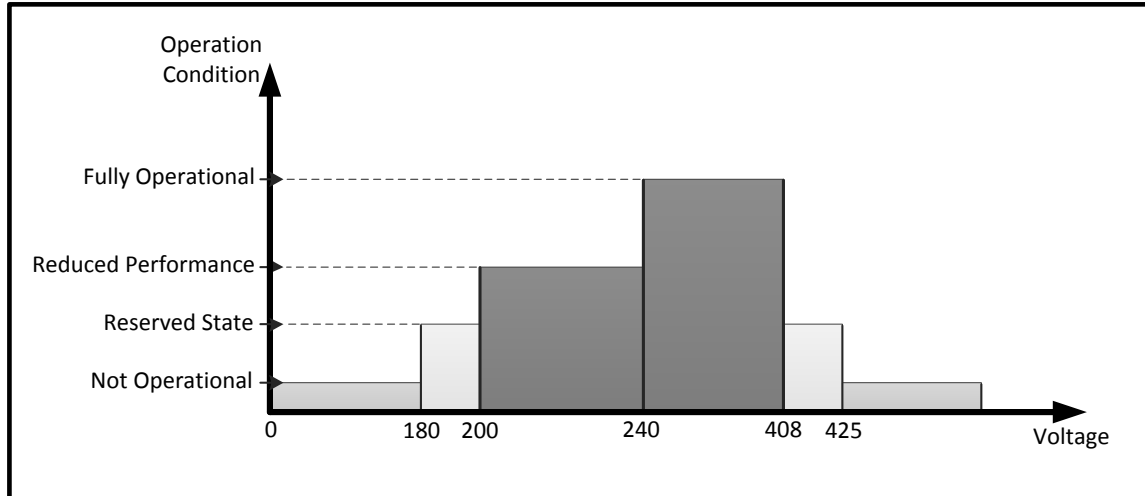


Figure 4-4: PIM Operation Range

The function of the motor drive is to get the low voltage PWM signal from the Motor Control, and produce a 3-phase high frequency, high voltage PWM motor voltage for production of torque at the output shaft.

This PIM is capable of the following:

- Converts high voltage DC power from the battery into high voltage AC propulsion power for the drive unit (motor)
- Converts the AC propulsion power from the drive unit (regenerative) to high voltage DC power
- Filters the high voltage DC power
- Communicates with external components via serial link
- Positive torque command produces clockwise torque on the electric motor, as viewed from inside the motor, looking out at the shaft towards the driveline

4.1.2 Brake System

The braking system in ICE vehicles is commonly friction-based, and includes hydraulic actuator and disc braking components. The Regenerative Braking System (RBS), on the other hand, converts kinetic energy gained from the negative torques of the wheels and recovers the electrical energy, which is saved back in the power supply. The capability of the electric traction motor to behave as a generator is required to dissipate the kinetic energy.

When having the parallel friction brake and RBS in the system, the regenerative braking algorithm receives brake pressure commands as a signal from a pressure sensor in the master cylinder. An electric brake torque is obtained from this signal, which is applied by the motors to assist the hydraulic brakes [36]. Figure 4-5 depicts the overall brake system considered for the proposed test vehicle.

Figure 4-6 shows that the friction brake hydraulic pump and its control box are mounted on the floor behind the driver's seat. The hydraulic pressure produced by this pump is transferred to the brake calipers through the hydraulic brake line passing under the vehicle body, as depicted in Figure 4-7:

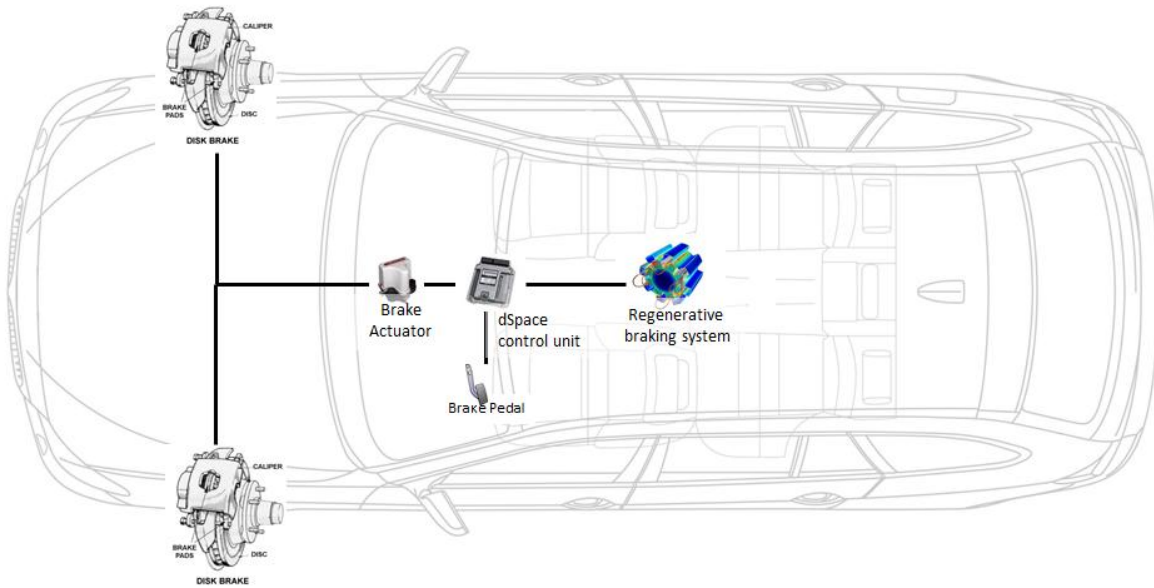


Figure 4-5: Parallel friction and regenerative braking system

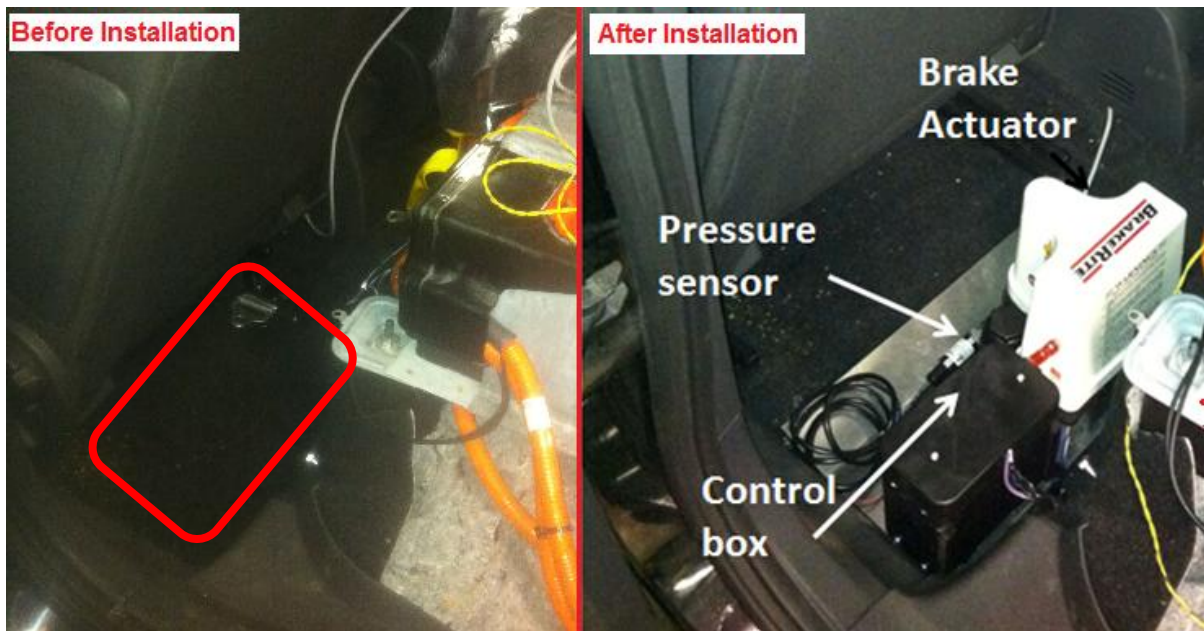


Figure 4-6: Friction brake hydraulic pump and control box



Figure 4-7: Hydraulic brake line

Figure 4-8 shows the in-lab setup for the verification and power test of the hydraulic pump prior to its installation on the vehicle, while Figure 4-9 depicts the results in the form of pump output pressure [psi] versus the time for different command voltages.



Figure 4-8: Brake pressure pump and sensor test setup

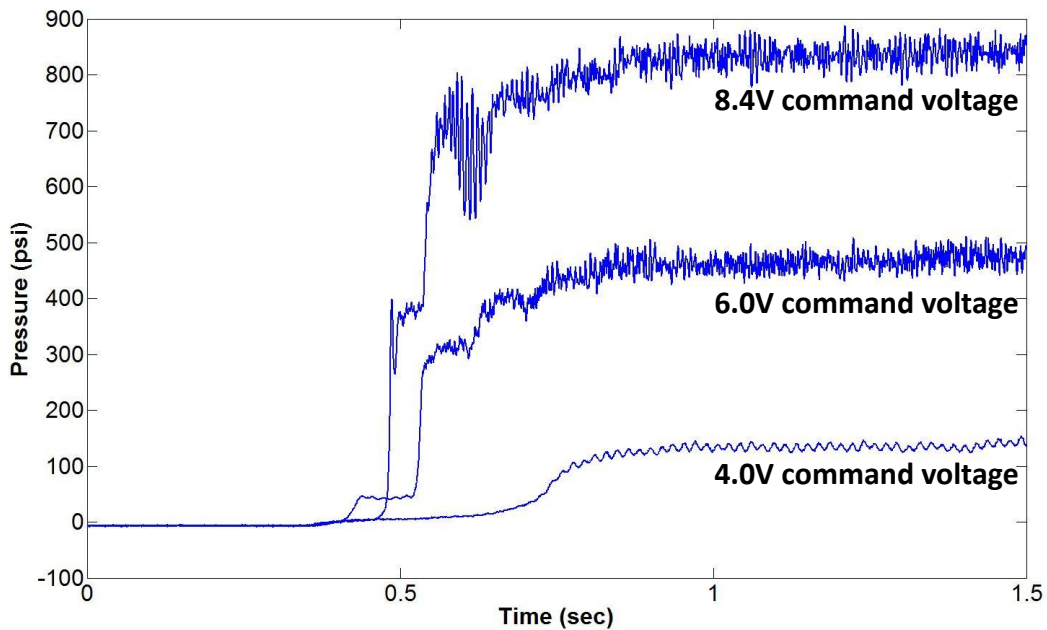


Figure 4-9: Hydraulic pump pressure at different voltages

Appropriate lookup tables based on the hydraulic pump performance, required braking torque, and stopping distance of the vehicle have been created and loaded on the vehicle’s MicroAutoBox controller. Figure 4-10 depicts the corresponding PWM inputs versus the braking torque, as obtained by experiment:

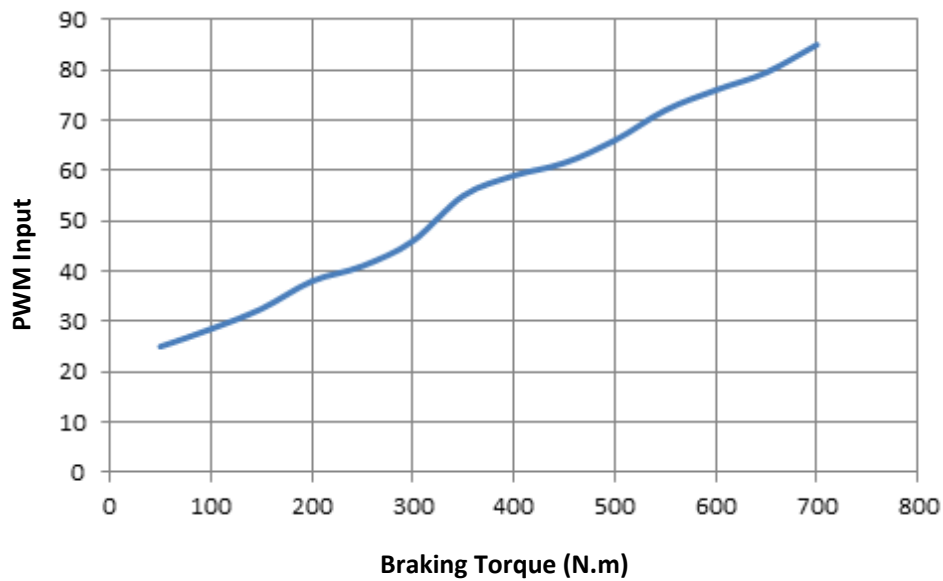


Figure 4-10: Friction Brake Mapping

4.1.3 Control System

dSPACE MicroAutoBox is a real-time system for performing fast function prototyping. It operates without user intervention, and can be used for many different rapid control prototyping applications, such as chassis control, powertrains, body control, and x-by-wire applications. The strength of the MicroAutoBox hardware is its unique combination of high-performance and comprehensive automotive I/O, and an extremely compact and robust design. It lets researchers equip different vehicles to check the reliability of their control functions. MicroAutoBox offers interfaces for all major automotive bus system: CAN, LIN, K/L-Line and FlexRay [37].

The available electronic control unit installed in the test vehicle has an 800 MHz processor and 8 MB memory, while the MATLAB/Simulink modeling tools are integrated into the dSPACE prototyping environment. The connection between the dSPACE hardware and the modeling tool through dSPACE's Real-Time-Interface (RTI) software make it possible for developers to implement their Simulink models on the MicroAutoBox automatically, without the need for professional programming skills [38].

MicroAutoBox Break-Out Box is an important accessory for working with MicroAutoBox. It provides easy access to all signals on the I/O connectors of the MicroAutoBox. Signals can be observed and reconnected through this break-out box without any change to existing cable harness. Different I/O ports can be found on the break-out box. One of these ports is called the Controller Area Network (CAN), which is used as a standard in the automotive industry to exchange data between different ECUs. For example, CAN bus may be used to connect engine and transmission control units.

Controller Area Network (CAN) Bus is an International Standardization Organization (ISO) defined serial communications bus originally developed to replace the complex wiring harness in the automotive industry with a two-wire bus . It was initially created by Robert Bosch, a German automotive system supplier, in the 1980s as a method for enabling robust serial communication. Later, the CAN protocol gained widespread popularity in industrial automation and was used in different applications in other markets.

Unlike other conventional networks such as USB or Ethernet, CAN does not send the block of data address-based from one node to another. In this message-based network system, data is available to the entire network and all nodes of the system. It is the responsibility of the nodes to either keep the message for the process or discard it immediately. An additional benefit of this

message-based protocol is that the extra nodes can be added to the system without reprogramming current nodes to recognize the new ones.

Controller Area Network (CAN) is used for command, status, and fault reporting communication between different vehicle controllers such as driver pedals, braking systems, and PIM [39, 40].

Vehicle Programming/Diagnostic Interface Panel allows users to configure the vehicle computer through communication with hardware such as dSPACE and CAN, which are located in the trunk. Data processed through MicroAutoBox are available to be observed and logged real-time by an external computer (e.g., a laptop) through this connection. This module is located in the passenger glove-box shown in Figure 4-11.



Figure 4-11: Diagnostic Interface Panel

In addition to the standard instrument cluster, which mainly contains the speedometer, this car has a Graphical User Interface (GUI) located in front of the center panel, as seen in Figure 4-12.



Figure 4-12: Graphical User Interface

This multilayer GUI has a separate power switch and can work without switching the vehicle on. Figure 4-13 to Figure 4-15 show the information that can be obtained from different layers of this display. The first screen is the general state of components such as the batteries, motors, and gear selector. Motor torques can be seen in the second screen, and the vehicle dynamic motions are displayed in the third screen.

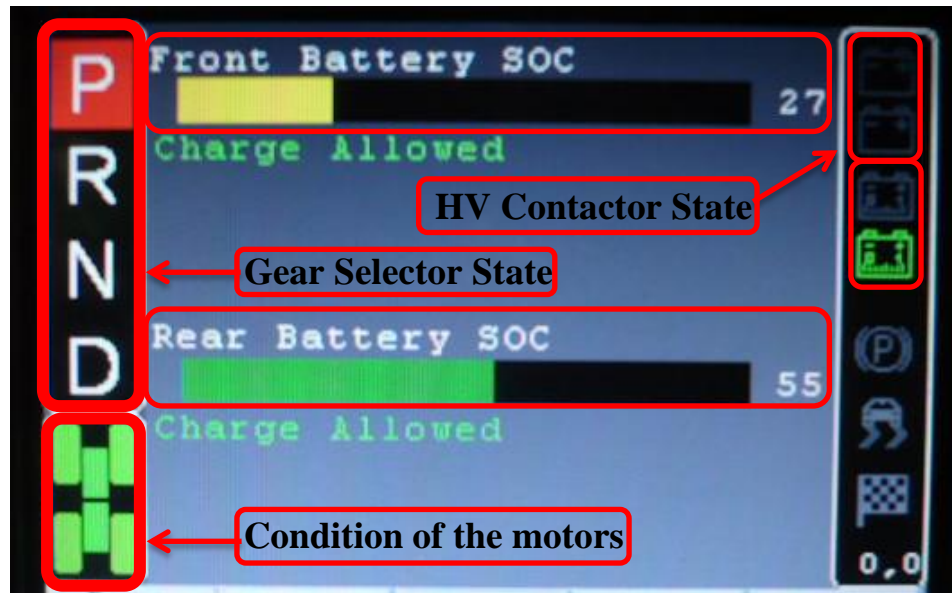


Figure 4-13: GUI first layer

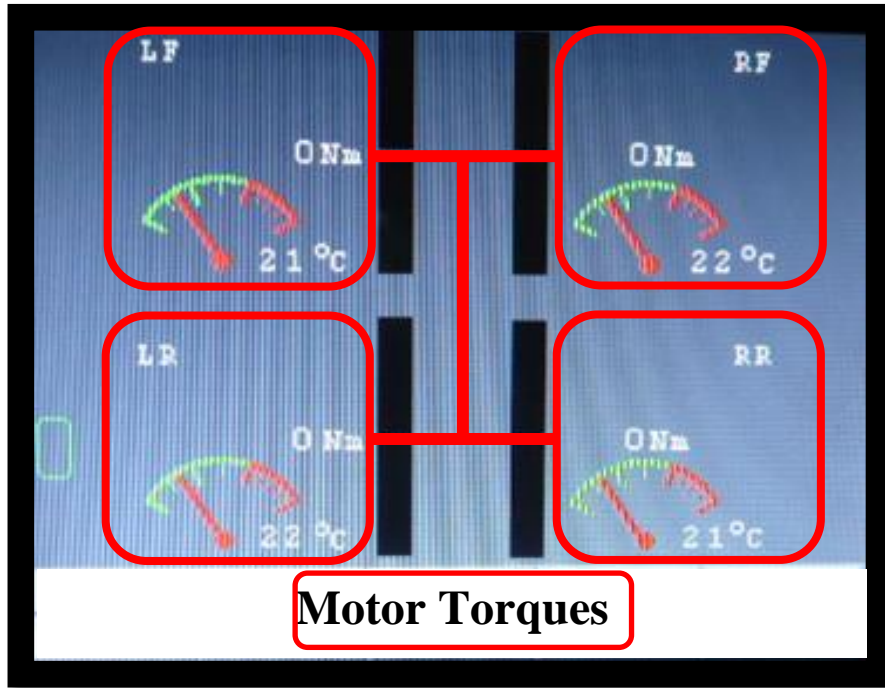


Figure 4-14: GUI motor information screen

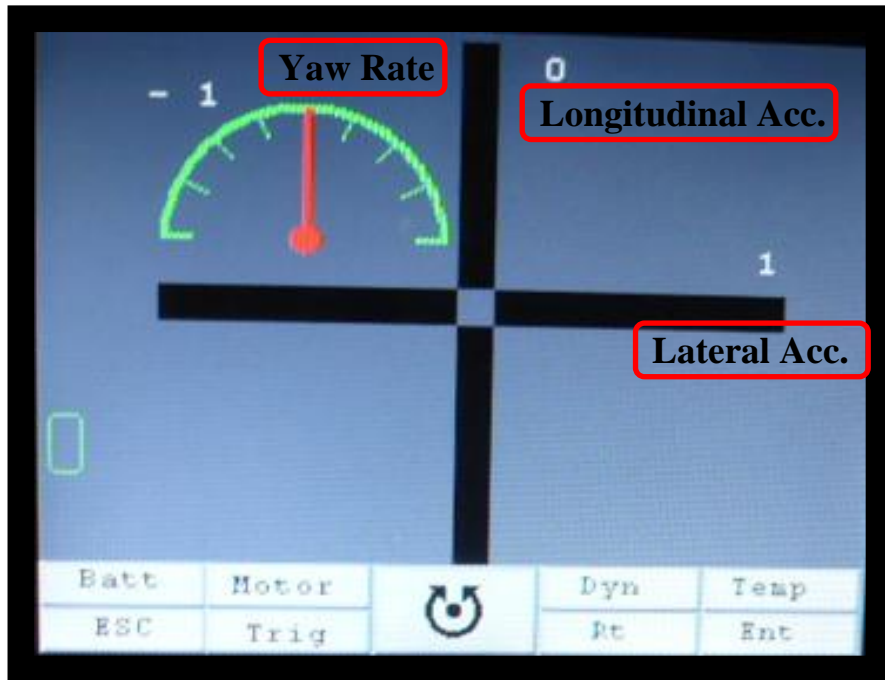


Figure 4-15: GUI dynamic screen

4.1.4 Electric Energy Storage System

The electric power to this vehicle is supplied by three batteries: one 12-volt DC battery, and two high- voltage DC batteries. The 12V battery is used to supply basic electric power to keep the vehicle computer running before engaging the high-voltage batteries. This way, any unexpected incident can be prevented in case of fault occurrence during software download on the vehicle computer. This section discusses the electrical power storage and all of its related components.

There are two high voltage (HV) batteries used to store the power. These batteries are made up of Nickel Metal Hydride (NiMH). They are capable of providing 18 kWh per charge, which is equivalent to 18km in driving distance. Although it is too short to be practically placed in production EVs, it is nonetheless sufficient for the purpose of research.

These two batteries are placed in two different locations: one is located under the hood and used for driving the front two motors, while the other sits on the chassis (rather than the rear seats) and supplies required power to the rear two motors, as shown in Figure 4-16.

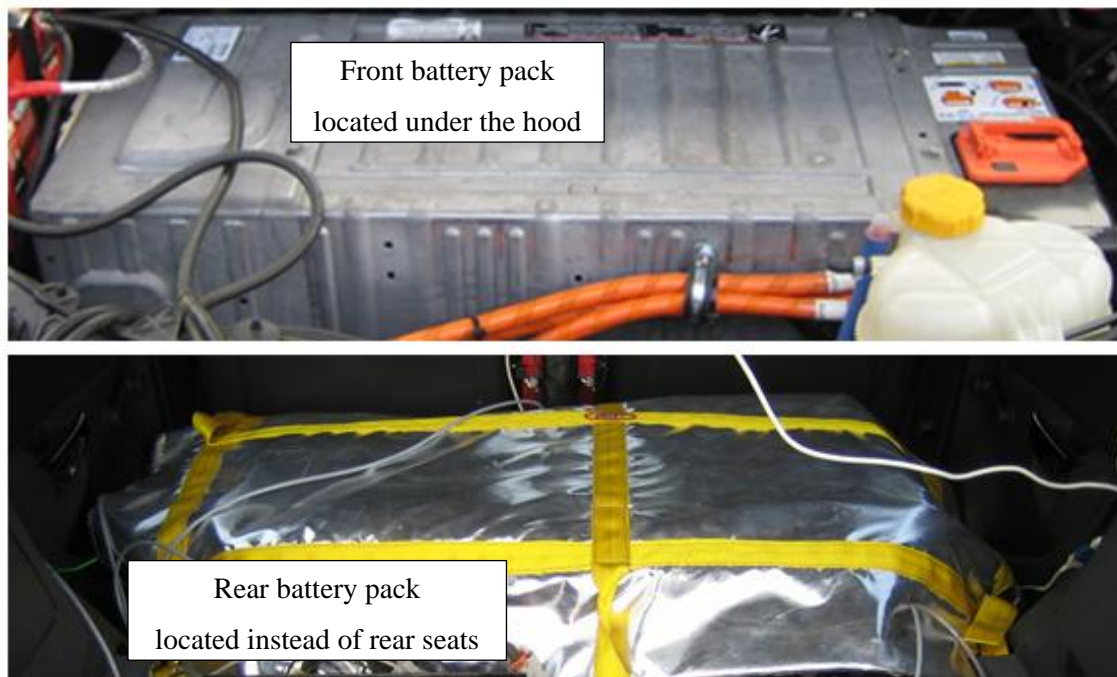


Figure 4-16: High voltage battery packs

These batteries have their own Battery Management System (BMS) monitored through the GUI. Any offset or adjustment needed for these batteries can be made by dSPACE via the on-board laptop.

The auxiliary electric power source is needed to let the user start the vehicle on-board computer and perform desired configurations without turning on the HV batteries and motors. A conventional 12 volt DC power battery is embedded under the hood, and is connected parallel to the front 300 [V] battery. For the purpose of hardware-in-the-loop and in-lab tunings, this battery is used while being charged with the charger plugged into the wall. When the car is used on the road, this 12 [V] battery is being charged from the HV battery. Since this battery is always fully charged, the driver is still able to stop the car using the friction brake system in case of power outage in the main power source (HV batteries). The friction brake system needs a 12 [V] supply to operate.



Figure 4-17: 12V battery located under the hood

Having an adequate charging system is essential in any electric vehicle. Two powerful and efficient chargers of the Manzanita Micro PFC 30M type are used to charge the two high voltage NiMH batteries. These chargers are shown in Figure 4-18, and are placed in the trunk area while being separately connected to the front and rear batteries.

They support any input voltage in the range of 100V to 240V AC power, and can be adjusted to charge batteries varied from 12 to 450 volts. The reason they are labeled “Power Factor Corrected (PFC)” is because the current and voltage are drawn in unity. The built-in cooling fan is placed

inside the charger enclosure to avoid overheating. The chargers are enabled/disabled by the dSPACE via the charger interface circuit, shown in Figure 4-19.



Figure 4-18: Manzanita Micro PFC Charger

4.1.5 Inertial Measurement Unit

This inertial and GPS navigation system, as shown in Figure 4-19, is an advanced six-axis inertial navigation system of the RT-2500 model bought from Oxford Technology Solutions Ltd. It incorporates an UrbanTrack GPS receiver [41].



Figure 4-19: OXTS 6-axis GPS IMU [42]

This device has an inertial sensor block with three servo-grade accelerometers to measure the linear accelerations along three axes (X, Y, Z), as well as three gyros to measure the angular rates about these three axes, as shown in Figure 4-20.

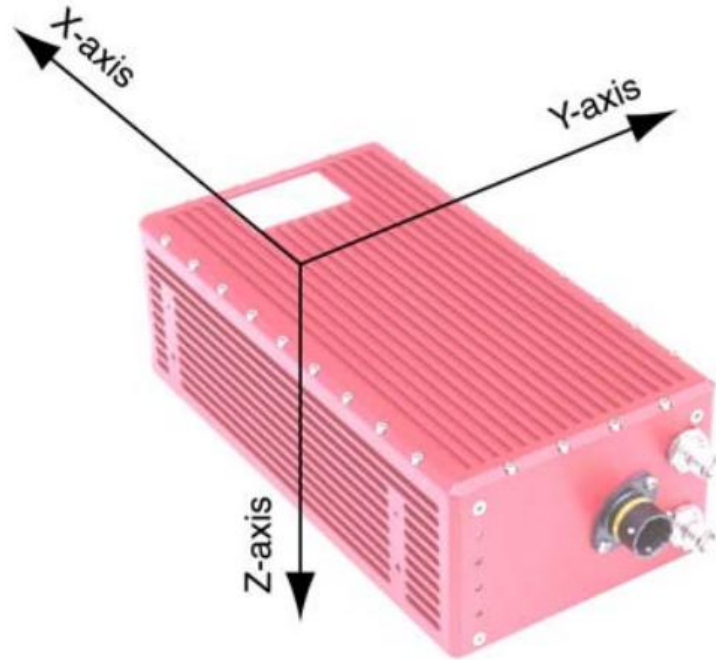


Figure 4-20: Coordinate system of the IMU

The advantages of using both inertial sensors and the GPS over using the GPS alone include higher update rates (100Hz or 250Hz), very low latency (3.5ms), and continuous outputs during GPS blackout conditions. Acceleration signals, especially the angular acceleration signal, are noisy because of the vibration produced by the vehicle. The RT unit is capable of filtering both the linear and angular accelerations before sending them out through the CAN bus, using a second order low-pass filter.

The GPS unit has its own correction system, using the three consecutive rotation matrices (Euler angles) that transform a vector measured in the navigation coordinate frame to the body coordinate frame. If V_n is vector V , measured in the navigation coordinate frame, and V_b is the same vector measured in the body coordinate frame, the two vectors are related by equation (4-1), where Ψ is heading angle, θ is pitch angle, and ϕ is roll angle [41].

$$V_n = C_{bn}V_b \tag{4-1}$$

$$C_{bn} = \begin{bmatrix} \cos \Psi & -\sin \Psi & 0 \\ \sin \Psi & \cos \Psi & 0 \\ 0 & 0 & 1 \end{bmatrix} \begin{bmatrix} \cos \theta & 0 & \sin \theta \\ 0 & 1 & 0 \\ -\sin \theta & 0 & \cos \theta \end{bmatrix} \begin{bmatrix} 1 & 0 & 0 \\ 0 & \cos \phi & -\sin \phi \\ 0 & \sin \phi & \cos \phi \end{bmatrix} \quad (4-2)$$

Figure 4-21 shows the location of this IMU installed in the vehicle, which was transferred to the actual CG point of the vehicle by using the built-in setup software. All initial setup for this unit is performed using the on-board laptop via 10/100 Base-T Ethernet port and the real-time results are output on CAN bus, accessible from the dSPACE MicroAutoBox.



Figure 4-21: Location of OXTS IMU

The performance specification for this series of IMU unit is shown in appendix B, as provided by the manufacturer [42].

4.2 Vehicle Parameters Measurements

There is a list of parameters that are required for the model to calculate the output. Some of these parameters, such as the track width or wheelbase, are relatively easy to measure. Other parameters, such as the center of gravity location and wheel moment of inertia, need more calculation and test. This section discusses the procedure of calculating these parameters.

4.2.1 Steering Wheel Gear Ratio

The steering mechanism consists of different components to provide mechanical advantages, such as the ratio of output force to the input force applied to the system. In the steering system of the vehicle, the driver's input to the hand wheel results in a much larger steering force at the front wheels. For example, applying a force of 5 pounds to the hand wheel can produce up to 130 pounds at the front wheels. This increase in force is supplied by the steering gear ratio.

In other words, the steering gear ratio is a number that should be multiplied by the wheel steering angle obtained from CAN-Bus to give an angle of each wheel on the ground during turning. The higher the steering ratio, the easier it is to steer the vehicle; however, higher steering ratios also mean that more turns of the steering hand wheel are needed to achieve the intended steering [43].

The steering gear ratio varies greatly and is dependent on the type of vehicle and its operation. Low steering ratio is usually called fast or quick steering, and is more common for passenger vehicles. There is an exception to the available test vehicle, which has a gear ratio about twice that of other sedan cars. The reason for this is the excessively large tires and rims used in the test vehicle to provide enough room for electric motors and their attached components.

To attain this angle, a simple test was performed. The steering hand wheel was turned for a number of angles, and the angles of each wheel were recorded. Next, based on the collected data, the gear ratio can be easily estimated. This ratio is equal to 32 for the wheels. Figure 4-22 shows the way that the wheel angle on the ground was read.



Figure 4-22: Setup for steering gear ratio measurement

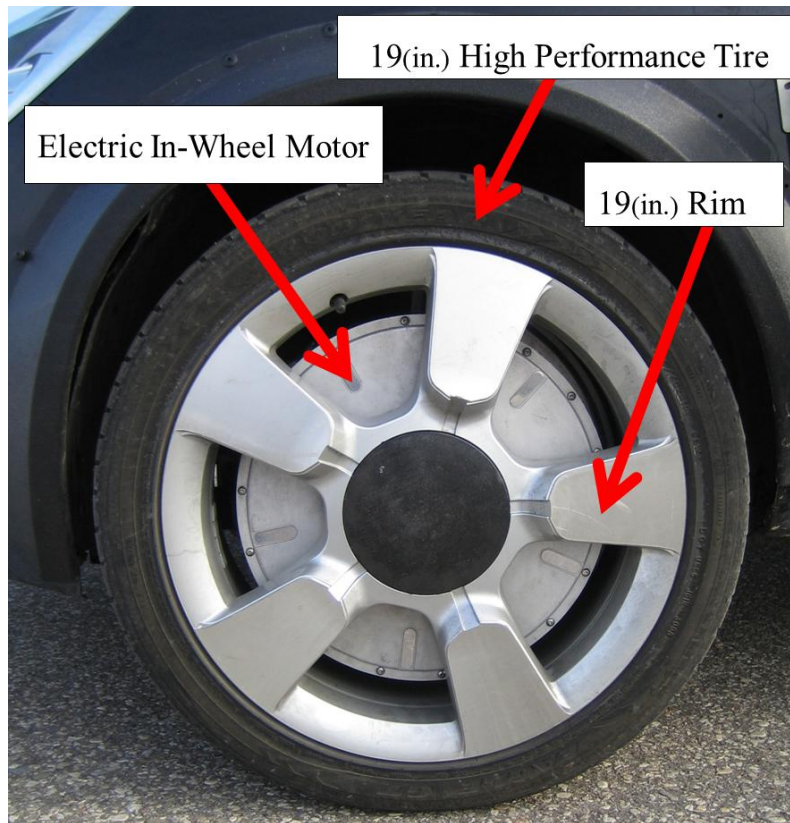


Figure 4-23: Front wheel assembly with wheel hub motor

4.2.2 Weight Measurement Procedure

Curb weight is the weight of the vehicle when it is loaded with all of its standard operational equipment and fluids. Because of the modifications performed on this vehicle, including the removal of the internal combustion engine and the addition of battery packs, the weight of the vehicle is not identical to the original model. This weight plays a key role in each of the algorithms that use the vehicle model and parameters, including the driver command interpreter, stability controller system, and vehicle estimation works.

The portable weight scale system is the suitable device to complete all force/mass measurements. These wheel load weight scales provide a convenient and versatile method of determining vehicle weight. To weigh the vehicle, portable load scales made of high strength aluminum were placed on the lab ground surface, which is made of cement. This is because the accuracy and repeatability of the wheel load is significantly affected by the scale foundation, and cement is the best foundation. These load scales are functional in the temperature range of -10°C to $+40^{\circ}\text{C}$ with 0.1% accuracy.



Figure 4-24: Vehicle sitting on the load scales

The measurements have been completed twice; initially, the car was empty, and then it was completed with two passengers sitting in the front seats. For stability control purposes, the weight measurement with two passengers was used, since the driver and the extra person is needed in the car for the road test. The measured weights for both measurements are listed in Table 2 [44, 45, 46, 47].

Table 2: Vehicle load/mass measured data

Descriptions		Load Without Passengers	Load With 2 Passengers
		[lb] ([kg])	[lb] ([kg])
Wheel Orders	Front Left	872 (395.5)	961 (436.0)
	Front Right	871 (395.0)	969 (439.5)
	Rear Left	699 (317.0)	784 (355.6)
	Rear Right	650 (294.5)	746 (338.4)
Vehicle Total Load		3090 (1402.0)	3460 (1569.5)

4.2.3 Center of Gravity (CG) Location

One of the essential parameters for the proposed model is the location of CG, which can be calculated in the horizontal plane and from the weight measurements of each corner. This static information can give us the CG location using the equations (4-3) to (4-6).

$$L_f = \frac{F_{zrl} + F_{zrr}}{m g} L \quad (4-3)$$

$$L_r = L - L_f \quad (4-4)$$

$$L_{srl} = L_{sfl} = \frac{(F_{zfl} + F_{zrl})}{m g} e_f \quad (4-5)$$

$$L_{srr} = L_{sfr} = t_r - L_{sfl} \quad (4-6)$$

L_f and L_r are the distances from the CG location to the front and rear axles, respectively. Parameter L is the vehicle wheelbase, and F_{zrl} and F_{zrr} are the acting vertical forces on the rear left and rear right wheels, individually. The track width of the vehicle at the front and rear are assumed to be the same, and equal to t_r . Parameters L_{sfl} , L_{sfr} , L_{srl} , L_{srr} are the distance between the CG location and the four corners of the vehicle.

After finding the horizontal coordinates of the CG point, the height needs to be calculated. This is possible by locating the vehicle on the inclined surface. Applied load on the front and rear axle in addition to the surface angle make it possible to get the height CG (H_{CG}) using equation (4-7), where γ is the surface angle.

$$H_{CG} = \frac{1}{m g \sin(\gamma)} ((F_{zrl} + F_{zrr})L - m g L_f \cos(\gamma)) \quad (4-7)$$

4.3 Hardware-in-the-loop setup

The framework of the hardware-in-the-loop setup is shown in Figure 4-25. In this figure, the connection between hardware and vehicle dynamic software is illustrated.

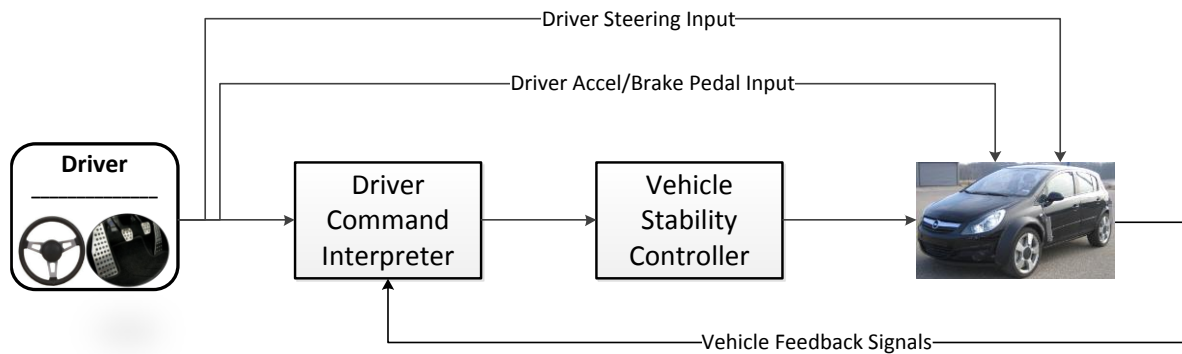


Figure 4-25: Hardware-in-the-loop simulation framework

The reason for performing the hardware-in-the-loop test was to make sure that all developed algorithms, based on theories and conversions from Matlab codes to Simulink blocks, would be compiled appropriately for the vehicle on-board computer. Additionally, conducting this test is also necessary to ensure that these algorithms communicate properly with other hardware and sensors such as gas/brake pedals and the steering column sensor.

As shown in Figure 4-25, driver inputs are sent to the vehicle overall control unit, which is the dSPACE AutoBox. Next, the required traction/braking torques are determined and sent to the computer connected to AutoBox, which has a CarSim program installed and running. The exact vehicle model created in the CarSim provides CG accelerations of the vehicle instead of the actual IMU. These accelerations were used to calculate the CG forces, and were then compared with the desired forces generated from the DCI. Using this step, the performance of the stability controller was tested to make sure it was not producing large unexpected torques; this was necessary after any modification to the vehicle controller.

Figure 4-26 and Figure 4-27 show the vehicle in the lab, while the HIL test was performed. Although the final input torques to all four wheels was blocked, and the circuit between batteries and motors was open, the vehicle was lifted off the ground in case of any unexpected human error. The computer loaded with the required programs was then connected to the car through the designated interface panel and PCI card. This computer was replaced with a laptop for the road test.



Figure 4-26: Vehicle off the ground in the lab for HIL test



Figure 4-27: HIL Computer connected to the vehicle in the lab

4.4 Implementation Issues and Solutions

Before compiling the controller codes onto the on-board vehicle microprocessor, some modifications and tunings were performed to solve real-time implementation issues.

4.4.1 Sample-Time Issue

The first issue at the implementation stage was related to differences in the sample times of the DCI and the sensors. During the computer simulation, all subsystems such as DCI and CarSim had sample times of 0.001 seconds, but the sample time for the real sensors mounted on the vehicle were 0.005 second. It was noted that different sample times cause the input to the DCI to not be updated properly. This issue was resolved by internally predicting the data for the missing sample-times.

As shown in Figure 4-28, sensory data are fed to the DCI at time t , while the calculated desired forces are produced at time $t + n\Delta t$, where Δt is the sampling time of the DCI and n is the number of missing sample times. Thus, the DCI requires updating its parameters in this timespan by running the built-in vehicle dynamics model. As mentioned before, the sample time considered for the developed DCI is 1 millisecond, while the minimum sample time for the sensors and hardware communications can be set to 5 milliseconds. It is concluded that the value of n is equal to 5.

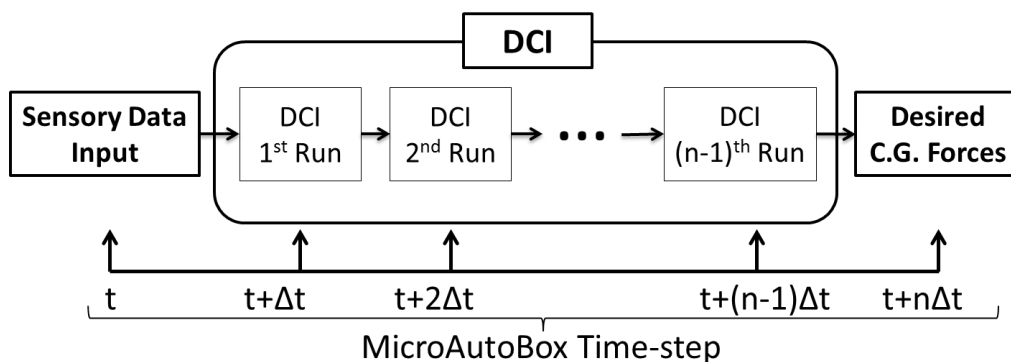


Figure 4-28: DCI internal prediction

4.4.2 Noise Issue

Noises in the outputs of the steering column sensor and wheels' optical sensors were the second issue in the implementation stage. This stage focused on the inputs to the DCI, and thus created the noisy calculated signals. In addition, the low-frequency noises were observed in the vehicle's IMU

outputs, causing large discrepancies in the CG forces. Different filters have been offered in research literature to fix noise issues. For the purpose of this thesis, these noises were removed by applying 4th-order Chebyshev type II filters to the signals of both the DCI and the IMU.

The fast response time and more reliable real-time performance of this filter made it a seamless candidate for this application, especially when compared to other low-pass filters. As shown in Figure 4-29, this Chebyshev low-pass filter is free of ripple in the passband region, while there might be ripples in the stopband region. The gain of this filter is calculated using equation:

$$G_n = \frac{\epsilon}{\sqrt{1+\epsilon^2}} \quad (4-8)$$

where the ripple factor (ϵ) is equal to:

$$\epsilon = \frac{1}{\sqrt{10^{0.1\gamma_{filter}-1}}} \quad (4-9)$$

The cutoff frequency (F_h) of the filter is determined by the -3 dB point of the filter magnitude response relative to the peak passband value, and the stopband edge frequency (F_c) is related to (F_h) by:

$$F_c = F_h \cosh\left(\frac{1}{n} \cos^{-1} \frac{1}{\epsilon}\right) \quad (4-10)$$

This filter has steeper transition-region roll-off, but more nonlinear-phase response characteristics.

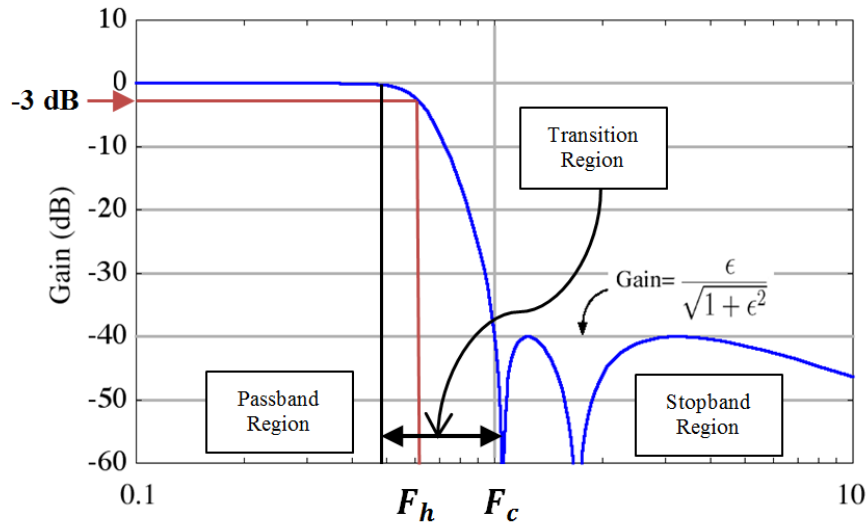


Figure 4-29: Chebyshev type II filter bode diagram

The custom-designed filters used in the experimentation have a stopband ripple magnitude (γ_{filter}) of 60 dB, while the cutoff frequencies were set to 5 Hz. Although the system was affected by delay due to filter integration, the amount of delay is sufficiently small enough to not deteriorate the controller's stability and accuracy.

An alternative solution was also found: by using the 30-point average smoothing filter, the low magnitude-high frequency noises could be by-passed, resulting in a clean signal being obtained.

4.4.3 Acceleration Generation from IMU Outputs

Cost is one of the important metrics for the automotive industry. In most road tests, the highly accurate 6-axis IMU have been used to get the actual CG linear and rotational accelerations, but such an IMU is too expensive to be used in all low-class vehicles. On the other hand, the regular 3-axis IMU installed on most vehicles does not generate the necessary rotational acceleration, and only measures the yaw-rate.

To solve this problem, a 5th-order differentiator was used to resolve this issue. To obtain the yaw acceleration, the last five data points plus the current yaw-rate values are needed. The formulation of the differentiator is:

$$\dot{r} = \frac{16U_0 + U_1 + 10U_2 - 10U_3 - 6U_4 + 9U_5}{28\Delta dt} \quad (4-11)$$

where:

$$U_i = r(t - i) \quad i = 0, 1, \dots, 5 \quad (4-12)$$

This differentiator also caused some delay in the system, but not significant enough to affect stability controller performance [4].

Chapter 5

Full Vehicle Testing

This chapter discusses the available test track, the road surface condition, and the standard driving scenarios performed for the purpose of algorithm verification using the available EV. The results for these tests are presented at end of the chapter.

5.1 Standard Tests Description

5.1.1 Test Track

Waterloo Region Emergency Services Training and Research Complex (WRESTRC) was used for high speed testing is normally used for training purposes for vehicle drivers of emergency vehicles such as fire trucks and ambulances. This track had a length of 250 [m] and a width of 40 [m], as shown in Figure 5-1.

The rectangular area marked in the middle of this field has a different ground surface. This surface was used as the low μ surface because the vehicle became more easily unstable on this surface compared to other areas of the field. Pouring water on top of this surface made it more slippery and comparable with icy roads. After validating the driver command interpreter and vehicle stability controller on the high μ surface, the car was driven on this specific surface to see the performance of the controller in unstable conditions.

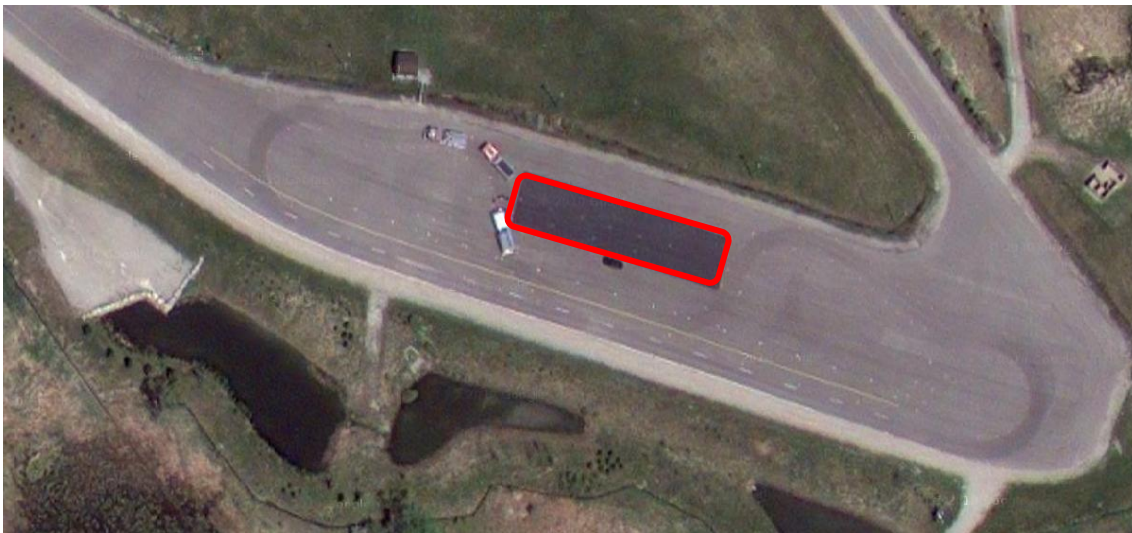


Figure 5-1: Test Track (Google Map)

5.1.2 Environmental Conditions

Different testing was completed in different environmental conditions. Some results were obtained in the summer time, while others were obtained during colder weather conditions in the fall. The change in temperature has an effect on the tire performance and overall vehicle action.

Since vehicle was not isolated properly, no testing was performed during the winter time or whenever the test track was filled with snow or ice. The solution to create a slippery road for evaluating the DCI and testing the vehicle controller was to put sand on the ground and evenly distribute it to make sure all four wheels are sensing the same road condition.

5.1.3 Test Scenarios

The objective of these tests were to determine handling and stability characteristics of the passenger vehicle with independent electric-driven motors through two different standard tests. These tests were chosen based on the limitations from both the vehicle and the test track. In all the tests, the vehicle was stopped in the beginning, but presented results were not saved from a stationary condition. This was because the limitation from the on-board laptop memory resulted in a boundary for the recording time.

5.1.3.1 Double Lane Change (DLC) Test

This safety test consisted of performing an obstacle avoidance maneuver to evaluate the handling and stability characteristics of the vehicle under extreme conditions. The car was driven through a double-lane-change course at increasing speeds until the test was determined to be unsafe. The test was defined unsafe if the vehicle handling became unstable, or if any of the tires lost contact with the surface.

The vehicle entered the test course in the right lane, crossed over to the left lane within the 13 [m] gate spacing, traveled for another 11 [m], and then returned to the first lane in the next 12 [m] spacing. The layout of the test track for this standard scenario is illustrated in Figure 5-2, while Figure 5-3 shows the vehicle trajectory recorded by the GPS.

For the purpose of validating a driver command interpreter, a test run is only considered valid if the vehicle is able to perform the maneuver at a constant speed without deviating from the test course or striking pylons. Any instability in the vehicle means that the car is not following the driver's desired commands. After validation, the proposed stability controller was enabled, and the

vehicle speed was increased up to the point that the vehicle was stable with the controller, but unstable without it. In this way, the robustness of the DCI and the vehicle controller was proved together.



Figure 5-2: Test track with cones setup for double-lane-change scenario



Figure 5-3: Top view of the test track with pylons in place for a double-lane-change maneuver (Google Map)

At the DCI verification stage, the vehicle did not take to its stability limits; however, to check the controller performance, the test driver was unaware of the controller enable/disable condition. This way, the possibility of any additional effort from the driver to keep the car stable could be reduced [48].

5.1.3.2 Slalom Test

The purpose of completing a slalom run was to determine how realistically the DCI model predicts while driving at moderate turning and velocities. Figure 5-4 shows a layout of slalom setup on the available track. Pylons were arranged in a straight line about 20 [m] apart over a total distance of 100 [m]. A positive point about the slalom test is that the vehicle experiences different lateral acceleration and rotational moments at its CG point, which is helpful in evaluating the DCI and controller robustness.

The vehicle average speed during this standard scenario was 43 [km/h], while the driver steering input was changing from -300 [deg] to 350 [deg] on the hand wheel, with consideration that the steering gear ratio in this vehicle was 32. This means wheel angle variations of -9.5 to 11 [deg] on the ground.

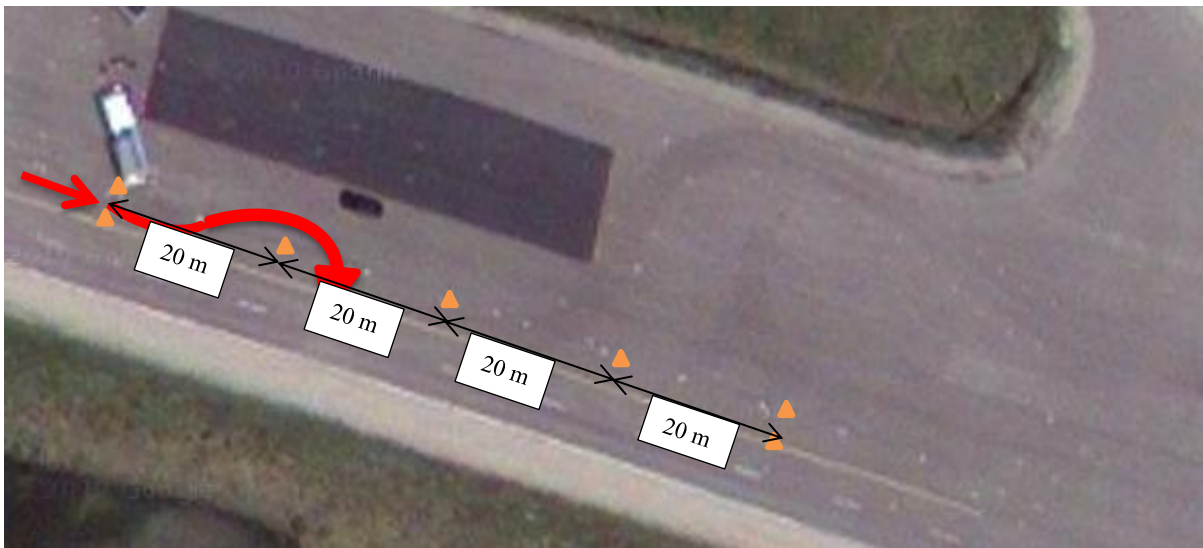


Figure 5-4: Semi-Slalom Test (Google Map)

5.1.4 Test Driver

This car was not tested and verified by the research team before any implementation, and the friction brake module was added by our team, which did not have the same braking power as regular vehicles. As such, the stopping distance of the test vehicle was twice as much as the standard distance achieved with the original OEM brakes. Due to these limitations and its inherent dangers, amateur non-experienced drivers were not permitted to test drive this car, and a professional driver was required for testing purposes.

The designated male driver to perform all validation testing was 24 years old, and has participated in specific high speed driving training classes. The test results shown in this work were obtained while he was driver. However, after finishing this validation stage and learning the vehicle's actions, four different drivers with different driving experiences were employed to verify the performance of the stability controller.

5.2 Results and Analysis

The results for the two previously mentioned scenarios are presented and discussed in this section. To verify the sensors and the vehicle computer, the test vehicle was driven in a small parking lot before these high speed tests were conducted.

Based on the rough data collected during these runs, basic sensitivity analysis had been performed to determine the effectiveness of all 23 independent parameters in the DCI model, including both vehicle and tire parameters. The figure shown in appendix G presents the results of this analysis, as obtained by ADAMS/Insight software [49].

5.2.1 Double Lane Change (DLC) Test Results

As illustrated in Figure 5-5, the input torques to both the front and rear wheels, which were adjusted to be identical. This is also known as the 50/50 front-to-back torque ratio. At the beginning of the test, the gas pedal was fully applied to accelerate the car from a stationary position and increase the speed to 55 [km/h]. The rest of the torque applied to each wheel from the 3rd second up to the end of the DLC maneuver (9th second) was about 150 [N] for maintaining the speed constant.

Looking at Figure 5-7, it is obvious that driving with constant speed and doing two immediate lane changes was not easy for untrained drivers on the research team. Figure 5-6 also shows the input steering angles, which was applied to the hand-wheel by the driver. By dividing these angles by the steering gear ratio, the wheel angles on the ground roughly varied from -5 [deg] to -6 [deg]. The negative torque applied after the 9th second was the limited braking torque assisting the friction drums to stop the car before reaching to the end of track.

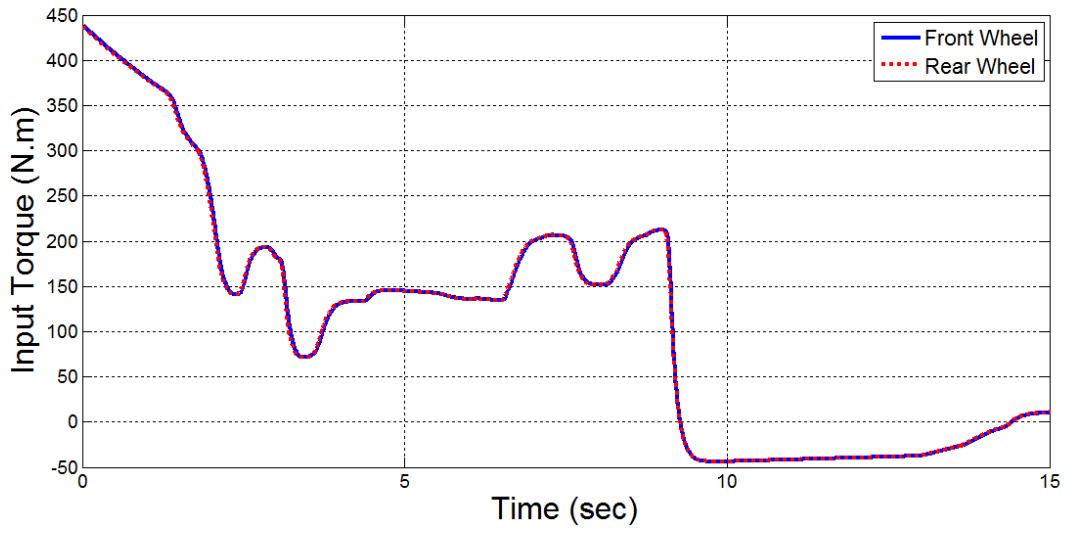


Figure 5-5: DLC test input torques

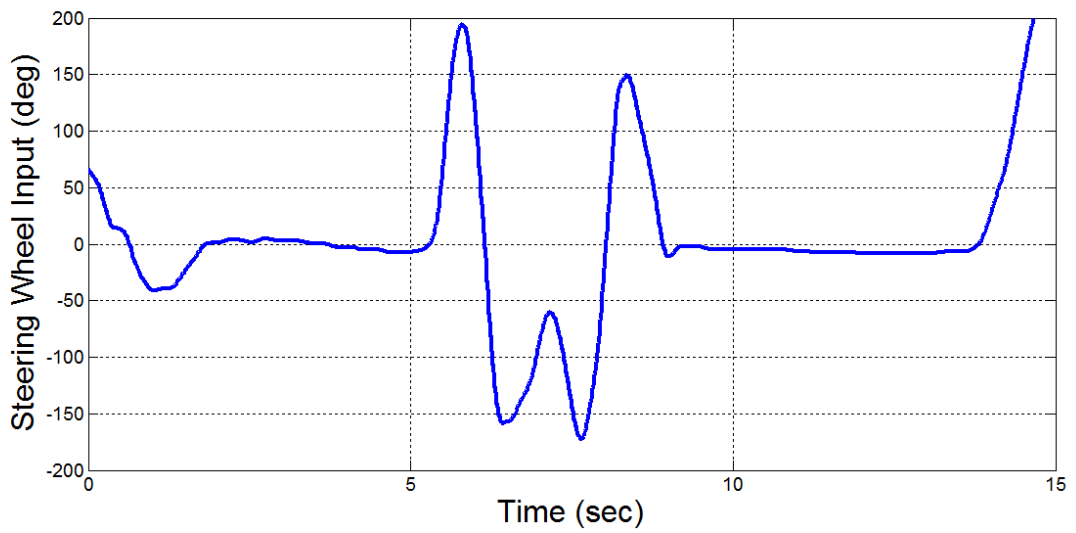


Figure 5-6: DLC test input steering angle

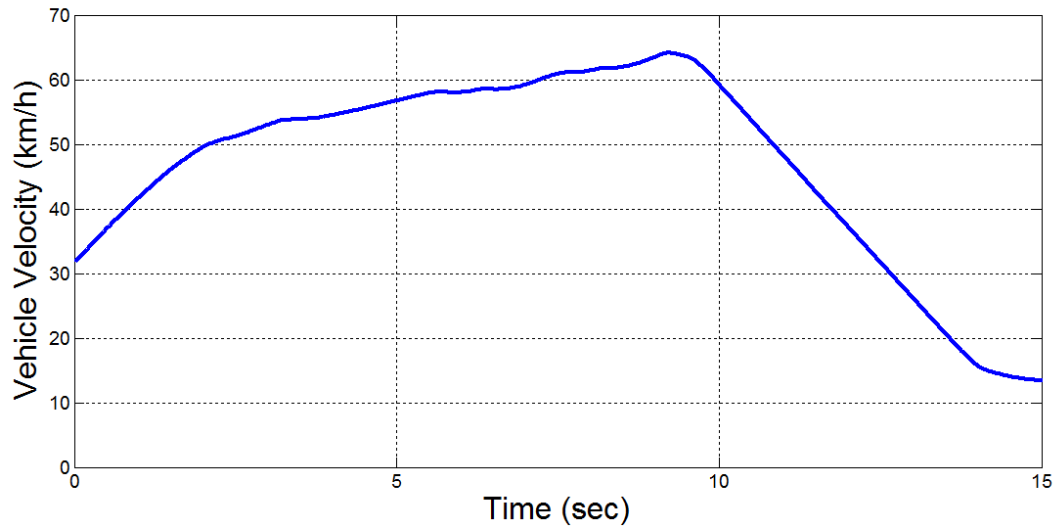


Figure 5-7: DLC test vehicle forward velocity

Figure 5-8 to Figure 5-10 show the results of the forces measured and calculated at the CG location. These figures present the general obedience of the DCI with the vehicle body. Some discrepancies that occurred in the longitudinal forces could be caused from the assumed and original drag forces. In the DCI, the drag force was modeled to be linear proportional to the vehicle speed, while the actual drag force has a more complicated concept.

Small deviations observed in the lateral forces and yaw moments were due to the side-slips experienced during the maneuver. These plots were matched to each other as soon as the vehicle body settled to its normal conditions. Figure 5-11 shows the trajectory of the test vehicle passing through the DLC course, as captured by the GPS unit. The red circle shows the section of the course where the vehicle went through two lane changes.

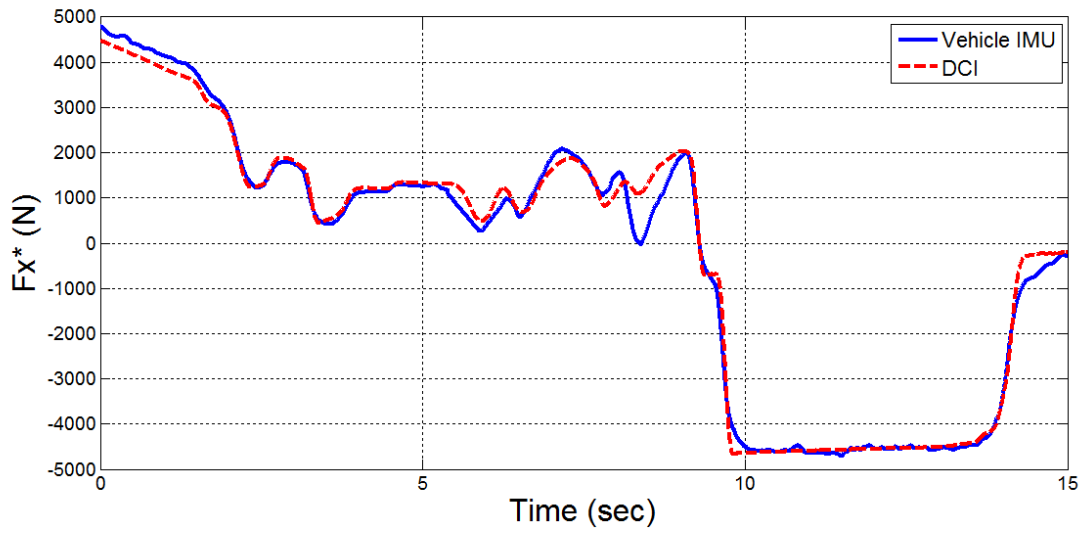


Figure 5-8: DLC test forward force at CG point

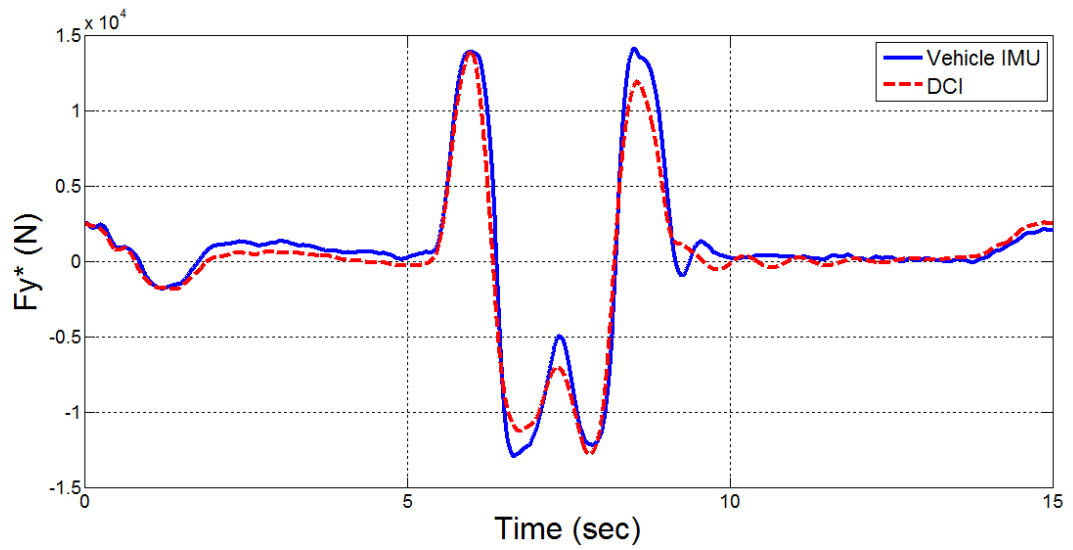


Figure 5-9: DLC test lateral force at CG point

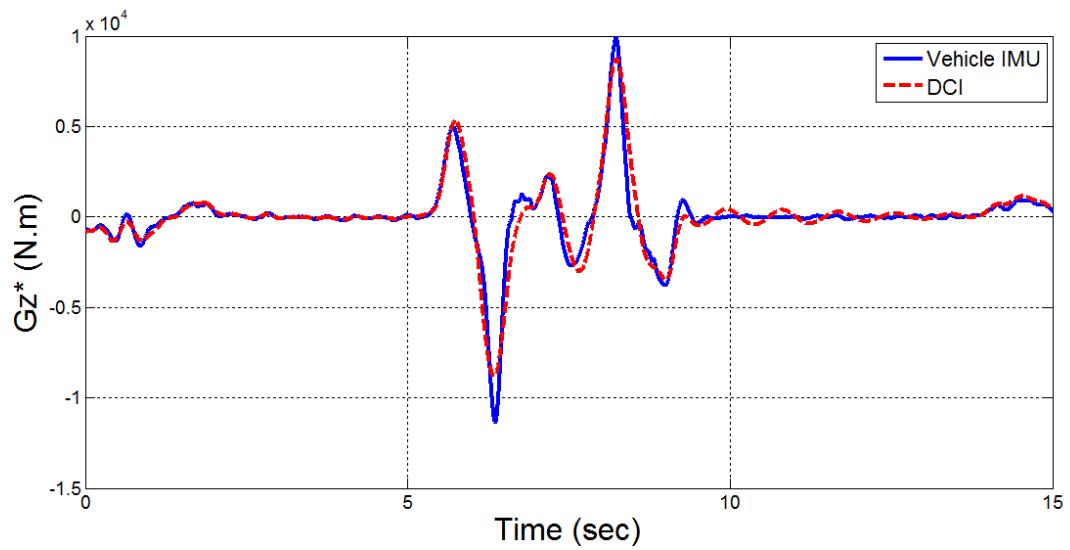


Figure 5-10: DLC test yaw moment at CG point

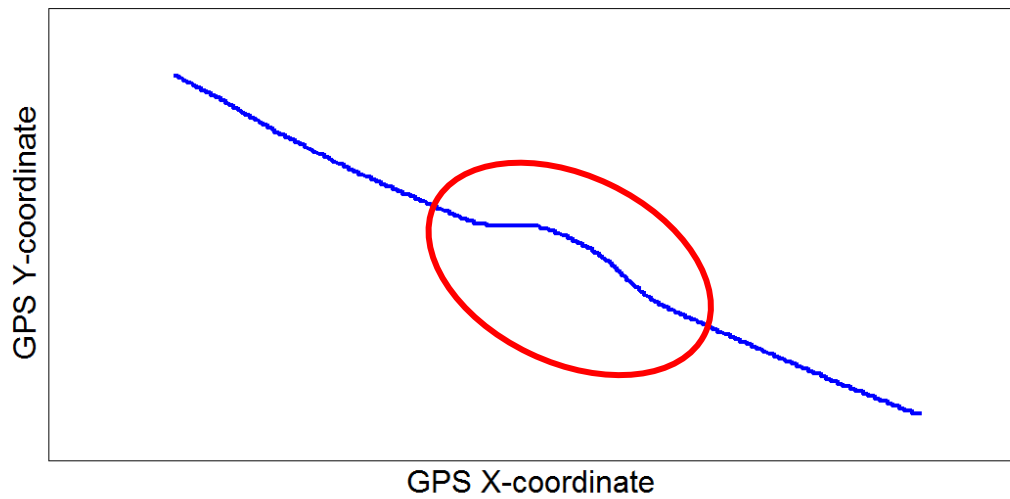


Figure 5-11: DLC test vehicle trajectory

5.2.2 Slalom Test Results

The second test used to investigate DCI performance was the slalom test. Results of this test are presented below. Figure 5-12 and Figure 5-13 depict the motor torque and desired steering angle commanded by the driver.

Similarly to the DLC, the vehicle was accelerated from stationary to 43 [km/h] using the full power of the electric motors, and subsequently operated at a constant speed. The driver's effort on the hand-wheel had to be increased after moving to the next pylon, which originates from the vehicle body's natural oscillations. In other words, vehicle tires were reaching their saturation point, and high slipping condition were occurring.

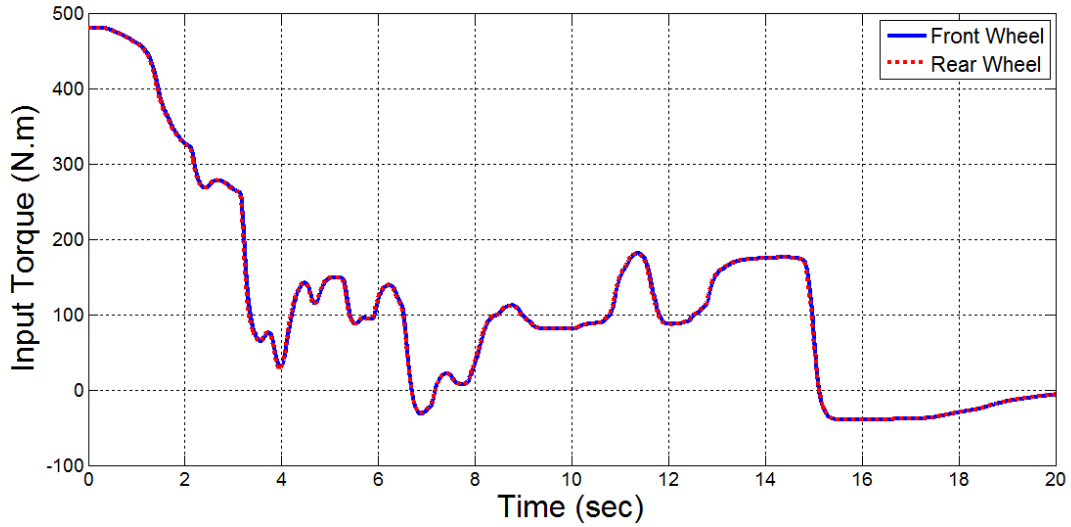


Figure 5-12: Slalom test input torques

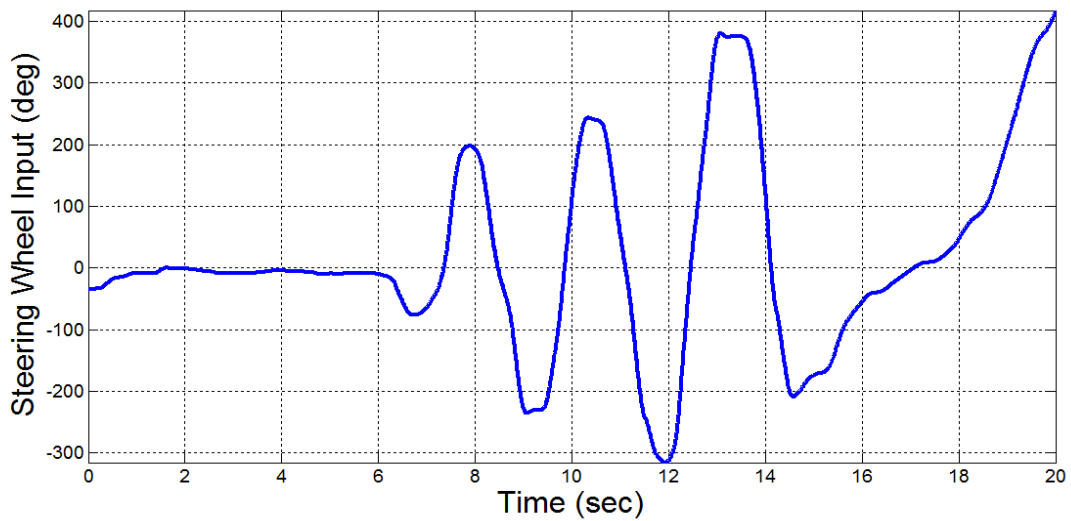


Figure 5-13: Slalom test input steering angle

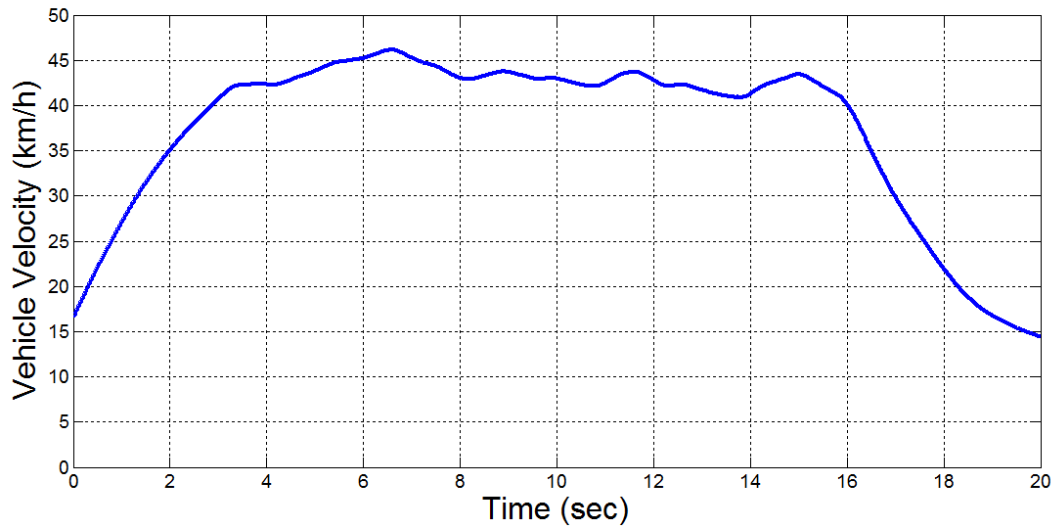


Figure 5-14: Slalom test vehicle forward velocity

As illustrated in Figure 5-15 to Figure 5-17, it is shown that in addition to yaw moments, desired longitudinal and lateral CG forces are following the measured forces. Some gaps between the longitudinal force plots were determined as a result of different drag force modeling. Small changes were noticed in the actual yaw moment plot, which was not generated by the DCI. The IMU was installed on the vehicle chassis, which means it attained any minor forces applied to the vehicle body. Such a force could not be regenerated in the proposed DCI model, which concludes the reason for these disagreements.

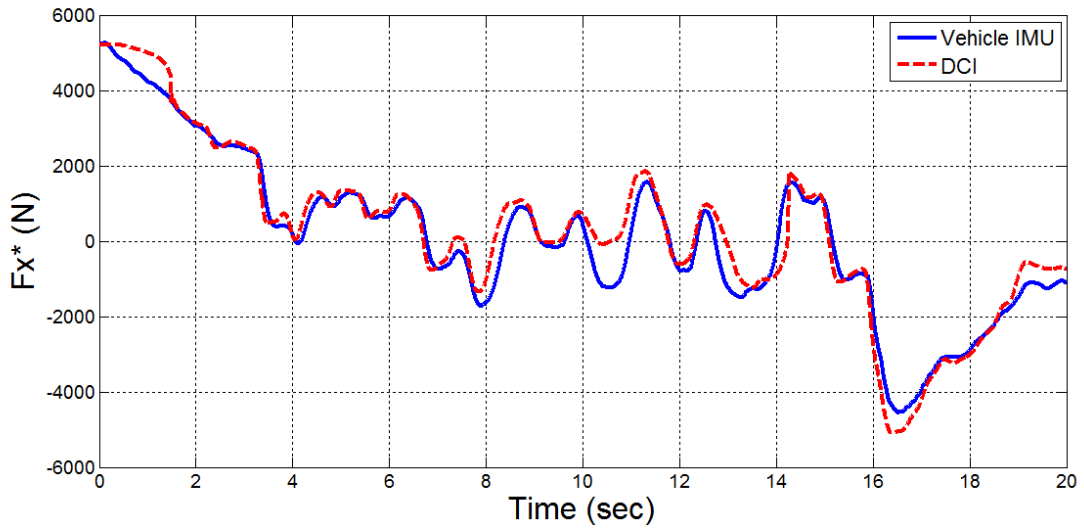


Figure 5-15: Slalom test forward force at CG point

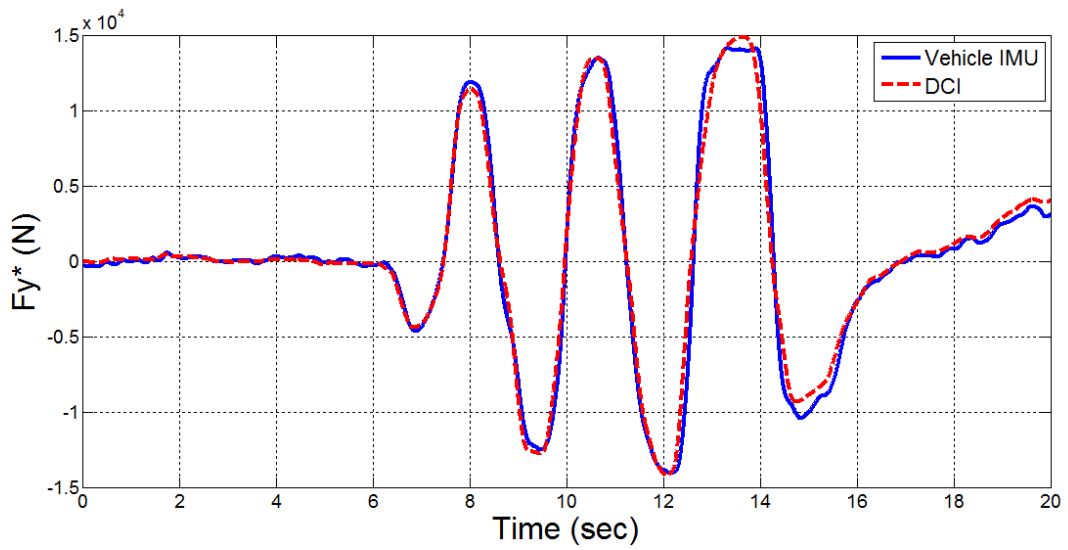


Figure 5-16: Slalom test lateral force at CG point

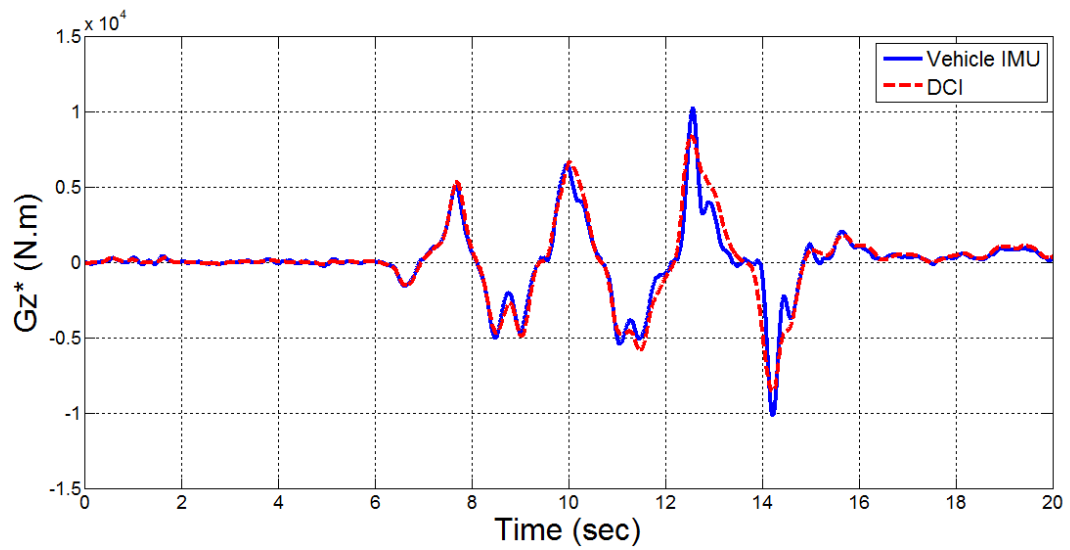


Figure 5-17: Slalom test yaw moment at CG point

Figure 5-18 shows the GPS-based vehicle trajectory during the slalom test. The red circle defines the section of the court where the pylons were located.

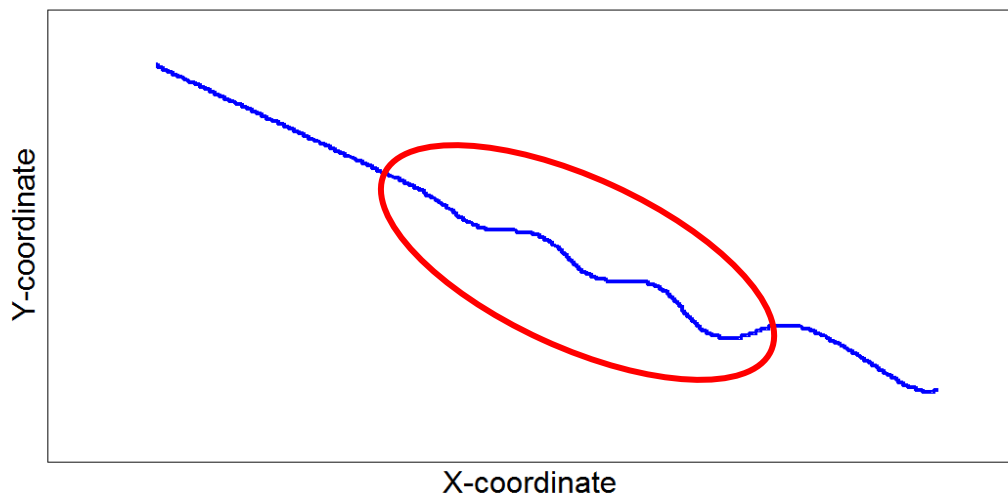


Figure 5-18: Slalom test vehicle trajectory

Chapter 6

Conclusion and Recommendations

6.1 Conclusion and Summary

In this thesis, a Driver Command Interpreter (DCI) module was successfully developed in order to interpret the driver's intention and to generate proper control actions using an accurate bicycle vehicle model. The accuracy of the DCI module was verified through experiments, as shown by the presented results obtained from both computer simulations and full vehicle testing on the road.

First, a mathematical model for the DCI was developed and analyzed. The model was then implemented in Matlab/Simulink format for validation via computer simulation. All of the required vehicle-body feedbacks input to the DCI module (e.g., velocity, actual accelerations) were provided using the CarSim software, which has a large library of full models for different vehicles. The uniqueness of this work was in performing the HIL and real-time road test to evaluate real-world functionality of the DCI after obtaining positive results from the simulation. The purpose of the HIL was to detect the potential issues involved in the software and hardware interaction, and to find solutions to these problems. The final implementation of the DCI code was compiled into C-code and installed on the vehicle's on-board computer.

Full vehicle testing was achieved by deploying a fully electric Opel Corsa equipped with various sensors and hardware. Four electric DC motors and their drivers were connected to the wheels without a gear or drive shaft, also known as the in-wheel hub. The ability to control the torque of each wheel independently – which facilitates in achieving vehicle stability – was attained in this EV. The process of becoming familiar with the EV, and making hardware diagnostics and modifications (which took a relatively long time) was also part of this research effort.

Testing was performed in a restricted open area that was only accessible to the research team. Two standard driving maneuvers were performed by an experienced driver with professional driving certificates. These driving scenarios were extracted from available vehicle stability tests. Automakers usually evaluate the performance of developed components based on the ranking obtained by tests such as these.

A fully practical DCI was defined as a module to connect the driver inputs to the vehicle dynamics stability controller. The DCI's role is to provide the desired forces of the vehicle at the

CG location based on driver commands such as steering input and gas and brake-pedal input. The stability controller compares these desired forces with the actual body forces that were obtained from the vehicle's IMU. The differences between these two signal series' had to be fixed by adding or subtracting the torques calculated independently in each wheel.

Full vehicle testing was performed on dry road because the DCI's role is to interpret the driver's intentions under perfect conditions. Overall, the results demonstrated good accuracy between the signals generated from the DCI and the vehicle's IMU. Some insignificant discrepancies were caused by differences between the modeled and actual resistive forces, as well as other factors that can be ignored to simplify the calculation procedure and timing. The developed DCI can be easily modified for different types of vehicle models by changing the vehicle's fixed parameters, including its mass and CG location, as well as the tire-model properties.

6.2 Future Work

For future research, it would be beneficial to study the delay in the different hardware components. The inherent assumption is that the actuation dynamics are faster than the vehicle's dynamics, which may not always be correct. Each electric motor comes with a particular motor driver that manages the performance of the motor. For example, to extend the life of the motor and avoid any serious damage, some constraints are usually imposed by the driver. These constraints and other motor characteristics should be also defined for the DCI module, thus improving its accuracy in predicting the motor's response and performance.

Further testing scenarios need to be conducted to make sure the DCI module always generates reasonable results, even in high-oscillation conditions. A driver's input when he/she is in panic might affect the performance of the DCI; this should also be investigated. This type of investigation can be conducted after making the test vehicle waterproof and driving it on low- μ condition surfaces, such as a road covered with water or ice.

Bibliography

- [1] C. B. Rogers, *High Efficiency & High Performance converter/inverter System Configurations for HEV/EV Traction Drives*, Michigan: Michigan State University, 2012.
- [2] "New World Encyclopedia," 05 May 2009. [Online]. Available: http://www.newworldencyclopedia.org/entry/Internal_combustion_engine.
- [3] [Online]. Available: http://www.bls.gov/green/electric_vehicles/#differences. [Accessed Oct 2012].
- [4] A. Athari, S. Fallah, B. Li, A. Khajepour, S. K. Chen and B. Litkouhi, "Optimal Torque Control for an Electric-Drive Vehicle with In-Wheel Motors: Implementation and Experiments," *SAE International Journal of Commercial Vehicles*, vol. 6, no. 1, 2013.
- [5] L. L. Wang, *Modeling and Simulation of the Control Strategy of Propulsion System of the in-Wheel Motors EV*, Wuhan University of Technology (People's Republic of China), 2007.
- [6] "Vehicle Suspension System," [Online]. Available: <http://www.herfehTimn2.blogfa.com/post/7>.
- [7] W. R. Garrot and E. N. Mazzae, "An Overview of the National Highway Traffic," in *SAE International Congress and Exposition*, Detroit, 1999.
- [8] "Vehicle Anti-Lock Braking System," [Online]. Available: <http://car2010.persianblog.ir/page/7>.
- [9] "Veloster & Safety," Hyundai Australia, [Online]. Available: <http://mantello.hyundai.com.au/Vehicles/Veloster/Performance-Safety/Performance-Safety>. [Accessed Feb 2013].
- [10] "Civilica," 2011. [Online]. Available: http://www.civilica.com/Paper-ISME19-ISME19_625.html.
- [11] D. Piyabongkarn, R. Rajamani, J. Y. Lew and H. Yu, "On the Use of Torque-Biasing Devices for Vehicle Stability Control," in *ACC*, 2006.
- [12] D. Piyabongkarn, J. Y. Lew, R. Rajamani, J. A. Grogg and Q. Yuan, "On the Use of Torque-Biasing Systems for Electronic Stability Control: Limitations and Possibilities," *IEEE Transactions on Control Systems Technology*, vol. 15, no. 3, pp. 581-589.
- [13] R. Rajamani, *Vehicle Dynamics and Control*, New York: Springer-Verlag, 2005.
- [14] W. Chu, Y. Luo, Y. Dai and K. Li, "Traction system coordinated allocation control for four wheel," in *The 11th International Symposium on Advanced Vehicle Control*, Seoul, 2012.

- [15] T. Chung and K. Yi, "Side Slip Angle Based Control Threshold of Vehicle Stability Control System," *Mechanical Science and Technology*, vol. 19, no. 4, pp. 985-992.
- [16] K. Popp and W. Schiehlen, *Ground Vehicle Dynamics*, Springer, 2010.
- [17] B. A. Guvenc, L. Guvenc and S. Karaman, "Robust Yaw Stability Controller Design and Hardware-in-the-Loop Testing for a Road Vehicle," *IEEE Transactions on Vehicular Technology*, vol. 58, no. 2, pp. 555-571, 2009.
- [18] M. Canale, L. Fagiano and A. Ferrara, "Comparing Internal Model Control and Sliding-Mode Approaches for Vehicle Yaw Control," *IEEE Transactions on Intelligent Transportation Systems*, vol. 10, no. 1, pp. 31-41, 2009.
- [19] H. Fujimoto, A. Tsumasaka and T. Noguchi, "Direct yaw-moment control of electric vehicle based on cornering stiffness estimation," *31st Annual Conference of IEEE*, p. 6, 2005.
- [20] C. Geng, L. Mostefai and M. Denai, "Direct Yaw-Moment Control of an in-Wheel-Motored Electric Vehicle Based on Body Slip Angle Fuzzy Observer," *IEEE Transactions on Industrial Electronics*, vol. 56, no. 5, pp. 1411-1419, 2009.
- [21] S. Takano, M. Nagai and T. Taniguchi, "Study on a Vehicle Dynamics Model for Improving Roll Stability," *JSAE Review*, vol. 24, no. 2, pp. 149-156, 2003.
- [22] H. B. Pacejka, "Tire and Vehicle Dynamics," in *SAE International*, Detroit, 2002.
- [23] J. Ahmadi, A. K. Sedigh and M. Kabganian, "Adaptive Vehicle Lateral-Plane Motion Control using Optimal Tire Friction Forces with Saturation Limits Consideration," *IEEE Transactions on Vehicular Technology*, vol. 58, no. 8, pp. 4098-4107, 2009.
- [24] A. Rezaeian, R. Zarringalam, M. S. Fallah, W. Melek, A. Khajepour, S. K. Chen and B. Litkouhi, "Joint Unscented Kalman Filter for Combined Estimation of Vehicle States and Parameters," in *11th International Symposium on Advanced Vehicle Control (AVEC'04)*, Seoul, 2012.
- [25] F. Ying, G. Yiming and Z. Hongni, "Control for vehicle handling stability based on ADAMS and Matlab," in *International Conference on Computer Application and System Modeling (ICCASM)*, 2010.
- [26] "Images of cars to paint cars coloring drawings," [Online]. Available: <http://reidosanime.blogspot.ca/2008/07/imagens-de-carros-para-pintar-desenhos.html>.
- [27] *Vehicle Dynamics Testing in Advanced Driving Simulators Using a Single Track Model*, Linköping University, 2012.

- [28] N. W. Frey, "Development of a rigid ring tire model and comparison among various tire models for ride comfort simulations," Clemson University, Ann Arbor, 2009.
- [29] J. P. Maurice and H. B. Pacejka, "Relaxation Length Behaviour of Tyres," *International Journal of Vehicle System Dynamics*, vol. 27, pp. 339-342, 1997.
- [30] J. Coffey, "Universe Today," What Is Air Resistance, 10 Sep 2010. [Online]. Available: <http://www.universetoday.com/73315/what-is-air-resistance/>.
- [31] "Half-a-loaf of Automotive Aerodynamics," 28 June 2010. [Online]. Available: <http://electricalpowerengineering.blogspot.ca/2010/06/half-loaf-of-automotive-aerodynamics-aa.html>.
- [32] *CarSim, Version 8.03a, September 2010*.
- [33] "The Engineering ToolBox," Rolling friction and rolling resistance, [Online]. Available: http://www.engineeringtoolbox.com/rolling-friction-resistance-d_1303.html.
- [34] "A Review of Available Vehicle Simulation Software," 19 May 1998. [Online]. Available: <http://arc.engin.umich.edu/events/archive/conf/conf98/mccarthy.pdf>.
- [35] "Carscoop: Electric powered MINI QED Concept," [Online]. Available: <http://carscoop.blogspot.com/2006/07/electric-powered-mini-qed-concept-with.html>.
- [36] "iMiEV," Mitsubishi Motors, [Online]. Available: <http://www.mitsubishi-motors.com/special/ev/>.
- [37] "Green Car Congress: Peugeot BB1 EV," [Online]. Available: <http://www.greencarcongress.com/2009/09/hybrid4-bb1-20090915.html>.
- [38] S. R. Cikanek and K. E. Bailey, "Regenerative Braking System For A Hybrid Electric Vehicle," in *Proceedings of American Control Conference*, Dearborn, 2002.
- [39] "Ceanet," [Online]. Available: <http://www.ceanet.com.au/Products/dSPACE/Hardware/MicroAutoBoxHardware.aspx>.
- [40] "dSPACE MicroAutoBox: Computing Larger Models Faster," [Online]. Available: <http://www.ceanet.com.au/Portals/0/dSPACE%20MicroAutoBox%20Oct%2009.pdf>.
- [41] S. Corrigan, "Texas Instruments: Introduction to the Controller Area Network (CAN)," 2008. [Online]. Available: <http://www.ti.com/lit/an/sloa101a/sloa101a.pdf>.
- [42] K. Pazul, "Microchip Technology Inc.: Controller Area Network (CAN) Basics," 1999. [Online]. Available: [http://www.ee.uidaho.edu/ee/classes/ECE341/refs/AN713%20-%20Controller%20Area%20Network%20\(CAN\)%20Basics.pdf](http://www.ee.uidaho.edu/ee/classes/ECE341/refs/AN713%20-%20Controller%20Area%20Network%20(CAN)%20Basics.pdf).

- [43] "Oxford Technology RT-2500 System," [Online]. Available:
<http://www.oxts.com/default.asp?pageRef=59>.
- [44] "RT Inertial and GPS Measurement Systems: User Manual," [Online]. Available:
<http://www.oxts.com/downloads/rtman.pdf>.
- [45] "Integrated Publishing: Tie-Rod Assemblies," [Online]. Available:
http://constructionmanuals.tpub.com/14273/css/14273_310.htm.
- [46] "Massload: Standard Wheel Load Scale," [Online]. Available: http://www.massload.com/product-Standard_Wheel_Load_Scale-1-1.html.
- [47] "Rebco 1-Weigh Scale System - 1500 LB 2-1/2 x 15 Pads," [Online]. Available:
<http://www.racerpartswholesale.com/product/1847/Scales>.
- [48] "Central Carolina Scale: Computerscales® AccuSet™ Karting 10" x 10"," [Online]. Available:
<http://racing.centralcarolinascalse.com/Longacre/computerscales-AccuSet-karting-72625.htm>.
- [49] "North Bay Electric Auto Association," [Online]. Available:
<http://www.nbeaa.org/osev/sota/blog.htm>.
- [50] "Safety - A Double-Lane Change (Obstacle Avoidance Test)," Apr 2006. [Online]. Available:
http://www.vss.psu.edu/BTRC/TestProcedures/3_safety.pdf.
- [51] "Adams/Insight help - MSC Adams 2011," MSC Software, 16 Jan. 2012. [Online]. Available:
<http://simcompanion.mssoftware.com/infocenter/index?page=content&id=DOC10099&cat=1VMO50&actp=LIST>.
- [52] V. Kaul, S. Singh, K. Rajagopalan and M. Coury, "Consumer Attitudes and Perceptions about Safety," in *SAE International*, 2010.
- [53] "Iranian Society of Automotive Engineers," 08 Aug 2008. [Online]. Available:
<http://isae.blogfa.com/post-48.aspx#axzz1wJAwZ3rg>.
- [54] L. Cheah and J. Heywood, "Meeting U.S. passenger vehicle fuel economy standards in 2016 and beyond," *Energy Policy*, vol. 39, no. 2011, pp. 454-466, 2010.

Appendix A

Tire Model Parameters

Table A-1: List of the parameters for nonlinear tire model

a_x	1.1182603735953
b_x	2.34839022760952
c_x	6.739312458777446
λ_x	0.7
β_x	0.17
γ_x	5
a_y	1.1256606428309
b_y	2.058190850185012
c_y	0.169820716112177733
λ_y	0.6
β_y	10
γ_y	0.15

Appendix B RT2000 Specifications

Parameter	RT2500 / RT2500-250	RT2502 / RT2502-250	RT2002 / RT2002-250	RT2004 / RT2004-250
GPS Type	L1	L1	L1/L2	GG-L1 ¹
Position Accuracy	3.0m CEP SPS 2.0m CEP SBAS	3.0m CEP SPS 2.0m CEP SBAS	1.5m CEP SPS 0.6m CEP SBAS 0.4m CEP DGPS 50cm CEP VBS 15cm CEP XP 10cm CEP HP 20cm 1σ L1 2cm 1σ L1/L2	1.8m CEP SPS 0.6m CEP SBAS 0.4m CEP DGPS 20cm 1σ L1 2cm 1σ GG-L1 ¹
Velocity Accuracy	0.2 km/h RMS	0.2 km/h RMS	0.1 km/h RMS	0.1 km/h RMS
Acceleration				
– Bias	10 mm/s ² 1σ	10 mm/s ² 1σ	10 mm/s ² 1σ	10 mm/s ² 1σ
– Linearity	0.01% 1σ	0.01% 1σ	0.01%	0.01%
– Scale Factor	0.1% 1σ	0.1% 1σ	0.1% 1σ	0.1% 1σ
– Range	100 m/s ²	100 m/s ²	100 m/s ²	100 m/s ²
Roll/Pitch	0.15° 1σ	0.15° 1σ	0.05° 1σ	0.05° 1σ
Heading	0.3° 1σ	0.2° 1σ	0.1° 1σ	0.1° 1σ
Angular Rate				
– Bias	0.02°/s 1σ	0.02°/s 1σ	0.01°/s 1σ	0.01°/s 1σ
– Scale Factor	0.2% 1σ	0.2% 1σ	0.2% 1σ	0.2% 1σ
– Range	100°/s	100°/s	100°/s	100°/s
Track (at 50km/h)	0.25° 1σ	0.25° 1σ	0.1° 1σ	0.1° 1σ
Slip Angle (at 50km/h)	0.4° 1σ	0.4° 1σ	0.2° 1σ	0.2° 1σ
Lateral Velocity	0.5% 1σ	0.4% 1σ	0.2% 1σ	0.2% 1σ
Update Rate	100 Hz / 250 Hz	100 Hz / 250 Hz	100 Hz / 250 Hz	100 Hz / 250 Hz
Power	9-18 V d.c. 15W	9-18 V d.c. 15W	9-18 V d.c. 15W	9-18 V d.c. 15W
Dimensions (mm)	234 x 120 x 76	234 x 120 x 76	234 x 120 x 76	234 x 120 x 76
Weight	2.3 kg	2.3 kg	2.4 kg	2.4 kg
Twin Antenna	No	Yes	No	No
GPS Raw Data	Yes	Yes	Yes	Yes

Note 1: GG-L1 means GPS and GLONASS L1. A GNSS base-station transmitting RTCA corrections for GPS and GLONASS L1 signals is required.

Figure A-1: Performance Specification for the RT2000 Systems [42]

Appendix C Vehicle Components

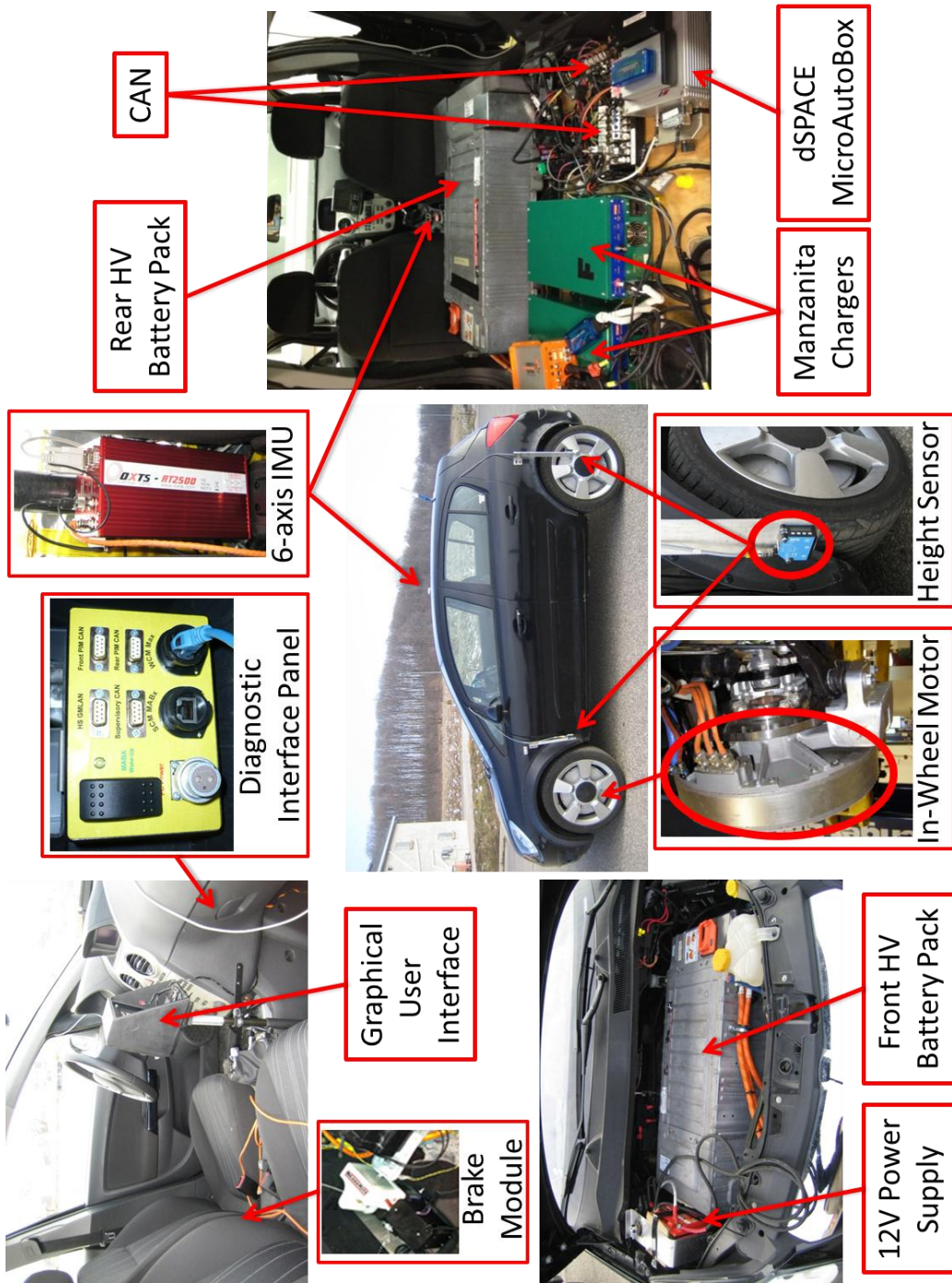


Figure A-2: Detailed picture of all vehicle components and sensors

Appendix D

Aerodynamic Drag Coefficient Tables

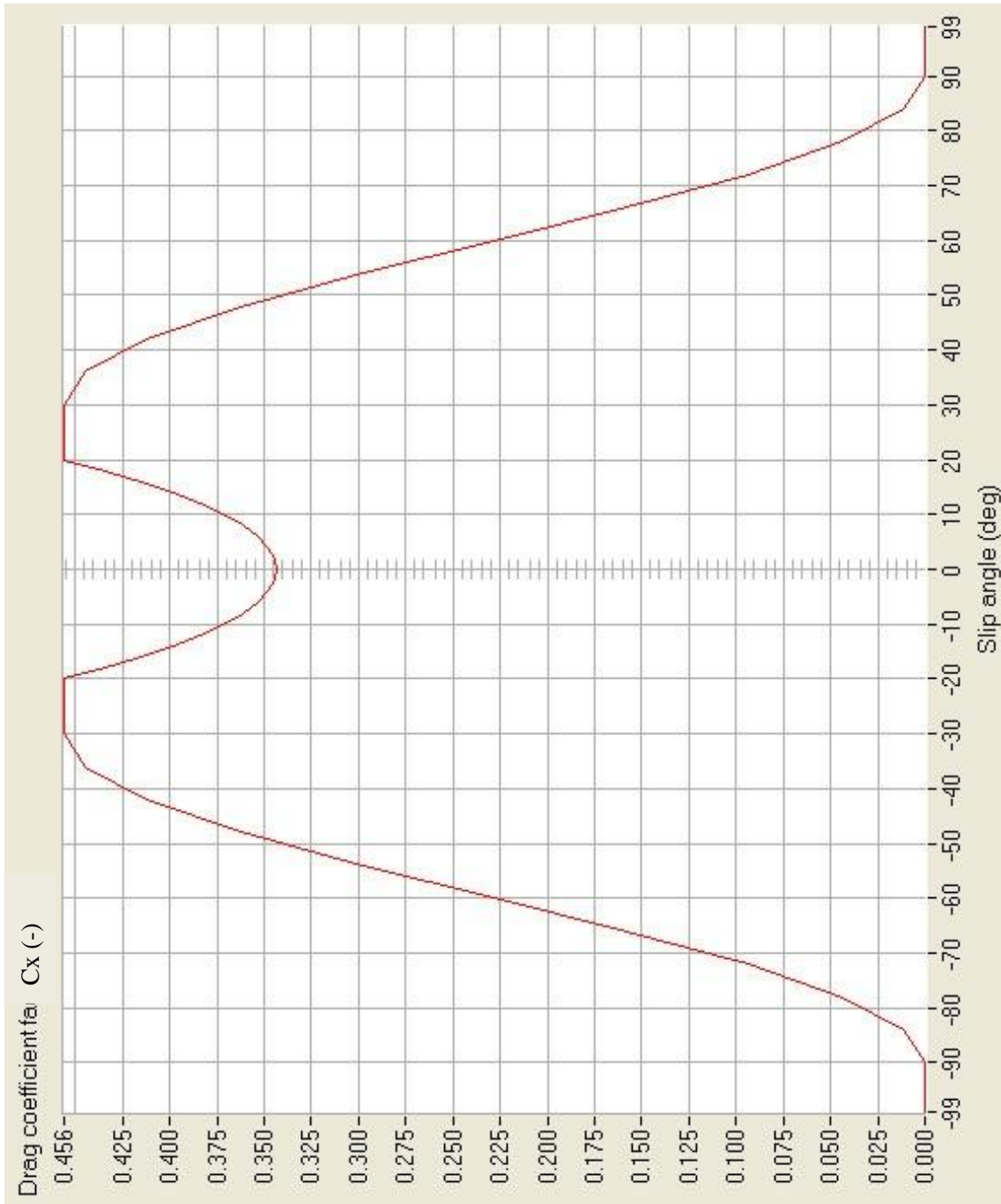


Figure A-3: Longitudinal drag coefficient vs. vehicle slip angle

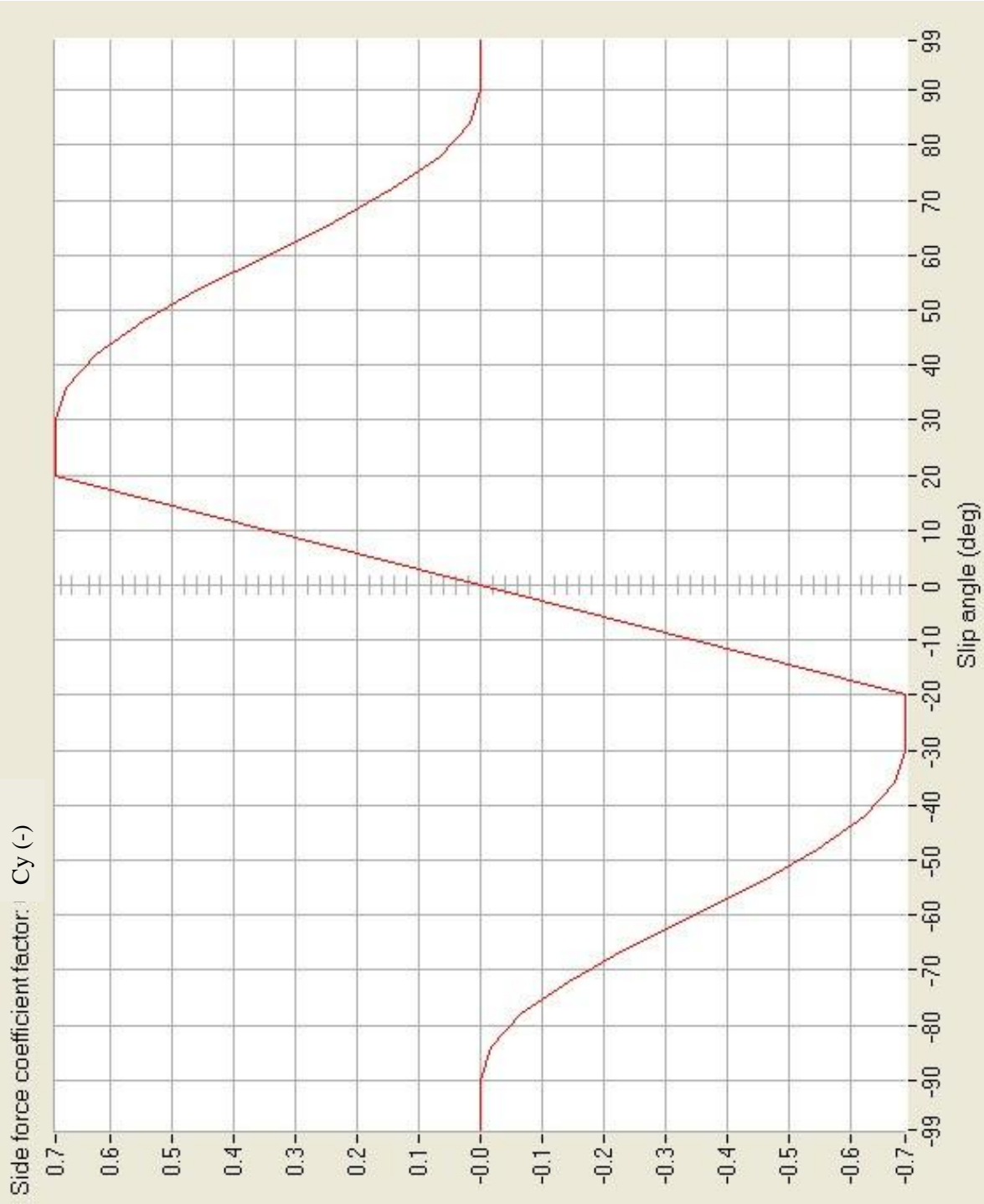


Figure A-4: Lateral drag coefficient vs. vehicle slip angle

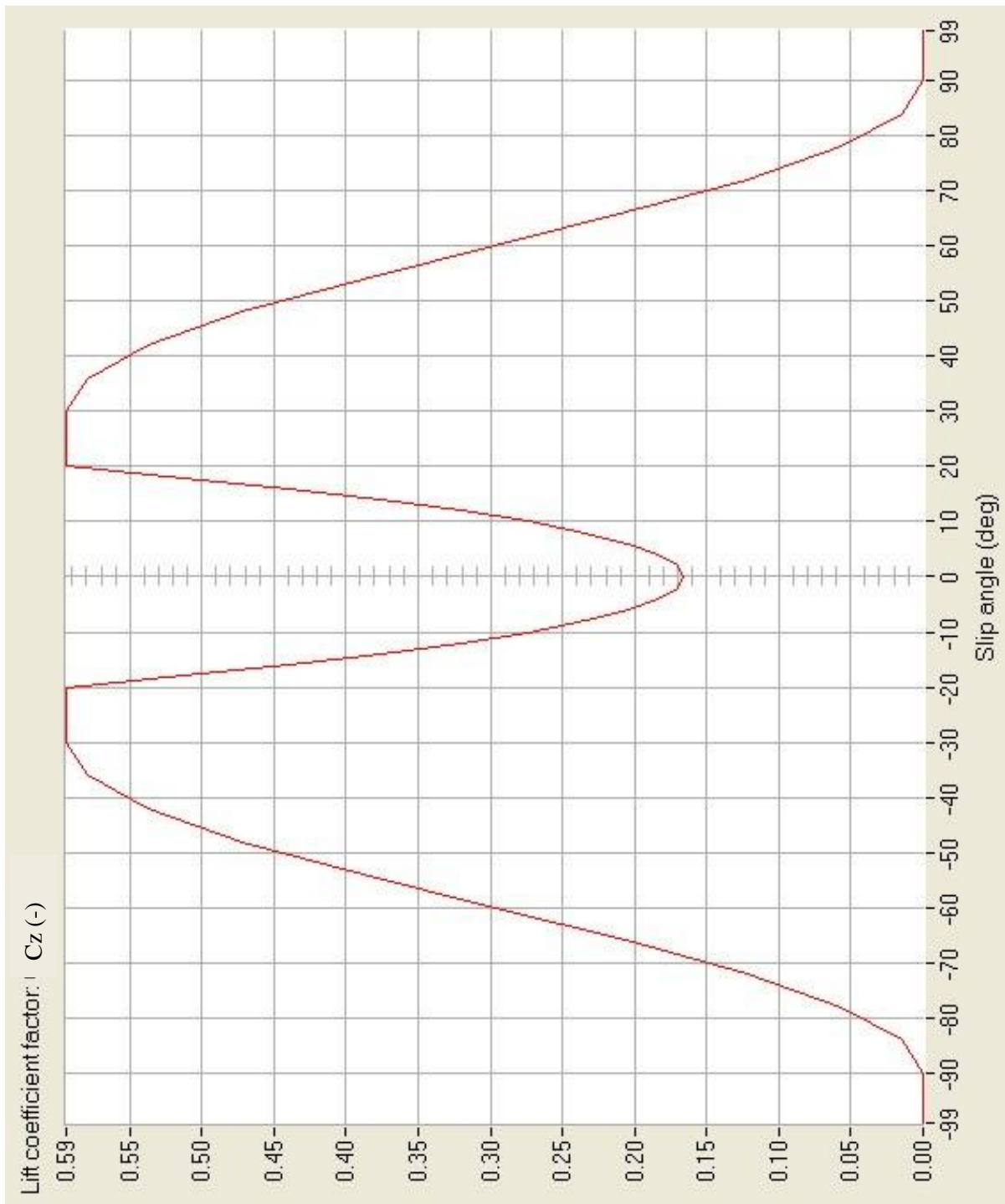


Figure A-5: Vertical drag coefficient vs. vehicle slip angle

Appendix E

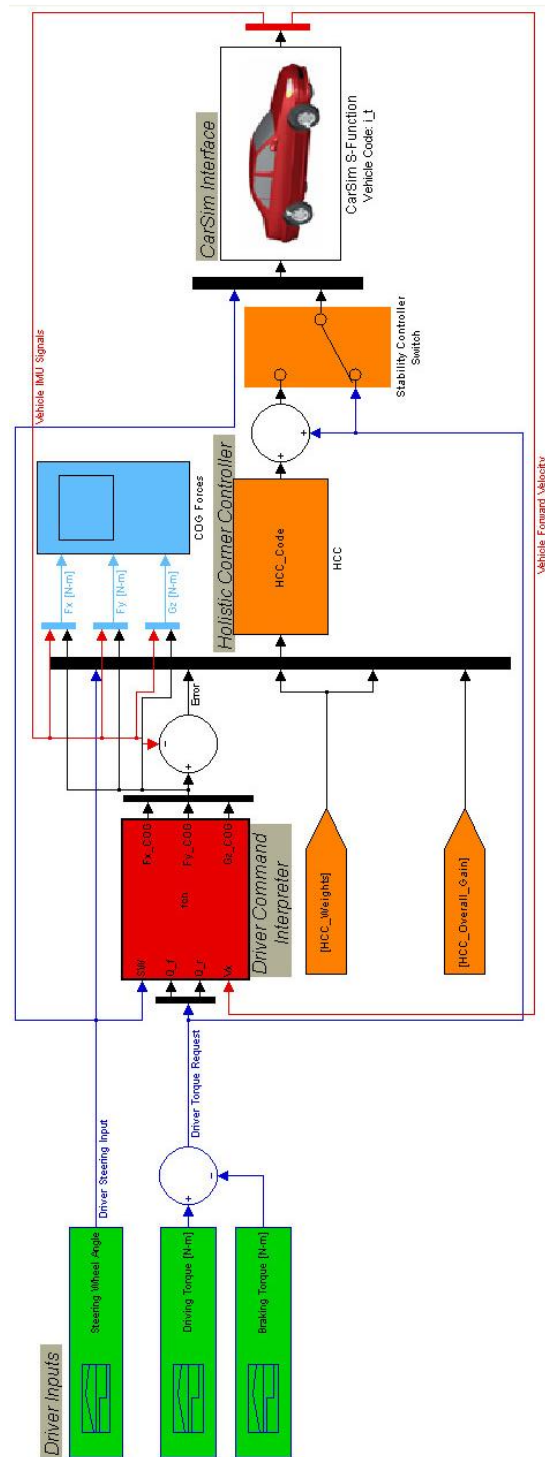


Figure A-6: CarSim/Simulink Simulation Interface

Appendix F

DCI Model Matlab Code

```
function [Fx_star,Fy_star,Gz_star] =
fcn(SW_in,SW_in_old,Q_in_f,Q_in_f_old,Q_in_r,Q_in_r_old,U_car)
%#eml

%%=====
%% NOTES:
%% 1. Please make sure "SW_in" is the angle of the wheel on the ground and
its unit is [Radians]
%% 2. Please make sure "U_car" is the longitudinal velocity of the vehicle
and its unit is [m/s]
%%=====
%% Initial Data

Lf = 1.096;           % Vehicle C.G. distance from the front wheel
Lr = 2.515-Lf;       % Vehicle C.G. distance from the rear wheel
HCG = 0.622158;
Reff = 0.332846;     % Effective wheel radius
H = HCG-(0.313/4);
d = 0.656;
d1 = d/2; d2 = d/2;

roll_steering_coefficient = 0.047206;

Iz = 2849;
Ix = 977.502;
Ixz = 27.9552;

g = 9.81;           % Gravity Acceleration
mass = 1535.2;      % Vehicle mass [1401 + 2*75]
Iw = 1.93368;       % Inertial moment of the wheel
M = mass/2;
Fz = mass*g;

mio = 1;           % Road Coefficient of Friction

persistent udot_dummy;
persistent vdot_dummy;
persistent rdot_dummy;
persistent wfdot_dummy;
persistent wrdot_dummy;
persistent zddot_dummy;
persistent phiddot_dummy;
persistent phidot_dummy;

if isempty(udot_dummy)
```

```

        udot_dummy = 0;
end
if isempty(vdot_dummy)
    vdot_dummy = 0;
end
if isempty(rdot_dummy)
    rdot_dummy = 0;
end
if isempty(wfdot_dummy)
    wfdot_dummy = 0;
end
if isempty(wrdot_dummy)
    wrdot_dummy = 0;
end
if isempty(zddot_dummy)
    zddot_dummy = 0;
end
if isempty(phiddot_dummy)
    phiddot_dummy = 0;
end
if isempty(phidot_dummy)
    phidot_dummy = 0;
end

persistent z;
if isempty(z)
    z = 0; % initial height of cg
end
persistent zdot;
if isempty(zdot)
    zdot = 0; % initial bounce motion
end

% Static Friction Coefficient

% Initial conditions of the dynamic model
u = U_car+0.1; % Initial longitudinal velocity
persistent v;
if isempty(v)
    v = 0; % Initial lateral velocity
end
persistent r;
if isempty(r)
    r = 0; % Initial r
end
persistent rdot;
if isempty(rdot)
    rdot = 0; % Initial yaw motion
end

```

```

persistent yaw;
if isempty(yaw)
    yaw = 0;
end
persistent wf;
if isempty(wf)
    wf = u/Reff;
end
persistent wr;
if isempty(wr)
    wr = u/Reff;
end
persistent phil;
if isempty(phil)
    phil = 0;
end

persistent phi;
if isempty(phi)
    phi = 0;
end
persistent phidot;
if isempty(phidot)
    phidot = 0;
end
persistent phiddot;
if isempty(phiddot)
    phiddot = 0;
end

Kphi = 79988;
Cphi = 697.44;

dt = 0.001;
dt_out = 0.005;

%%=====
SW_in_Rate = (SW_in-SW_in_old)/dt_out;
Q_in_f_Rate = (Q_in_f-Q_in_f_old)/dt_out;
Q_in_r_Rate = (Q_in_r-Q_in_r_old)/dt_out;

%%=====

%% DCI Embedded Block Inputs

drv_Tf_modified = Q_in_f;
drv_Tr_modified = Q_in_r;

Wheel_SA = SW_in;

```

```
%% Tire Forces Coefficients
```

```
ay = 1.25220; %%%%%%%%%%%%%%%%%%%%%%%%%%%%%%%%%%%%%%%%%%%%%%%%%%%%%%%%%%%%%%%%%%%%%%%%%%%  
by = 2.12080; %%% Tire Lat Spec %%%  
cy = 0.18189; %%%%%%%%%%%%%%%%%%%%%%%%%%%%%%%%%%%%%%%%%%%%%%%%%%%%%%%%%%%%%%%%%%%%%%%%%%%  
landay = 0.604242;  
betay = 10.12940;  
gamay = 0.171964;
```

```
ax = 1.08882; %%%%%%%%%%%%%%%%%%%%%%%%%%%%%%%%%%%%%%%%%%%%%%%%%%%%%%%%%%%%%%%%%%%%%%%%%%%  
bx = 2.62665; %%% Tire Long Spec %%%  
cx = 6.58032; %%%%%%%%%%%%%%%%%%%%%%%%%%%%%%%%%%%%%%%%%%%%%%%%%%%%%%%%%%%%%%%%%%%%%%%%%%%  
landax = 0.648628;  
betax = 0.162792;  
gamax = 4.660550;
```

```
% for i=1:4
```

```
%%%%%%%%%%%%%%%%%%%%%%%%%%%%%%%%%%%%%%%%%%%%%%%%%%%%%%%%%%%%%%%%%%%%%%%%%%  
%% LOOP 1 %%%%%%%%%%%%%%%%%%%%%%%%%%%%%%%%%%%%%%%%%%%%%%%%%%%%%%%%%%%%%%%%%%%%%%%%%%%  
%%%%%%%%%%%%%%%%%%%%%%%%%%%%%%%%%%%%%%%%%%%%%%%%%%%%%%%%%%%%%%%%%%%%%%%%%%
```

```
%% New Arranged Model
```

```
Vtf = sqrt((v+Lf*r)^2+u^2);  
Vtr = sqrt((v-Lr*r)^2+u^2);  
  
alpha_front = ((Wheel_SA-  
atan2((v+Lf*r),u))+roll_steering_coefficient*phi)*180/pi;%Slip angle of  
front tire  
alpha_rear = ((-atan2((v-Lr*r),u))-  
roll_steering_coefficient*phi)*180/pi; %Slip angle of rear tire  
  
vwxf = Vtf*cos(alpha_front*pi/180);  
vwxr = Vtr*cos(alpha_rear*pi/180);  
  
kappa_front = -(vwxf - Reff*wf) / max(vwxf, Reff*wf);  
%Slip ratio of front tire  
kappa_rear = -(vwxr - Reff*wr) / max(vwxr, Reff*wr);  
%Slip ratio of rear tire  
  
Fzf= (mass*g)/2;  
Fzr= (mass*g)/2;
```

```
%%=====
```

```
%% Front Tire Forces
```

```
FXf = ax*Fzf*mio*sin(bx*tanh(cx*kappa_front/mio));  
FYf = ay*Fzf*mio*sin(by*tanh(cy*alpha_front/mio));
```

```

    phi_x_front = (1-
landax*sech(gamax*kappa_front)*tanh((betax*alpha_front))^2);
    phi_y_front = (1-
landay*sech(gamay*alpha_front)*tanh((betay*kappa_front))^2);
    Fxf = FXf*phi_x_front;
% Front tire longitudinal force
    Fyf = FYf*phi_y_front;
% Front tire lateral force

%% Rear Tire Forces

    FXr = ax*Fzr*mio*sin(bx*tanh(cx*kappa_rear/mio));
    FYr = ay*Fzr*mio*sin(by*tanh(cy*alpha_rear/mio));
    phi_x_rear = (1-
landax*sech(gamax*kappa_rear)*tanh((betax*alpha_rear))^2);
    phi_y_rear = (1-
landay*sech(gamay*alpha_rear)*tanh((betay*kappa_rear))^2);
    Fxr = FXr*phi_x_rear;
% Rear tire longitudinal force
    Fyr = FYr*phi_y_rear;
% Rear tire lateral force

%%=====

%% Vehicle Dynamic Equations of Motion

    udot = (Fxf*cos(Wheel_SA)-Fyf*sin(Wheel_SA)+Fxr+mass*(r*v)-
0.3381*(U_car^2)-(0.03*Fz))/mass;    udot_dummy = udot;
    u=u+(udot_dummy+udot)/2*dt;

    vdot = (Fxf*sin(Wheel_SA)+Fyf*cos(Wheel_SA)+Fyr-mass*(r*u))/mass;
vdot_dummy = vdot;
    v=v+(vdot_dummy+vdot)/2*dt;

    rdot = ((Fxf*sin(Wheel_SA)+Fyf*cos(Wheel_SA))*Lf-Fyr*Lr)/Iz;
rdot_dummy = rdot;
    r=r+(rdot_dummy+rdot)/2*dt;

%%=====

%% Parameters Update

    wfdot = (drv_Tf_modified-Fxf*Reff)/Iw;
wfdot_dummy = wfdot;
    wf=wf+(wfdot_dummy+wfdot)/2*dt;

    wrdot = (drv_Tr_modified-Fxr*Reff)/Iw;
wrdot_dummy = wrdot;
    wr=wr+(wrdot_dummy+wrdot)/2*dt;

```

```

zddot=(1/mass)*(Fzf+Fzr-mass*g);
zddot_dummy = zddot;
zdot=zdot+(zddot_dummy+zddot)/2*dt;

phiddot=(-(M)*H*(vdot+r*u)+(M)*g*H*phi-Kphi*phi-
Cphi*phidot+Ixz*rdot)/Ix;          phiddot_dummy = phiddot;
phidot=phidot+(phiddot_dummy+phiddot)/2*dt;
phidot_dummy = phidot;
phi=phi+(phidot_dummy+phidot)/2*dt;

Wheel_SA = Wheel_SA + SW_in_Rate*dt;
drv_Tf_modified = drv_Tf_modified + Q_in_f_Rate*dt;
drv_Tr_modified = drv_Tr_modified + Q_in_r_Rate*dt;

%%%%%%%%%%%%%%%%%%%%%%%%%%%%%%%%%%%%%%%%%%%%%%%%%%%%%%%%%%%%%%%%%%%%%%%%
%% LOOP 2 %%%%%%%%%%%%%%%%%%%%%%%%%%%%%%%%%%%%%%%%%%%%%%%%%%%%%%%%%%%%%%%%%%%%%%%%%
%%%%%%%%%%%%%%%%%%%%%%%%%%%%%%%%%%%%%%%%%%%%%%%%%%%%%%%%%%%%%%%%%%%%%%%%

Vtf = sqrt((v+Lf*r)^2+u^2);
Vtr = sqrt((v-Lr*r)^2+u^2);

alpha_front = ((Wheel_SA-
atan2((v+Lf*r),u))+roll_steering_coefficient*phi)*180/pi;%Slip angle of
front tire
alpha_rear = ((-atan2((v-Lr*r),u)-
roll_steering_coefficient*phi)*180/pi;          %Slip angle of rear tire

vwxf = Vtf*cos(alpha_front*pi/180);
vwxr = Vtr*cos(alpha_rear*pi/180);

kappa_front = -(vwxf - Reff*wf) / max(vwxf, Reff*wf);
%Slip ratio of front tire
kappa_rear = -(vwxr - Reff*wr) / max(vwxr, Reff*wr);
%Slip ratio of rear tire

Fzf= (mass*g)/2;
Fzr= (mass*g)/2;

%%=====
%% Front Tire Forces

FXf = ax*Fzf*mio*sin(bx*tanh(cx*kappa_front/mio));
FYf = ay*Fzf*mio*sin(by*tanh(cy*alpha_front/mio));
phi_x_front = (1-
landax*sech(gamax*kappa_front)*tanh((betax*alpha_front)^2);
phi_y_front = (1-
landay*sech(gamay*alpha_front)*tanh((betay*kappa_front)^2);

```

```

    Fxf = FXf*phi_x_front;
% Front tire longitudinal force
    Fyf = FYf*phi_y_front;
% Front tire lateral force

%% Rear Tire Forces

    FXr = ax*Fzr*mio*sin(bx*tanh(cx*kappa_rear/mio));
    FYr = ay*Fzr*mio*sin(by*tanh(cy*alpha_rear/mio));
    phi_x_rear = (1-
landax*sech(gamax*kappa_rear)*tanh((betax*alpha_rear)^2);
    phi_y_rear = (1-
landay*sech(gamay*alpha_rear)*tanh((betay*kappa_rear)^2);
    Fxr = FXr*phi_x_rear;
% Rear tire longitudinal force
    Fyr = FYr*phi_y_rear;
% Rear tire lateral force

%%=====
%% Vehicle Dynamic Equations of Motion

    udot = (Fxf*cos(Wheel_SA)-Fyf*sin(Wheel_SA)+Fxr+mass*(r*v)-
0.3381*(U_car^2)-(0.03*Fz))/mass;    udot_dummy = udot;
    u=u+(udot_dummy+udot)/2*dt;

    vdot = (Fxf*sin(Wheel_SA)+Fyf*cos(Wheel_SA)+Fyr-mass*(r*u))/mass;
vdot_dummy = vdot;
    v=v+(vdot_dummy+vdot)/2*dt;

    rdot = ((Fxf*sin(Wheel_SA)+Fyf*cos(Wheel_SA))*Lf-Fyr*Lr)/Iz;
rdot_dummy = rdot;
    r=r+(rdot_dummy+rdot)/2*dt;

%%=====
%% Parameters Update

    wfdot = (drv_Tf_modified-Fxf*Reff)/Iw;
wfdot_dummy = wfdot;
    wf=wf+(wfdot_dummy+wfdot)/2*dt;

    wrdot = (drv_Tr_modified-Fxr*Reff)/Iw;
wrdot_dummy = wrdot;
    wr=wr+(wrdot_dummy+wrdot)/2*dt;

    zddot=(1/mass)*(Fzf+Fzr-mass*g);
zddot_dummy = zddot;
    zdot=zdot+(zddot_dummy+zddot)/2*dt;

```

```

    phiddot=(-(M)*H*(vdot+r*u)+(M)*g*H*phi-Kphi*phi-
Cphi*phidot+Ixz*rdot)/Ix;          phiddot_dummy = phiddot;
    phidot=phidot+(phiddot_dummy+phiddot)/2*dt;
phidot_dummy = phidot;
    phi=phi+(phidot_dummy+phidot)/2*dt;

Wheel_SA = Wheel_SA + SW_in_Rate*dt;
drv_Tf_modified = drv_Tf_modified + Q_in_f_Rate*dt;
drv_Tr_modified = drv_Tr_modified + Q_in_r_Rate*dt;

%%%%%%%%%%%%%%%%%%%%%%%%%%%%%%%%%%%%%%%%%%%%%%%%%%%%%%%%%%%%%%%%%%%%%%%%
%% LOOP 3 %%%%%%%%%%%%%%%%%%%%%%%%%%%%%%%%%%%%%%%%%%%%%%%%%%%%%%%%%%%%%%%%%%%%%%%%%
%%%%%%%%%%%%%%%%%%%%%%%%%%%%%%%%%%%%%%%%%%%%%%%%%%%%%%%%%%%%%%%%%%%%%%%%

    Vtf = sqrt((v+Lf*r)^2+u^2);
    Vtr = sqrt((v-Lr*r)^2+u^2);

    alpha_front = ((Wheel_SA-
atan2((v+Lf*r),u))+roll_steering_coefficient*phi)*180/pi;%Slip angle of
front tire
    alpha_rear = ((-atan2((v-Lr*r),u))-
roll_steering_coefficient*phi)*180/pi;          %Slip angle of rear tire

    vwx_f = Vtf*cos(alpha_front*pi/180);
    vwx_r = Vtr*cos(alpha_rear*pi/180);

    kappa_front = -(vwx_f - Reff*wf) / max(vwx_f, Reff*wf);
%Slip ratio of front tire
    kappa_rear = -(vwx_r - Reff*wr) / max(vwx_r, Reff*wr);
%Slip ratio of rear tire

    Fzf= (mass*g)/2;
    Fzr= (mass*g)/2;

%%=====
%% Front Tire Forces

    FXf = ax*Fzf*mio*sin(bx*tanh(cx*kappa_front/mio));
    FYf = ay*Fzf*mio*sin(by*tanh(cy*alpha_front/mio));
    phi_x_front = (1-
landax*sech(gamax*kappa_front)*tanh((betax*alpha_front))^2);
    phi_y_front = (1-
landay*sech(gamay*alpha_front)*tanh((betay*kappa_front))^2);
    Fxf = FXf*phi_x_front;
% Front tire longitudinal force
    Fyf = FYf*phi_y_front;
% Front tire lateral force

%% Rear Tire Forces

```

```

    FXr = ax*Fzr*mio*sin(bx*tanh(cx*kappa_rear/mio));
    FYr = ay*Fzr*mio*sin(by*tanh(cy*alpha_rear/mio));
    phi_x_rear = (1-
landax*sech(gamax*kappa_rear)*tanh((betax*alpha_rear))^2);
    phi_y_rear = (1-
landay*sech(gamay*alpha_rear)*tanh((betay*kappa_rear))^2);
    Fxr = FXr*phi_x_rear;
% Rear tire longitudinal force
    Fyr = FYr*phi_y_rear;
% Rear tire lateral force

%%=====

%% Vehicle Dynamic Equations of Motion

    udot = (Fxf*cos(Wheel_SA)-Fyf*sin(Wheel_SA)+Fxr+mass*(r*v)-
0.3381*(U_car^2)-(0.03*Fz))/mass;    udot_dummy = udot;
    u=u+(udot_dummy+udot)/2*dt;

    vdot = (Fxf*sin(Wheel_SA)+Fyf*cos(Wheel_SA)+Fyr-mass*(r*u))/mass;
vdot_dummy = vdot;
    v=v+(vdot_dummy+vdot)/2*dt;

    rdot = ((Fxf*sin(Wheel_SA)+Fyf*cos(Wheel_SA))*Lf-Fyr*Lr)/Iz;
rdot_dummy = rdot;
    r=r+(rdot_dummy+rdot)/2*dt;

%%=====

%% Parameters Update

    wfdot = (drv_Tf_modified-Fxf*Reff)/Iw;
wfdot_dummy = wfdot;
    wf=wf+(wfdot_dummy+wfdot)/2*dt;

    wrdot = (drv_Tr_modified-Fxr*Reff)/Iw;
wrdot_dummy = wrdot;
    wr=wr+(wrdot_dummy+wrdot)/2*dt;

    zddot=(1/mass)*(Fzf+Fzr-mass*g);
zddot_dummy = zddot;
    zdot=zdot+(zddot_dummy+zddot)/2*dt;

    phiddot=(-(M)*H*(vdot+r*u)+(M)*g*H*phi-Kphi*phi-
Cphi*phidot+Ixz*rdot)/Ix;    phiddot_dummy = phiddot;
    phidot=phidot+(phiddot_dummy+phiddot)/2*dt;
phidot_dummy = phidot;
    phi=phi+(phidot_dummy+phidot)/2*dt;

```

```

Wheel_SA = Wheel_SA + SW_in_Rate*dt;
drv_Tf_modified = drv_Tf_modified + Q_in_f_Rate*dt;
drv_Tr_modified = drv_Tr_modified + Q_in_r_Rate*dt;

%%%%%%%%%%%%%%%%%%%%%%%%%%%%%%%%%%%%%%%%%%%%%%%%%%%%%%%%%%%%%%%%%%%%%%%%
%% LOOP 4 %%%%%%%%%%%%%%%%%%%%%%%%%%%%%%%%%%%%%%%%%%%%%%%%%%%%%%%%%%%%%%%%%%%%%%%%%
%%%%%%%%%%%%%%%%%%%%%%%%%%%%%%%%%%%%%%%%%%%%%%%%%%%%%%%%%%%%%%%%%%%%%%%%

Vtf = sqrt((v+Lf*r)^2+u^2);
Vtr = sqrt((v-Lr*r)^2+u^2);

alpha_front = ((Wheel_SA-
atan2((v+Lf*r),u))+roll_steering_coefficient*phi)*180/pi;%Slip angle of
front tire
alpha_rear = ((-atan2((v-Lr*r),u))-
roll_steering_coefficient*phi)*180/pi; %Slip angle of rear tire

vwxf = Vtf*cos(alpha_front*pi/180);
vwxr = Vtr*cos(alpha_rear*pi/180);

kappa_front = -(vwxf - Reff*wf) / max(vwxf, Reff*wf);
%Slip ratio of front tire
kappa_rear = -(vwxr - Reff*wr) / max(vwxr, Reff*wr);
%Slip ratio of rear tire

Fzf= (mass*g)/2;
Fzr= (mass*g)/2;

%%=====

%% Front Tire Forces

FXf = ax*Fzf*mio*sin(bx*tanh(cx*kappa_front/mio));
FYf = ay*Fzf*mio*sin(by*tanh(cy*alpha_front/mio));
phi_x_front = (1-
landax*sech(gamax*kappa_front)*tanh((betax*alpha_front))^2);
phi_y_front = (1-
landay*sech(gamay*alpha_front)*tanh((betay*kappa_front))^2);
Fxf = FXf*phi_x_front;
% Front tire longitudinal force
Fyf = FYf*phi_y_front;
% Front tire lateral force

%% Rear Tire Forces

FXr = ax*Fzr*mio*sin(bx*tanh(cx*kappa_rear/mio));
FYr = ay*Fzr*mio*sin(by*tanh(cy*alpha_rear/mio));

```

```

    phi_x_rear = (1-
landax*sech(gamax*kappa_rear)*tanh((betax*alpha_rear))^2);
    phi_y_rear = (1-
landay*sech(gamay*alpha_rear)*tanh((betay*kappa_rear))^2);
    Fxr = FXr*phi_x_rear;
% Rear tire longitudinal force
    Fyr = FYr*phi_y_rear;
% Rear tire lateral force

%%=====

%% Vehicle Dynamic Equations of Motion

    udot = (Fxf*cos(Wheel_SA)-Fyf*sin(Wheel_SA)+Fxr+mass*(r*v)-
0.3381*(U_car^2)-(0.03*Fz))/mass;    udot_dummy = udot;
    u=u+(udot_dummy+udot)/2*dt;

    vdot = (Fxf*sin(Wheel_SA)+Fyf*cos(Wheel_SA)+Fyr-mass*(r*u))/mass;
vdot_dummy = vdot;
    v=v+(vdot_dummy+vdot)/2*dt;

    rdot = ((Fxf*sin(Wheel_SA)+Fyf*cos(Wheel_SA))*Lf-Fyr*Lr)/Iz;
rdot_dummy = rdot;
    r=r+(rdot_dummy+rdot)/2*dt;

%%=====

%% Parameters Update

    wfdot = (drv_Tf_modified-Fxf*Reff)/Iw;
wfdot_dummy = wfdot;
    wf=wf+(wfdot_dummy+wfdot)/2*dt;

    wrdot = (drv_Tr_modified-Fxr*Reff)/Iw;
wrdot_dummy = wrdot;
    wr=wr+(wrdot_dummy+wrdot)/2*dt;

    zddot=(1/mass)*(Fzf+Fzr-mass*g);
zddot_dummy = zddot;
    zdot=zdot+(zddot_dummy+zddot)/2*dt;

    phiddot=(-(M)*H*(vdot+r*u)+(M)*g*H*phi-Kphi*phi-
Cphi*phidot+Ixz*rdot)/Ix;    phiddot_dummy = phiddot;
    phidot=phidot+(phiddot_dummy+phiddot)/2*dt;
phidot_dummy = phidot;
    phi=phi+(phidot_dummy+phidot)/2*dt;

```

```

Wheel_SA = Wheel_SA + SW_in_Rate*dt;
drv_Tf_modified = drv_Tf_modified + Q_in_f_Rate*dt;
drv_Tr_modified = drv_Tr_modified + Q_in_r_Rate*dt;

%%%%%%%%%%%%%%%%%%%%%%%%%%%%%%%%%%%%%%%%%%%%%%%%%%%%%%%%%%%%%%%%%%%%%%%%
%% LOOP END %%%%%%%%%%%%%%%%%%%%%%%%%%%%%%%%%%%%%%%%%%%%%%%%%%%%%%%%%%%%%%%%%%%%%%%%%
%%%%%%%%%%%%%%%%%%%%%%%%%%%%%%%%%%%%%%%%%%%%%%%%%%%%%%%%%%%%%%%%%%%%%%%%

%%=====

Fx_s = Fxf*cos(Wheel_SA)-Fyf*sin(Wheel_SA)+Fxr-0.3381*(U_car^2)-
(0.03*mass*g);
Fy_s = Fxf*sin(Wheel_SA)+Fyf*cos(Wheel_SA)+Fyr;
Gz_s = rdot*Iz;

%% Final Output Phase

Fx_star = Fx_s;
Fy_star = Fy_s;
Gz_star = Gz_s;

```

Appendix G

Sensitivity Analysis Results

